Coupled Transport Processes in Zero-Gravity Distillation Columns

Dissertation

Niklas Albrecht Preußer

TECHNISCHE
UNIVERSITÄT
DARMSTADT

Coupled Transport Processes in Zero-Gravity Distillation Columns

Doctoral thesis
by Niklas Albrecht Preußer

submitted in fulfillment of the requirements for the
degree of Doktor-Ingenieur
(Dr.-Ing.)

at the Department of Mechanical Engineering
of the Technische Universität Darmstadt

First Examiner: Apl. Prof. Dr. Tatiana Gambaryan-Roisman
Second Examiner: Prof. Dr.-Ing. Peter Stephan
Third Examiner: Prof. Dr. rer. nat. Steffen Hardt

Darmstadt 2020

Niklas Albrecht Preußer: Coupled Transport Processes in Zero-Gravity Distillation Columns
Darmstadt, Technische Universität Darmstadt
Thesis published online on TUprints in 2020
Oral examination on January 28, 2020

Danksagung

Diese Arbeit entstand im Rahmen meiner Tätigkeit am Fachgebiet für Technische Thermodynamik (TTD) der TU Darmstadt. Meiner Referentin Apl. Prof. Dr. Tatiana Gambaryan-Roisman und meinem Referenten Prof. Dr. Peter Stephan möchte ich für die hervorragende wissenschaftliche Betreuung meiner Arbeit danken. Beide schafften einen Rahmen, in dem ich selbstständig meine Ideen entwickeln und vorantreiben konnte. Gleichzeitig wurde mir Unterstützung zuteil, wenn ich diese benötigte. Prof. Dr. Steffen Hardt danke ich für die Übernahme des Koreferats.

Dem ganzen Kollegium am Fachgebiet TTD möchte ich für das angenehme Miteinander im Büro und außerhalb des Büros danken. Durch die Hilfe von Gaby Gunkel und Heike Kagerbauer ließ sich der Arbeitsalltag deutlich leichter gestalten. Die IT sorgte stets für die optimale Infrastruktur in Büro und Labor. Der Werkstatt unter der Leitung von Roland Berntheisel und unserem Techniker Robert Schrod danke ich für die Unterstützung bei Entwurf, Fertigung und Aufbau meines Experiments. Besonders erwähnen möchte ich auch Dr. Felix Größmann, der mir in meiner Anfangszeit sehr oft mit gutem Rat zur Seite stand, auch wenn seine zeitlichen Kapazitäten eigentlich beschränkt waren. Weiterhin hatten alle Studierenden, deren Abschlussarbeiten ich betreuen durfte und die mich mit hilfswissenschaftlichen Tätigkeiten unterstützt haben, einen beträchtlichen Anteil am Gelingen meiner Arbeit.

Für die sorgfältige Durchsicht meines Manuskripts bin ich Achim Bender und Dr. Timm Winterling zu Dank verpflichtet. Außerdem danke ich Irini Losoff für die sprachliche Korrektur meiner Arbeit.

Ein besonderer Dank gilt meiner Familie für die stetige Unterstützung auf meinem Bildungsweg und bei allem darüber hinaus.

Abstract

Distillation is an essential process in the chemical industry. To cope with small production quantities of specialized chemicals, modular production plants have gained increasing attention in the past years. Zero-gravity distillation is a small-scale distillation process, which offers high separation efficiencies and can be used as a part of modular production plants. Instead of gravity, capillary forces are utilized to sustain the fluid circulation. In order to apply the process in industry, the influence of the operating parameters and the capillary structure on the process variables has to be understood. In this thesis, the results of experiments and simulations of zero-gravity distillation are presented and discussed.

The experimental setup, which is similar to a flat heat pipe, allows measuring the wall and vapor temperatures, the fluid composition at the condenser, the pressure, and the liquid-vapor interface shape. Two different capillary structures were investigated at infinite reflux with mixtures of water and ethanol. For the extensively studied triangular groove structure, the overall average ethanol fraction, the heat flux, and the inclination of the system were varied. Negative inclination angles indicate that the condenser lay higher than the evaporator. The separation efficiency defined as the difference between the ethanol mole fraction at the condenser and the system average ethanol mole fraction increased with decreasing overall average ethanol fraction, decreasing heat flux, and decreasing inclination angle. For the advanced rectangular groove structure, three fluid compositions were tested. By comparing the two groove structures, no clear conclusion could be drawn on which capillary structure promotes separation.

Kurzfassung

Destillationen sind essenziell in der chemischen Industrie. Um die Produktion kleiner Mengen von Spezialchemikalien leisten zu können, sind modulare Produktionsanlagen in den Fokus gerückt. Die Gravidestillation ist ein kleinskaliger Destillationsprozess, der mit hohen Trennraten modular eingesetzt werden kann. Anstatt der Gravitation werden Kapillarkräfte genutzt, um die Fluidströmung aufrechtzuerhalten. Um den Prozess industriell nutzen zu können, muss der Einfluss der Betriebsparameter und der Kapillarstruktur auf die Prozessvariablen verstanden werden. In dieser Arbeit werden Ergebnisse von Experimenten und Simulationen zur Gravidestillation vorgestellt und diskutiert.

Mit dem Versuchsaufbau, der mit einer *Flat Heat Pipe* vergleichbar ist, können die Wand- und Dampftemperaturen, die Zusammensetzung am Kondensator, der Druck und die Form der Phasengrenzfläche gemessen werden. Zwei Kapillarstrukturen wurden mit Wasser-Ethanol-Gemischen bei unendlichem Rückfluss untersucht. Für die detailliert untersuchte dreieckige Rillenstruktur wurden der mittlere Ethanolanteil, die Wärmestromdichte und die Neigung des Systems variiert. Hierbei stehen negative Winkel dafür, dass der Kondensator höher liegt als der Verdampfer. Die Trenneffizienz, definiert als die Differenz zwischen dem Ethanolanteil am Kondensator und dem mittleren Ethanolanteil, nahm mit abnehmendem mittleren Ethanolanteil, mit abnehmender Wärmestromdichte und abnehmendem Neigungswinkel zu. Für die fortgeschrittene rechteckige Rillenstruktur wurden drei Fluidzusammensetzungen untersucht. Durch den Vergleich der zwei Rillenstrukturen konnte nicht eindeutig identifiziert werden, welche Struktur eine Trennung begünstigt.

In the theoretical model, heat transfer, mass transfer, and hydrodynamics are coupled for zero-gravity distillation in channel-shaped capillary structures. In contrast to existing models for porous media as capillary structures, the influence of the variation of the area occupied by the liquid along the flow direction is accounted for. Additionally, heat conduction in the channel wall is included.

The theoretical model of zero-gravity distillation was applied to a re-entrant channel structure at different values of the heat flux, the inclination, and the radius of the circular part of the cross section. As in the experiments, the separation improved with decreasing heat flux, which means the difference between the ethanol mole fractions between evaporator and condenser increased. Changing the inclination of the system did not lead to changes in the distribution of the component mole fractions in the system. With decreasing the radius of the circular part of the capillary structure cross section, an improved separation was observed. Thus, an influence of the capillary structure design on the separation was shown.

In dem theoretischen Modell werden Wärmetransport, Stofftransport und Hydrodynamik für kanalförmige Kapillarstrukturen gekoppelt. Im Gegensatz zu existierenden Modellen für poröse Medien wird der Einfluss der Veränderung des von der Flüssigkeit eingenommenen Querschnitts entlang der Strömungsrichtung berücksichtigt. Zusätzlich wird die Wärmeleitung in der Kanalwand betrachtet.

Mit dem theoretischen Modell der Gravidestillation wurde eine *Re-Entrant*-Kanalstruktur für variierte Wärmestromdichten, Neigungen und Radien des kreisförmigen Teils des Kanalquerschnitts untersucht. Wie im Experiment verbesserte sich die Trennung für eine abnehmende Wärmestromdichte, was bedeutet, dass die Differenz zwischen den Ethanolstoffmengenanteilen im Verdampfer und denen im Kondensator zunahm. Für variierte Neigungswinkel konnte keine Veränderung in der Trennung beobachtet werden. Eine Abnahme des Radiusses des kreisförmigen Teils des Kanalquerschnitts führte zu einer verbesserten Trennung. Dadurch konnte ein Einfluss der Kapillarstruktur belegt werden.

Contents

Nomenclature

Latin Symbols

Symbol	Description	Unit
a	thermal diffusivity	$\mathrm{m^2\,s^{-1}}$
A	area	$\mathrm{m^2}$
c	concentration	$\mathrm{mol\,m^{-3}}$
C	curvature	$\mathrm{m^{-1}}$
d	diameter	m
D	diffusion coefficient	$\mathrm{m^2\,s}$
f	body force	$\mathrm{N\,m^{-3}}$
f_F	Fanning friction factor	-
g	gravitational acceleration	$\mathrm{m\,s^{-2}}$
Δh_LV	enthalpy of evaporation	$\mathrm{J\,kg^{-1}}$
$\Delta \widetilde{h}_\mathrm{LV}$	molar enthalpy of evaporation	$\mathrm{J\,mol^{-1}}$
h	height	m
$HETP$	height equivalent to a theoretical plate	mm
k	mass transfer coefficient	$\mathrm{m\,s^{-1}}$
K	overall mass transfer coefficient	$\mathrm{mol\,m^{-2}\,s^{-1}}$
L	characteristic length	m
$\dot{M}$	mass flow rate	$\mathrm{kg\,s^{-1}}$
$\widetilde{M}$	molar mass	$\mathrm{kg\,mol^{-1}}$
N	number of theoretical plates	-
$\dot{N}$	molar flow rate	$\mathrm{mol\,s^{-1}}$
$\vec{n}$	normal vector	m
p	pressure	$\mathrm{N\,m^{-2}}$
P	permeability	$\mathrm{m^2}$
$\dot{q}$	integrated heat flux	$\mathrm{W\,m^{-1}}$
$\dot{q}$	heat flux	$\mathrm{W\,m^{-2}}$
$\dot{Q}$	heat flow	W
r	radial coordinate	m
R	radius	m
R_R	reflux ratio	-
S	specific interface area	$\mathrm{m^{-1}}$
s_c	source term	$\mathrm{mol\,m^{-3}\,s^{-1}}$
t	temperature	$\mathrm{°C}$
T	temperature	K

Symbol	Description	Unit
u	velocity in x-direction	$\mathrm{m\,s^{-1}}$
v	velocity in y-direction	$\mathrm{m\,s^{-1}}$
w	velocity in z-direction	$\mathrm{m\,s^{-1}}$
W	width	m
x	cartesian coordinate	m
$\widetilde{x}$	liquid mole fraction	-
y	cartesian coordinate	m
$\widetilde{y}$	vapor mole fraction	-
z	cartesian coordinate	m

Greek Symbols

Symbol	Description	Unit
α	opening angle	$^\circ$
β	inclination angle	$^\circ$
Γ	interfacial coordinate	m
λ	thermal conductivity	$\mathrm{W\,m^{-1}\,K^{-1}}$
μ	dynamic viscosity	$\mathrm{kg\,m^{-1}\,s^{-1}}$
ρ	density	$\mathrm{kg\,m^{-3}}$
σ	surface tension	$\mathrm{N\,m^{-1}}$
φ	conductive transport coefficient	-
ψ	diffusive transport coefficient	-

Subscripts

Subscript	Description
A	component A
B	component B
BF	boundary flux
C	capillary
co	condenser
crit	critical
D	distilled/distillate
E	ethanol
ev	evaporator
G	groove
H	hydraulic
i	variable component
I	inner
int	interface
L	liquid
mac	macroscopic
melt	melting
mic	micro region
O	outer
OA	overall average
PC	phase change
RE	re-entrant
S	solid
sat	saturation
tot	total
V	vapor

Accents

Accent	Description
$\bar{}$	averaged

Abbreviations

Abbreviation	Description
CHR	chromatic confocal distance measurement system
NMR	nuclear magnetic resonance
PEEK	polyether ether ketone

Dimensionless Numbers

Symbol	Description	Exemplary definition
Pe	Péclet number (heat transfer)	$\frac{L\,w}{a}$
Pe'	Péclet number (mass transfer)	$\frac{L\,w}{D}$
Po	Poiseuille number	$f_{\mathrm{F}}\,Re$
Pr	Prandtl number	$\frac{\mu}{\rho\,a}$
Re	Reynolds number	$\frac{L\,w\rho}{\mu}$
Sc	Schmidt number	$\frac{\mu}{\rho\,D}$

Chapter 1

Introduction

In the chemical industry, the differentiation of products increases while at the same time the product life cycles get shorter [11]. Chemical companies face the challenge of producing lower quantities than today of each differentiated product for possibly shorter time spans [23]. As a consequence, the modular setup of chemical production processes has gained increasing attention in the past years. The connection of different production modules with variable output quantities allows a more flexible setup of production processes and also decentralized manufacturing close to the customer [36].

The separation of mixtures by distillation is an essential process in the chemical industry and a part of the production of many chemical products. On large scales, rectification processes are well established. These work continuously with counter current flows of the liquid and vapor phase and produce large quantities of chemicals. Small scale distillation apparatuses, on the other hand, often work discontinuously and produce smaller quantities. In many cases, liquid and vapor phase flow concurrently, which makes the processes less efficient. To enable efficient distillation in modular production plants, small scale distillation devices are a focus of research in process engineering. When the characteristic length scales of the transport processes are in the order of magnitude of several microns to less than a millimeter, these can be classified as micro distillation processes [33].

Zero-gravity distillation is a concept used for micro distillation, which has shown high separation efficiencies in the past. In the pioneering article in 1985, Seok and Hwang [68] stated that zero-gravity distillation "may offer the same degree of separation in a horizontal column one-ninth the length of conventional vertical towers". Kenig *et al.* [33] stated that eight zero-gravity distillation columns would be needed to obtain the same flow rates as in conventional columns. With its high separation efficiencies, the process could be beneficial for modularizing processes in the chemical industry. To the author's knowledge, the process has not been industrially applied thus far despite the promising results obtained more than thirty years ago. This is mainly due to the non-existent design guidelines [33]. These can only be formulated if the coupled hydrodynamics, heat transfer, and mass transfer processes in these devices are adequately understood. Until now this is not the case. For this reason, zero-gravity distillation is investigated in a detailed manner in this work with experimental and modeling methods.

This thesis is structured as follows: in Chapter 2 the relevant fundamentals of distillation in general and zero-gravity distillation in particular are introduced. An overview of different micro distillation concepts

is given to put zero-gravity distillation into perspective. Relevant research in the field of zero-gravity distillation is summarized. From the state of the art, the concrete aims of this work are derived in Chapter 3. In Chapter 4 the experimental setup designed to investigate zero-gravity distillation, the measurement techniques used, and the data evaluation methods are described. The description of the experimental methods is followed by the presentation and discussion of the experimental results in Chapter 5. Subsequently, the development of a theoretical model describing the relevant transport processes in zero-gravity distillation columns is described. The concept of the model and the governing equations are presented and explained in Chapter 6. The results obtained with the theoretical model are presented in Chapter 7. The thesis is concluded with a summary and an outlook in Chapter 8.

Chapter 2

State of the Art

In this chapter, relevant fundamentals are introduced and a literature overview of related work is given. The chapter begins with fundamentals of distillation. These are followed by a review of micro distillation concepts and past research on zero-gravity distillation. Additionally, research on two-component heat pipes is put in context with zero-gravity distillation.

2.1 Distillation

2.1.1 Fundamentals

Distillation is the thermal separation of mixtures by utilizing different boiling points of the mixture components. The fundamentals given in this paragraph can also be found in [51]. Distillation processes can be characterized in closed, open, and counter current systems. Additionally, continuous and discontinuous systems can be distinguished. In closed and open distillation processes, vapor and liquid flow in the same direction, which means that these are concurrent distillation processes. Closed systems are distillation processes in which the vapor is withdrawn from the system at a fixed position and is in equilibrium with the withdrawn liquid. In open processes, vapor is withdrawn from the distillation chamber at different positions in the direction of flow. Thus, the vapor composition varies depending on the position at which it is withdrawn. The overall vapor withdrawn from the system is not in equilibrium with the liquid withdrawn only at one position in the chamber. In counter current distillation processes the vapor and the liquid flow in opposite directions. In continuous systems, feed and distillate flows are continuously withdrawn from the system. This means that the compositions of the different streams do not change with time. In contrast, the compositions of liquid and vapor streams vary with time in discontinuous systems. A special case of counter current distillation is rectification, which is a repeated counter current distillation on multiple plates or stages. Rectification is usually performed in vertical columns. The molar flow supplied to the system is referred to as feed. At the top of the column, the top product is withdrawn, which mainly consists of the more volatile component in the system. At the bottom of the column, the bottom product is withdrawn, which mainly consists of the less volatile component. In rectification, the condensed vapor at the top of the column is partly recirculated in the system. When a higher purity of top

and bottom product streams is desired, this reflux is usually increased. Therefore, an important property of rectification processes is the reflux ratio. It is defined as

$$R_{\mathrm{R}} = \frac{\dot{N}_{\mathrm{L}}}{\dot{N}_{\mathrm{D}}} \tag{2.1}$$

with the recirculated liquid flow rate $\dot{N}_{\mathrm{L}}$ and the distillate flow rate (top product) $\dot{N}_{\mathrm{D}}$. When no top or bottom products are withdrawn from the system, $\dot{N}_{\mathrm{D}}$ approaches zero. The system then operates at infinite reflux (or total reflux).

2.1.2 Assessment of Separation Efficiency

The most established method to assess separation efficiency in rectification columns is the concept of theoretical plates developed by McCabe and Thiele [50]. They published a graphical method to determine the number of plates depending on the thermal condition of the feed, the reflux ratio, and the desired top and bottom product composition. For a system at infinite reflux, an exemplary graphical construction of the number of plates of a column is shown in Figure 2.1. The $\widetilde{x}$,$\widetilde{y}$-diagram correlates the composition of the vapor (mole fraction $\widetilde{y}$) to the composition of the liquid (mole fraction $\widetilde{x}$) in equilibrium at a specific pressure.

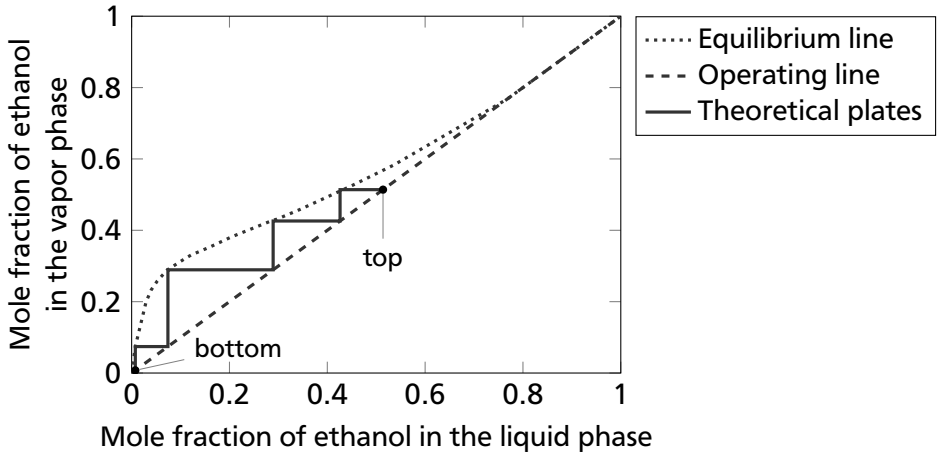

Figure 2.1: $\widetilde{x}$,$\widetilde{y}$-diagram of the binary system ethanol-water at a pressure of 1013 mbar with construction of theoretical plates at infinite reflux with vapor-liquid equilibrium data from Carey and Lewis [12]

The number of theoretical plates N can be graphically determined through the construction of steps between the equilibrium line and the operating line. For a system at infinite reflux, the construction of the operating line is simpler than for finite refluxes. The thermal condition of the feed is not relevant and the operating line equals the bisectrix. For the system shown in Figure 2.1, the number of theoretical plates would be at a value of four. The diagram does not include any information about the height of a column. To compare the efficiency of rectification processes, the height equivalent to a theoretical plate can be

calculated. Dividing the height of the apparatus h by the number of theoretical plates N gives the height equivalent to a theoretical plate

$$HETP = \frac{h}{N}. \tag{2.2}$$

Thus, this value gives information about the space, which is needed for a separation equal to one theoretical plate. In conventional macro scale rectification columns *HETP*-values between 300 mm and 600 mm are commonly reached [33].

2.2 Micro Distillation

In micro separation processes, the fluid flow is guided through micro structures [33]. Sundberg *et al.* [77] reviewed publications on micro distillation processes and categorized them in concurrent (single stage) and counter current processes (fractionating distillation). This is in accordance with the distinction commonly made for macro scale distillation processes.

In concurrent devices the liquid and vapor phase flow in the same direction, thereby only a separation of one single stage can be achieved. If the liquid and vapor phase flow counter currently, the separation efficiency can increase due to composition gradients in both phases, which lead to an enhanced mass transfer. The efficiency of micro distillation processes is usually evaluated in terms of the number of theoretical stages or the height equivalent to a theoretical plate *HETP*.

Sundberg *et al.* [77] stated that recurring issues with the apparatuses were concentration fluctuations evoked by unstable temperature profiles or the difficulty of controlling the pressure drop over the capillary structures. They concluded that gravitational forces were too weak in micro channels and, thus, micro distillation processes utilizing capillary forces were superior to processes utilizing gravitational forces.

2.2.1 Relevant Dimensionless Numbers

In micro distillation systems, momentum transport, heat transfer, and mass transfer are coupled. To characterize these transport processes in the system, three dimensionless numbers are introduced: the Reynolds number *Re*, the Péclet number for heat transfer *Pe*, and the Péclet number for mass transfer Pe'. In many cases, fluidic systems are only characterized by one value for each dimensionless number. For the system investigated in this work, dimensionless numbers in different coordinate directions need to be determined. Here, all dimensionless numbers are exemplarily defined in the direction of z with the characteristic velocity w. The Reynolds number is used in fluid mechanics to evaluate the ratio of the inertial forces to the viscous forces. It is defined through

$$Re_z = \frac{L\, w \rho}{\mu} \tag{2.3}$$

with the characteristic length L, the density ρ, and the dynamic viscosity μ. The Péclet number for heat transfer Pe describes the ratio of convective heat transfer to conductive heat transfer

$$Pe_z = \frac{L\,w}{a}, \tag{2.4}$$

where a is the thermal diffusivity. With the diffusion coefficient D, the Péclet number for mass transfer Pe' describes the ratio of convective mass transfer to diffusive mass transfer

$$Pe'_z = \frac{L\,w}{D}. \tag{2.5}$$

With two further dimensionless numbers correlating only fluid properties, the Prandtl number

$$Pr = \frac{\mu}{\rho\,a} \tag{2.6}$$

and the Schmidt number

$$Sc = \frac{\mu}{\rho\,D}, \tag{2.7}$$

the Péclet numbers can be connected to the Reynolds number. The Péclet number for heat transfer can be determined through the multiplication of the Prandtl number Pr and the Reynolds number

$$Pe_z = Pr\,Re_z. \tag{2.8}$$

Accordingly, the Péclet number for mass transfer can be determined through the multiplication of the Schmidt number Sc and the Reynolds number

$$Pe'_z = Sc\,Re_z. \tag{2.9}$$

2.2.2 Micro Distillation Concepts

Different micro distillation concepts investigated in the past are introduced in this section. Schematics of these are presented in Figure 2.2. Concepts utilizing concurrent flow are distillation with utilization of a carrier gas and bubble assisted distillation. Concepts utilizing counter current flow are membrane distillation, micro channel distillation, sieve-tray micro rectification, and rotating micro channel distillation.

Concurrent distillation processes using a carrier gas to establish fluid flow were investigated by Wootton and deMello [84] and Hartman *et al.* [25, 26] (Figure 2.2a). In this concept, the feed is driven through a micro channel together with a carrier gas. At the end of the channel, the liquid and vapor phases are separated. Hartman *et al.* [25] separate the phases with a membrane, Wootton and deMello [84] separate

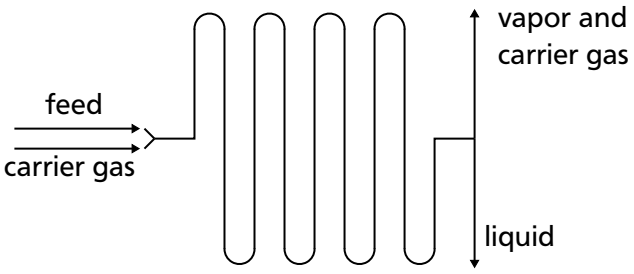

(a) Concurrent distillation with carrier gas (adapted from [25])

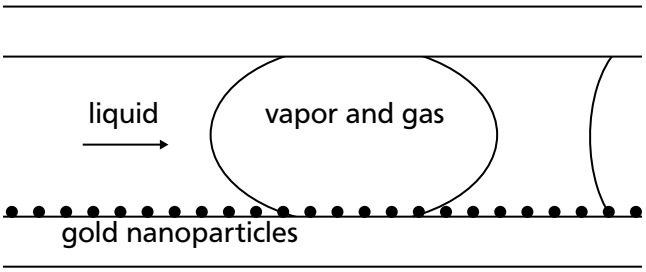

(b) Concurrent bubble assisted distillation (adapted from [8])

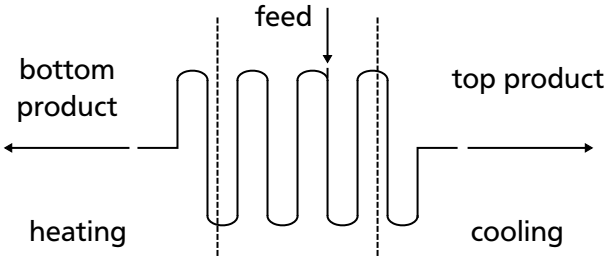

(c) Micro channel distillation (adapted from [39])

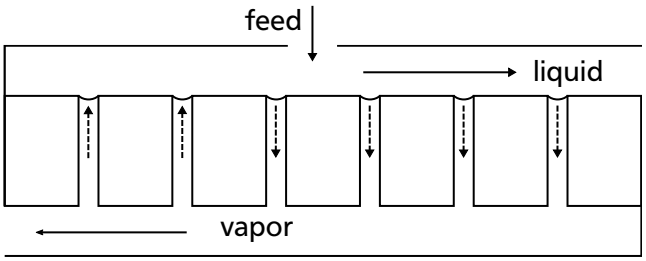

(d) Membrane distillation (adapted from [87])

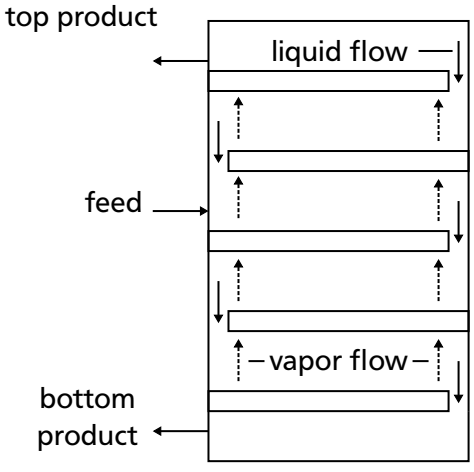

(e) Sieve-tray micro rectification (adapted from [90])

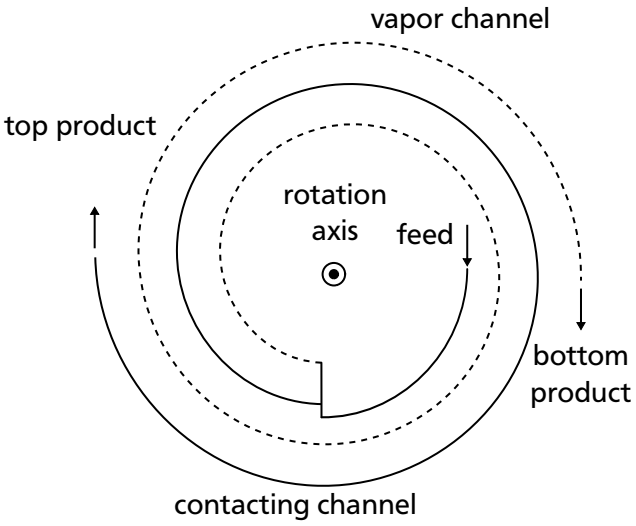

(f) Rotating micro channel distillation (adapted from [48])

Figure 2.2: Different micro distillation concepts

the phases with a “separation module”, which is not further specified. Wootton and deMello [84] used a mixture of acetonitrile and dimethylformamide and helium as carrier gas. With the described apparatus, a separation equal to 0.72 theoretical plates was achieved. Hartman *et al.* [25] tested their device with nitrogen as carrier gas and with equimolar methanol-toluene and dichloromethane-toluene mixtures at 70 °C. Analyzed with a gas chromatograph, a methanol fraction of 0.79 and a dichloromethane fraction of 0.63 were measured in the vapor phase. Hartman *et al.* [26] further investigated the previously introduced process as part of a chemical synthesis process with multiple steps. Aryl triflate was mixed with toluene or dimethylformamide and afterwards with gaseous nitrogen in order to establish gas-liquid segmented flow. Controlling the temperature in the device between the feed components boiling points led to an enrichment of the vapor phase with the more volatile component. Nuclear magnetic resonance (NMR) spectroscopy was used to determine the composition and concentrations of the components in the flows exiting the chamber.

Boyd *et al.* [8] developed the concept of distillation through bubble-assisted interphase mass transfer (Figure 2.2b). A gas bubble was trapped in a channel of 30 µm diameter. Gold nanoparticles at the walls of the channel were heated by a laser. This caused the liquid supplied from the left in the schematic to evaporate and the vapor to condense at the other end of the gas bubble without active cooling, thereby a single-stage distillation could be achieved, which could be followed by further distillation steps. No carrier gas is needed in this case to transport the fluid.

Micro channel distillation was investigated by Zheng *et al.* [89], Lam *et al.* [39, 40], Foerster *et al.* [19] and Ju *et al.* [32] (Figure 2.2c). In this concept, a feed is introduced at varying positions in the micro channel. A temperature profile in the micro channel is established through heating one end and cooling the other end of the micro channel. The more volatile component of the mixture is withdrawn from the micro channel at the cooler end, whereas the less volatile component is withdrawn at the warmer end of the micro channel. Lam *et al.* [39] investigated micro channel distillation and established a reflux of liquid through capillary flows in micro pillars in the wall region of the channel, thereby inducing a counter current flow of liquid phase and vapor phase. Methanol-toluene and acetone-water mixtures were used as fluids. Different setups of the micro channels and the capillary structures were tested and the separation performance was evaluated. Compared to a straight or a zig-zag micro channel, a serpentine-shaped micro channel led to the best separation performance. A relevant issue was to avoid flooding of the micro channel in the case of comparatively long micro channels, which can be achieved through additional capillary structures. Lam *et al.* [40] further analyzed the design and operational parameters of the previously introduced geometry of a serpentine-shaped micro channel with an acetone-water mixture. The feed was introduced into the micro channel at a quarter of the length of the micro channel from the heated end. It was found that increasing the temperature at the heated end improved the separation performance as well as decreasing the temperature at the cooled end. Both temperature adaptations led to a higher liquid reflux in the capillary structures, thereby improving the mass transfer between liquid and vapor phase. The feed composition was varied. Decreasing the percentage of the more volatile component in the feed led to a lower number of theoretical stages. Lam *et al.* [40] assume that the significant decrease in separation efficiency for the micro distillation apparatus is due to a decrease in reflux ratio induced by the changed feed composition. The reflux ratio of the investigated micro distillation column was strongly dependent on the feed composition. Foerster *et al.* [19] followed the

work of Lam *et al.* [39, 40] and investigated the distillation of toluene-benzaldehyde mixtures in a micro channel with a length of 400 mm, a width of 600 µm and a depth of 300 µm. Additionally, they integrated Raman spectroscopy to evaluate the local fluid composition in the system and infrared thermography to evaluate the temperatures of the system on the outside. According to the authors, the uncertainty of the composition measurements through Raman spectroscopy was at 3 mole-%. The number of stages was between 0.9 and 2.7, calculated under the assumption of total reflux. Depending on the operating parameters, separation zones of different lengths were determined through the Raman spectroscopy measurements. The authors concluded that the optimization process of the operating parameters strongly depended on the specific requirements and target values of the distillation to be executed. Zheng *et al.* [89] and Huang *et al.* [31] investigated counter current micro channel distillation as part of a refinement process of JP-8 fuel. The distillation led to a reduction in sulfur components in the fuel and could thereby improve the overall hydrodesulfurization process.

Membrane distillation was investigated by Zhang *et al.* [87] and Adiche and Sundmacher [6] (Figure 2.2d). In this concept, liquid and vapor flow are separated by a membrane. The position of the heat input varies within this concept and is therefore not shown in Figure 2.2d. Adiche and Sundmacher [6] investigated sweep gas membrane distillation with methanol-water mixtures. In the liquid channel, a feed at flow rates between 8 ml min^{-1} and 30 ml min^{-1} was fed and in the vapor channel a gas stream was fed, which swept the fluid out of the membrane. The concept could be operated in concurrent and counter current mode. No *HETP* values were given. Zhang *et al.* [87] investigated counter current vacuum membrane distillation of a water methanol mixture on a chip. The liquid flowed counter currently to the vapor but was separated from it by a polytetrafluorethylene membrane. Heat was supplied to the vapor phase, while the cooling flow of water was led in a parallel direction to the liquid flow. Thus, temperature gradients were generated between the vapor and liquid phase and inside the vapor and liquid phase. This led to a separation equivalent to 1.7 theoretical stages. Zhang *et al.* [88] then investigated the influence of temperature gradients, feed composition, feed flow rate, and membrane pore size on the distillation efficiency. For optimized operating parameters, the number of theoretical stages could be increased to 1.8. Feed flow rates up to 12 µl min^{-1} were reached.

Ziogas *et al.* [90] developed a micro rectification apparatus, which is built similarly to large industrial rectification apparatuses, but on a smaller scale (Figure 2.2e). The apparatus could be used in batch, semi-batch, and continuous operation mode. Binary mixtures tested in batch operation were equimolar acetone-n-butanol, equimolar toluene-o-xylene, and 48.55/51.45 mole-% i-octane-n-octane mixtures at infinite reflux ratio. Distillate flows of 99.95 mole-% acetone (five theoretical plates), 92.3 mole-% toluene (five theoretical plates), and 96.06 mole-% i-octane (twelve theoretical plates) were achieved. Additionally, an equimolar p-xylene-o-xylene mixture was tested in continuous operation mode.

MacInnes *et al.* [48] developed a rotating spiral micro channel distillation apparatus (Figure 2.2f). The feed is fed in the center of the spiral. The fluid flows along the micro channel. Through increasing temperature and thereby increasing the pressure along the contacting channel, a counter current vapor flow towards the center of the spiral is established. The rotational movement ensures a separation of the two phases. For the tested 2,2-dimethylbutane 2-methyl-2-butene mixture a separation of seven to fifteen ideal stages is achieved depending on the ratio of the top to the bottom product. The height equivalent to a theoretical plate is estimated to be at 5.3 mm.

2.3 Zero-Gravity Distillation

Another micro distillation concept is zero-gravity distillation. Commonly, the term is used to describe distillation in an apparatus similar to a heat pipe. Due to the fluid flow utilizing capillary forces, the process can be performed independently of gravity. In the following sections, the working principle of zero-gravity distillation based on heat pipes and relevant past research is described.

2.3.1 Working Principle of Heat Pipes

Heat pipes are heat transfer devices, which can transport comparably high heat flows. From the outside, heat pipes are heat conductors with a hot and a cold end. On the inside, a fluid circulates in the heat pipe and continuously evaporates and condenses. The hot end is where the circulating fluid evaporates and the cold end is where the evaporated vapor condenses. A pressure difference is needed to sustain the fluid flow. Heat pipes work without pumps. The pressure difference is supplied through a changing capillary pressure difference between vapor and liquid phase; therefore, the liquid flow is guided through capillary structures. An example distribution of the pressure in heat pipes is shown in Figure 2.3. The pressure in the vapor phase is always higher than in the liquid phase at the same axial position in the heat pipe. In the direction of flow, the pressure decreases. Thus, the vapor pressure decreases from the evaporator to the condenser and the liquid pressure decreases from the condenser to the evaporator. This implies that the capillary pressure between the vapor and the liquid phase is the highest in the evaporator section.

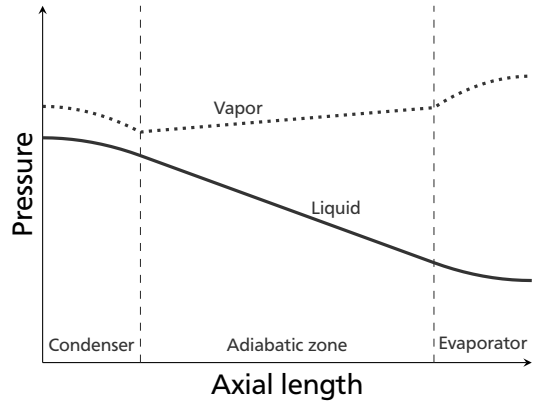

Figure 2.3: Pressure distribution in heat pipes (adapted from [82])

Many heat pipes use axial channels as capillary structures. Due to its comparatively small influence on the capillary pressure, the curvature of the fluid interface in axial direction can be neglected when calculating the capillary pressure in these channels. In this case the capillary pressure p_C is defined as

$$p_C = \frac{\sigma}{R} = \sigma C. \tag{2.10}$$

Here, σ is the surface tension of the fluid, R is the curvature radius of the interface, and C is the curvature of the interface. If the interface temperature does not change, the surface tension of a one-component fluid remains constant in a heat pipe. Thus, the curvature radius of the interface needs to decrease from

the condenser to the evaporator. Depending on the inclination of the heat pipe, gravity can either support the liquid flow from the condenser to the evaporator or deplete the liquid flow.

In Figure 2.4, the operational limits for heat pipes are shown. Heat pipes can be operated between the melting temperature T_{melt} and the critical temperature T_{crit} of the working fluid. If the combination of capillary structures and fluid does not permit a sufficient capillary pressure difference, a dry-out of the capillary structure in the evaporator section occurs. This causes a deteriorating cooling duty and is called the capillary limit. The boiling limit is reached, when nucleate boiling occurs in the capillary structure, which can destabilize the process. The viscosity limit, sonic limit, and reciprocation limit are not relevant within the scope of this work.

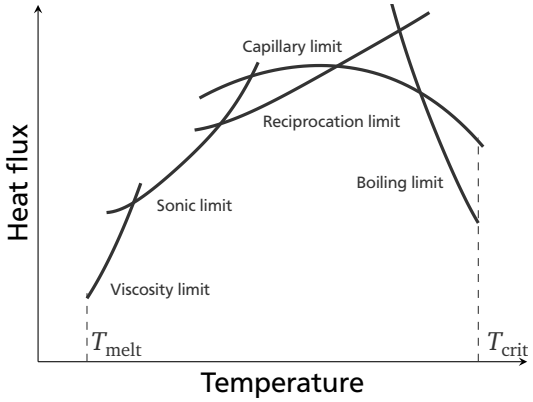

Figure 2.4: Operational limits of heat pipes (adapted from [82])

2.3.2 Transport Processes in Heat Pipes

To optimize heat pipes and evaluate the influence of operating parameters, heat transfer and fluid transport in heat pipes need to be described. To this purpose, theoretical models were developed and experiments were conducted. These led to the design of advanced capillary structures, which aim to optimize heat transfer and fluid transport in heat pipes. As described previously, the capillary pressure in heat pipes is dependent on the curvature radius of the liquid-vapor interface. To validate theoretical models, measurements were conducted to characterize the shape of the liquid-vapor interface. The state of the art on transport processes in heat pipes, advanced capillary structures, and measurements of the liquid-vapor interface shape in heat pipes is described in this section.

In heat pipe evaporators, the liquid evaporates at curved interfaces. In these cases, a relevant amount of heat is transferred in the vicinity of the apparent three-phase contact line, where solid, liquid, and vapor phase are in contact with each other. On a microscopic scale, the meniscus can be divided into three parts according to Potash Jr. and Wayner Jr. [52]: the macro region, the micro region, and the adsorbed film. In the macro region, the curvature of the interface is constant. Adjacent to the macro region is the micro region in which the curvature changes rapidly from the macroscopic curvature to zero. In the adjacent adsorbed film the curvature is zero. The liquid is adsorbed at the solid and the adhesion forces are too high to allow evaporation in this region. In the macro and micro region evaporation occurs. In the macro region, the temperature at the interface can be assumed to be the saturation temperature. In the micro region, the temperature of the interface is higher than the saturation temperature. Intermolecular forces

and the resistance of the liquid-vapor interface need to be taken into account. The momentum balance, energy balance, and mass balance lead to a system of four coupled differential equations in the micro region. To evaluate heat transfer in the evaporator of heat pipes, Stephan and Busse [71] introduced an iteration procedure between the heat transfer in the micro region and in the macro region. Integrating the micro region model into heat pipe evaporator calculations can lead to more exact forecasts of the heat transfer coefficient [71].

Xu and Carey [86] investigated evaporation from a triangular groove. They described the axial flow in the groove by balances for impulse and mass. Brandt *et al.* [10] developed a model, which combines heat transfer in the evaporator of heat pipes based on Stephan and Busse [71] with axial fluid transport in heat pipes based on Xu and Carey [86]. With this model, Brandt *et al.* [10] were able to predict the curvature distribution and heat transfer coefficients in heat pipes. A detailed description of the calculation process can be found in [9]. Größmann [14] used a similar model to calculate heat transfer coefficients in heat pipe evaporators.

To improve the heat transfer capabilities of heat pipes, capillary structures are optimized. The main focuses are to increase the boiling and the capillary limit. The structures investigated are mainly based on axial channels. A high capillary pressure and a low viscous pressure drop are desirable. Whereas a high capillary pressure demands a narrow channel, a low viscous pressure drop demands a wide channel diameter [66].

Schlitt [65] suggested varying the width of axially grooved channels along the flow direction. Since a high capillary pressure is only needed in the evaporator zone, the channels in the evaporator zone should be narrower than those in the adiabatic transport zone. This decreases the pressure drop in the adiabatic zone. Richter *et al.* [55] developed an “advanced trapezoidal axially grooved (ATAG) heat pipe”. This capillary structure consisted of a trapezoidal cross section where the opening width was lower than the bottom width. Harwell *et al.* [27] first published the concept of re-entrant channels. The re-entrant channel combines a circular cross section with a rectangular cross section. The rectangular cross section of comparatively small area connects the circular main channel to the vapor region. The small width of the open rectangle provides a high capillary pressure, whereas the larger diameter of the circular section provides a large cross-sectional area. Re-entrant channels were later also tested in the framework of a European Space Agency program [17]. In Figure 2.5, the design of a re-entrant channel and different improvements are shown. Stephan and Brandt [72] investigated advanced re-entrant structures with micro grooves perpendicular to the axial channels in the evaporator zone of their heat pipe (Figure 2.5b). Keeping the dimensions of the re-entrant grooves constant, the length scales of these perpendicular micro grooves were optimized. The addition of micro grooves led to a significant increase in heat transfer capabilities of the heat pipes. The reason for this was argued to be the increased length of the three-phase contact line, which led to an increased micro region evaporation. This heat pipe design was also tested in space [67]. Größmann [14] improved this concept in a setup with an external condenser. He focused on pointedly varying the parameters of contact line length and surface of the liquid-vapor interface in the evaporator. As a further advancement in capillary structure development, he firstly added further micro channels parallel to the main re-entrant channels (Figure 2.5c). Secondly, he added sintered structures between the re-entrant channels (Figure 2.5d). He was able to further increase the heat transfer coefficient. For the sintered structure, the parameters contact line length and liquid-vapor interface could

not be exactly described. Größmann [14] compared the heat transfer coefficients obtained with these structures for methanol and acetone at different heat fluxes, varied saturation temperatures, and different partial pressures of non-condensable gases. The heat transfer coefficient increased with decreasing heat fluxes and increasing saturation temperatures.

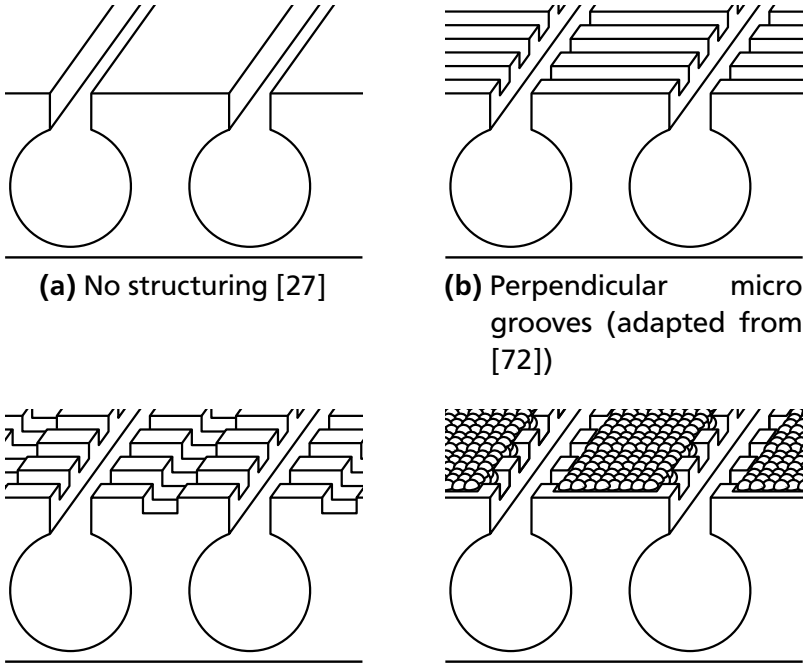

(a) No structuring [27]

(b) Perpendicular micro grooves (adapted from [72])

(c) Perpendicular and axial micro grooves (adapted from [14])

(d) Sintered structuring [14]

Figure 2.5: Variations of surface structuring for re-entrant channel structures

To validate a theoretical model on the curvature distribution in heat pipes, the research group of Lefèvre published multiple papers in which the interface curvature in flat heat pipes was measured with confocal spectroscopy [41–43, 46, 47, 54, 58]. The model used is similar to the one suggested by Brandt *et al.* [10]. Rullière *et al.* [58] first used confocal spectroscopy to compare measured curvature radii in an axially grooved heat pipe with the results of simulations. The grooves had a rectangular cross section with an opening width of 400 µm. The three-phase contact line was assumed to be pinned over the whole length of the heat pipe. Measurements and simulations of curvature radii were in good agreement with each other. Furthermore, a macroscopic thermal model was added for the evaporator, condenser, and adiabatic section separately [41]. The model for the condenser also accounted for condensation and liquid film formation on the fins between the axial grooves. The flow and thermal models were coupled and solved iteratively. The results were used to optimize the number of grooves and the groove dimensions of rectangular grooves of a flat heat pipe. Revellin *et al.* [54] improved the thermal model and additionally developed correlations for the equivalent thermal conductivities during evaporation and condensation. The same group then focused on measuring the film thickness on the fins between the axial grooves [42]. The film on the fins exhibited an inverted curvature compared to the menisci in the grooves. Based on the measured decrease of the curvature radius on the fins from the condenser to the evaporator, Lefèvre *et al.* [42] concluded that a liquid backflow from the evaporator to the condenser existed on the fins.

Furrer *et al.* [21] presented a different method to capture the liquid-vapor interface shape in axial channels. In their system, a camera is positioned normal to the main flow direction of a groove. The liquid-vapor interface is illuminated with a laser sheet at a fixed axial position, which allows the camera to detect a sharp image of the interface. Savino *et al.* [60] tested the system on a grooved heat pipe with triangular cross section. According to the authors, the curvature radius could be determined between 1 mm and 10 mm with an uncertainty below 5 %.

2.3.3 Influence of Fluid Mixtures on Transport Processes in Heat Pipes

When filling heat pipes with a non-azeotropic binary mixture, a distillation process will be established. Due to the different boiling points of the components, the less volatile component will agglomerate at the evaporator and the more volatile component will agglomerate at the condenser. The local fluid composition will depend on the axial position in the heat pipe. The fluid properties are dependent on the local composition of the fluid in the apparatus. This includes the surface tension, the viscosity, the density, and, in terms of fluid-solid interaction, the wettability. Compared to one-component fluids, this implies that the change in capillary pressure along the heat pipe main axis can be established through a change in curvature and also in local surface tension. Additionally, a Marangoni flow can support the liquid flow from the condenser to the evaporator, if the surface tension of the less volatile component is higher than the surface tension of the more volatile component. For one-component fluids, mostly a Marangoni flow from the evaporator to the condenser exists since the surface tension decreases with increasing temperature for most of the fluids. This is not desirable for heat pipe operation. For this reason binary mixtures are a focus of heat pipe research.

Kuramae and Suzuki [38] experimentally investigated horizontal heat pipes without capillary structures with a water-ethanol mixture. The scope of this research was to test heat pipes which are more suitable for space applications than existing concepts and, therefore, to refrain from using capillary structures due to anticipated difficulties in manufacturing and restrictions of the maximum transferable heat. The flow of the liquid back to the evaporator was established through the Marangoni effect. Three different compositions of the mixture (0 mole-%, 5 mole-%, and 85 mole-% ethanol) were tested. The heat pipes were put in a dropping capsule in order to create a micro gravity environment. Whereas a dryout of the evaporator section occurred for pure water and for the 85 mole-% ethanol mixture, a reflux was established for the 5 mole-% ethanol mixture. To the author's knowledge, Kuramae and Suzuki [38] were the first authors who utilized Marangoni flows to prevent heat pipes from drying out.

Abe [1] considers fluids to be self-rewetting if the surface tension increases with temperature and, at the same time, the more volatile component has a lower surface tension than the less volatile component. Both of these characteristics lead to a strong tendency of the fluid to rewet dry surfaces in heat pipes or during nucleate boiling [1]. In Figure 2.6, the described behaviour is illustrated. In Figure 2.6a, the surface tensions are shown at different temperatures for different alcohols dissolved in water. Different mixtures exhibit local minima of the surface tension. In Figure 2.6b, the vapor-liquid equilibrium of water-butanol mixtures is shown. For mole frations of water higher than the azeotropic point, the surface tension of the less volatile component is lower than the surface tension of the more volatile component. Examples for self-rewetting fluids are mixtures of water and alcohols with four to ten carbon atoms [1].

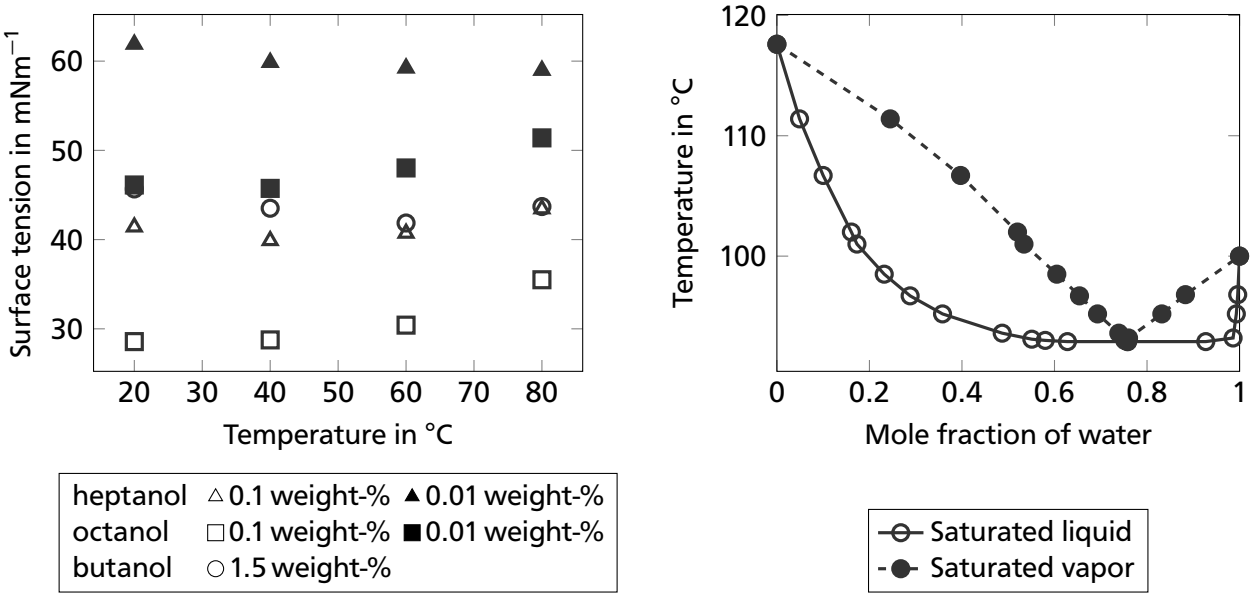

(a) Surface tension of aqueous alcohol solutions (adapted from Francescantonio *et al.* [20])

(b) Experimentally determined vapor-liquid equilibrium of water-butanol mixtures at a pressure of 1013 mbar from [22]

Figure 2.6: Measured surface tension of self-rewetting fluids (a) and vapor-liquid equilibrium of water-butanol mixtures (b)

The group of Abe investigated wicked and wickless heat pipes with binary mixtures under micro gravity conditions and on earth [2–5]. The dryout limit of wickless heat pipes could be increased with butanol-water mixtures (self-rewetting) compared to ethanol-water mixtures (not self-rewetting) [1]. Savino and Paterna [59] reached a similar conclusion when analytically investigating the influence of the Marangoni effect on the dryout of heat pipes with binary mixtures.

The group of Savino conducted further experimental and analytical studies regarding self-rewetting fluids in heat pipes. For wicked and wickless heat pipes on earth and under micro gravity the improved dryout limit of heat pipes with self-rewetting fluids was confirmed [20, 61, 62]. Recently, self-rewetting fluids have also been used in pulsating heat pipes in a parabolic flight [13] and on earth [30]. Additionally, ternary mixtures, brines with additions of alcohols, and suspensions of self-rewetting fluids and nano particles were identified as possible self-rewetting fluids [16, 63, 64].

The above mentioned micro region model relevant in heat pipe evaporators was also extended for binary mixtures by Kern and Stephan [35] and applied to nucleate boiling. In addition to the momentum balance, energy balance, and overall mass balance, mass balances for every component were formulated. Kern and Stephan [34] also evaluated the influence of different mixture effects on the micro region model for a mixture of propane and n-butane. The micro region heat transfer including all mixture effects was 30 % to 40 % lower in these calculations than for the case with averaged fluid properties. The change in saturation temperature over the length of the micro region was the most influential effect.

2.3.4 State of the Art on Zero-Gravity Distillation

In the following section, the state of the art on zero-gravity distillation is presented. The section is divided in experimental and theoretical studies.

Experimental Studies

Seok and Hwang [68] investigated a continuous zero-gravity distillation process. The more volatile component (top product) is discharged at the cooled condenser section whereas the less volatile component (bottom product) is discharged at the heated evaporator section. A binary mixture of fluid is continuously supplied to the adiabatic zone in between. In Figure 2.7 a schematic of the apparatus is shown.

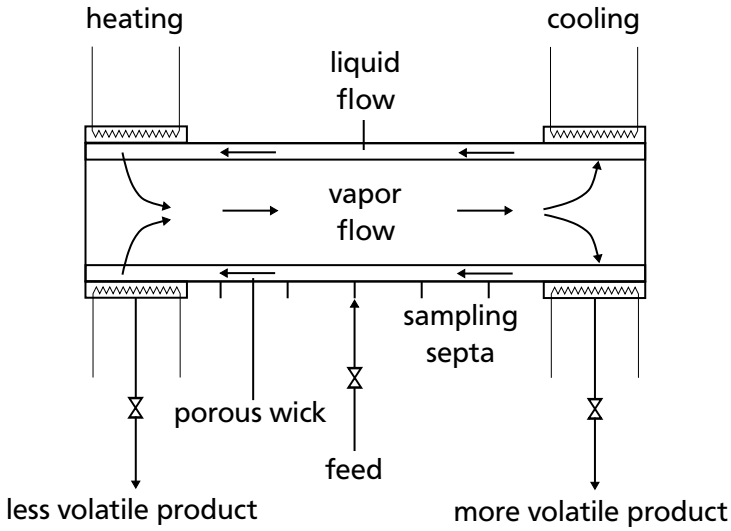

Figure 2.7: Schematic of the zero-gravity distillation apparatus investigated by Seok and Hwang [68] (adapted from [68])

The fluids used by Seok and Hwang [68] were ethanol-water and methanol-water mixtures of different compositions. The condenser and the evaporator were fabricated of copper, the adiabatic separation zone was made of a glass pipe and the capillary structures were made of fiber glass. The temperature at the evaporator section was held slightly below the boiling temperature of the mixture. According to Seok and Hwang [68], the experimental data obtained were in good agreement with the numerically predicted concentration profiles of the mixture. The measured and modeled composition profiles are shown in Figure 2.8. It can be seen that the separation of the components takes place predominantly between the evaporator and the condenser. This area is called the adiabatic separation zone. Seok and Hwang [68] observed that a greater reflux ratio resulted in a greater separation efficiency. The model developed by Seok and Hwang [68] is described in the following section on theoretical studies.

Sundberg *et al.* [74] developed a new zero-gravity distillation apparatus. Due to its high porosity, good wettability, high specific surface area, and its high permeability, metal foam was chosen as the porous medium. Three different distillation columns were tested with lengths from 140 mm to 500 mm. Those three columns varied in their dimensions, in the metal foams used as porous media, and in the way the

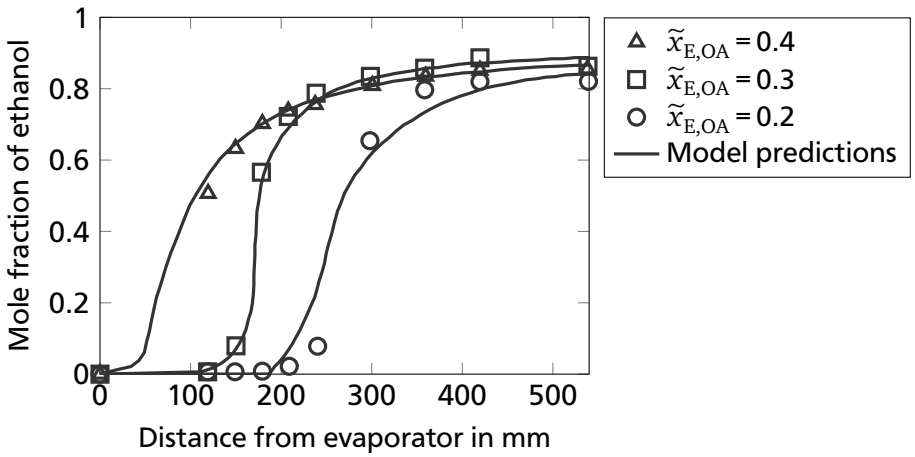

Figure 2.8: Composition profiles in the zero-gravity distillation apparatus investigated by Seok and Hwang [68] for water-ethanol mixtures with different overall average mole fractions of ethanol $\widetilde{x}_{E,OA}$ (adapted from [68])

heating and cooling of the different sections of the column were constructed. The fluid Sundberg *et al.* [74] mainly used was an equimolar n-hexane-cyclohexane mixture. Additionally, a mixture of n-hexane, cyclohexane, and toluene was tested. The temperatures at the evaporator and condenser section were kept at the respective boiling temperatures of the pure compounds of the mixture. Overall, a stable operation of the apparatuses was observed. A height equivalent to a theoretical plate of 13 mm (electrically heated at the warm end and temperature controlled by water at the cold end) and 25 mm (electrically heated at both ends) at total reflux was obtained.

Sundberg *et al.* [75] further improved the design of one of the investigated apparatuses (electrically heated at both ends) and thereby improved the *HETP* from 25 mm to 16 mm. This was achieved through complete reduction of the space above the metal foam. This led to the vapor flowing back to the evaporator through the porous structures, thereby enhancing the heat and mass transfer between liquid and vapor phase. Additionally, the heating duty was optimized in order to obtain the highest separation efficiency.

Sundberg *et al.* [76] also developed a micro distillation column with an external reboiler and an external condenser. The focus of these experiments was to determine how much heat was used for evaporating the fluid and how much heat was used to compensate for heat losses of the column. Based on the formulated conservation of energy, heat losses for different pure components were calculated from measured data. Linear dependences of the heat losses on the temperature difference between the column walls and the fluids were found. Through optimizing the apparatus' temperature the column could then be operated more efficiently.

Theoretical Studies

The transport processes in zero-gravity distillation were modeled by Seok and Hwang [68], Ramirez-Gonzalez *et al.* [53], Tschernjaew *et al.* [80], and Rieks *et al.* [56, 57]. The main assumptions and the formulations of the governing equations are presented in this section.

All the presented models use Darcy's law for the description of the liquid flow within the porous wick. Darcy's law can be used for creeping flows in porous media. For creeping flows, the viscous forces

outweigh the inertial forces and the Reynolds number is much smaller than one. Darcy's law correlates the velocity to the derivative of the pressure p according to

$$w = -\frac{P}{\mu}\frac{\mathrm{d}p}{\mathrm{d}z}. \tag{2.11}$$

Here, P is the permeability of the porous medium. The velocity w is not the velocity in the pores but is calculated from the volume flow rate divided by the entire flow area including the solid porous medium.

Seok and Hwang [68] only modeled the adiabatic separation zone based on a model of two-component heat pipes of Tien and Rohani [78]. To account for the influence of the evaporator and the condenser, they defined an effective length of the column. This length is the sum of the length of the adiabatic zone and half of the length of the condenser and evaporator zone. They did not assume a constant vapor flow rate. The derivative of the molar flow rate of component A (overall vapor flow rate $\dot{N}_\mathrm{V}$, vapor mole fraction $\widetilde{y}_\mathrm{A}$) in the vapor phase in the axial direction z is defined by

$$\frac{\mathrm{d}\left(\dot{N}_\mathrm{V}\,\widetilde{y}_\mathrm{A}\right)}{\mathrm{d}z} = K_\mathrm{V}\,S\,A_\mathrm{V}\left(\widetilde{y}_\mathrm{A,int} - \widetilde{y}_\mathrm{A}\right). \tag{2.12}$$

Here, K_V is an overall mass transfer coefficient which is assumed constant due to the low vapor flow rates and only accounts for diffusion. A_V denotes the cross sectional area in the vapor channel and S is the specific interfacial area. The vapor mole fraction at the interface $\widetilde{y}_\mathrm{A,int}$ is assumed to be equal to the equilibrium mole fraction. Additionally, the energy balance in the adiabatic zone is formulated as

$$0 = \Delta\widetilde{h}_\mathrm{LV,A}\frac{\mathrm{d}\left(\dot{N}_\mathrm{V}\,\widetilde{y}_\mathrm{A}\right)}{\mathrm{d}z} + \Delta\widetilde{h}_\mathrm{LV,B}\frac{\mathrm{d}\left(\dot{N}_\mathrm{V}\,(1-\widetilde{y}_\mathrm{A})\right)}{\mathrm{d}z} \tag{2.13}$$

with the molar enthalpies of evaporation of component A and B $\Delta\widetilde{h}_{\mathrm{LV},i}$. Combining both differential equations and eliminating $\frac{\mathrm{d}\dot{N}_\mathrm{V}}{\mathrm{d}z}$, the resulting equation can be solved for $\widetilde{y}_\mathrm{A}$ with the boundary condition of a pure less volatile component at the evaporator. The maximum flow rate was either calculated from the capillary limit of the system or fitted to the experimental data. In the first case, Darcy's law is used to determine the capillary limit for a given heat flow.

The models of Ramirez-Gonzalez *et al.* [53] and Tschernjaew *et al.* [80] also include the liquid phase. Ramirez-Gonzalez *et al.* [53] formulated the mass balance equations and solved these for the adiabatic separation zone only. The temperatures and compositions of the mixtures in the evaporator and condenser are reflected in the model as boundary conditions. For the liquid phase the conservation of mass for component A is formulated as

$$D_\mathrm{L}\frac{\mathrm{d}^2\widetilde{x}_\mathrm{A}}{\mathrm{d}z^2} + \frac{\mathrm{d}\widetilde{x}_\mathrm{A}}{\mathrm{d}z}\frac{\mathrm{d}D_\mathrm{L}}{\mathrm{d}z} - w_\mathrm{L}\frac{\mathrm{d}\widetilde{x}_\mathrm{A}}{\mathrm{d}z} - \frac{2R_\mathrm{O}\,k_\mathrm{L}}{R_\mathrm{O}^2 - R_\mathrm{I}^2}(\widetilde{x}_\mathrm{A} - \widetilde{x}_\mathrm{A,int}) = 0. \tag{2.14}$$

For the vapor phase the conservation of mass for component A is formulated as

$$-D_{\mathrm{V}}\frac{\mathrm{d}^2\widetilde{y}_{\mathrm{A}}}{\mathrm{d}z^2}-w_{\mathrm{V}}\frac{\mathrm{d}\widetilde{y}_{\mathrm{A}}}{\mathrm{d}z}-\frac{2\,k_{\mathrm{V}}}{R_{\mathrm{I}}}(\widetilde{y}_{\mathrm{A,int}}-\widetilde{y}_{\mathrm{A}})=0. \tag{2.15}$$

Here, $\widetilde{x}_{\mathrm{A}}$ is the liquid mole fraction of component A, k_{V} is the mass transfer coefficient in the vapor phase, and R_{I} is the radius of the pipe excluding the porous structure whereas R_{O} is the radius including the porous structure. The effective diffusion coefficient in the liquid phase D_{L} is corrected for a porous medium. Since the composition of the mixture changes, the diffusion coefficient also changes dependent on the position in the column in the liquid phase. For the vapor phase, the diffusion coefficient is assumed to be constant. The liquid velocity is determined through Darcy's law and the Young-Laplace equation, assuming perfectly wetted walls and an effective pore radius. To calculate the mass transfer coefficients, Ramirez-Gonzalez *et al.* [53] use correlations. For the liquid phase, a correlation for turbulent flow is used since this led to a better fit of the theoretical results to experimental data from Seok and Hwang [68].

Tschernjaew *et al.* [80] developed a two-dimensional model to describe the radial and axial concentration profiles in a zero-gravity distillation apparatus. The equations implemented in the model are the component balance for component A in the liquid phase

$$D_{\mathrm{L}}\frac{\partial^2\widetilde{x}_{\mathrm{A}}}{\partial r^2}-w_{\mathrm{L}}\frac{\partial\widetilde{x}_{\mathrm{A}}}{\partial z}=0 \tag{2.16}$$

and in the vapor phase

$$D_{\mathrm{V}}\frac{\partial^2\widetilde{y}_{\mathrm{A}}}{\partial r^2}+w_{\mathrm{V}}\frac{\partial\widetilde{y}_{\mathrm{A}}}{\partial z}=0. \tag{2.17}$$

Here, r is the radial coordinate. The effective diffusion coefficient in the liquid phase D_{L} is corrected for a porous medium. D_{L} is assumed to be constant. Both component balances are coupled through the equality between diffusive transport in the liquid and vapor phase. The interface mole fraction in the vapor phase is described as a linear function of the interface mole fraction in the liquid phase. The partial differential equations can be solved for concentration profiles in the direction of the flow and orthogonal to the flow direction. An exemplary calculation of concentration profiles is undertaken for an ethanol-isopropyl-water mixture.

Common assumptions of the models of Ramirez-Gonzalez *et al.* [53] and Tschernjaew *et al.* [80] are that the liquid flow in the capillary structures is induced by a constant prescribed gradient of surface tension between the condenser and evaporator and that the contact angle of the fluid is independent of the position in the column.

Rieks *et al.* [56, 57] coupled heat transfer, mass transfer, and impulse transport for zero-gravity distillation at infinite reflux in metal foams. Impulse transport is described utilizing the approach of hydrodynamic analogy. In this approach, the vapor flow is described as a laminar steady-state flow and the liquid flow through the porous medium is described using Darcy's law. The resulting velocity fields are coupled with energy balances and the convection-diffusion equations and solved for the temperature field and the composition field. A temperature distribution in the walls is given as boundary condition.

Heat conduction in the wall is not included. As a consequence of the hydrodynamic analogy approach, diffusion is the only transport mechanism perpendicular to the main flow direction. The model was only used for highly porous metal foams with porosities above 99 % due to the high computational effort for lower porosities. The heights equivalent to a theoretical plate were around 70 mm.

Chapter 3

Aims of this Work

With their investigation of zero-gravity distillation, Seok and Hwang [68] proved that high separation efficiencies can be reached with a distillation concept similar to a heat pipe. Nevertheless, the understanding of the underlying transport processes has not evolved in a detailed manner thus far. In zero-gravity distillation columns, heat transfer, mass transfer, and hydrodynamics are coupled. For heat pipes, the coupling of heat transfer and hydrodynamics is well understood. The capillary structure is a key element in heat pipes, which influences the axial fluid transport and the axial and radial heat transfer. Often, axial channels are chosen as capillary structures. In zero-gravity distillation columns, different components are transported in the two phases and get separated. This makes the system more complex. Based on the state of the art the following can be concluded:

1. Measurements of the relevant variables in zero-gravity distillation lack a high spatial resolution. Until now, experimental works focused on measuring the global separation efficiency of the devices and the composition profiles. The coupling of the different transport processes was not studied experimentally and, as a result, could not be fully understood. In particular, the influence of the hydrodynamics remains unclear.

2. Most models only use simplified mass transfer approaches to describe the separation of components in the system. Only recently was a model in which heat transfer, mass transfer, and hydrodynamics are coupled proposed for the first time. In this model, the hydrodynamics are only resolved in a simplified manner. All the existent models focus on porous media as capillary structures. For channel-shaped capillary structures, no models exist.

3. Neither in experiments nor in models were different influential parameters pointedly varied within a broad range. Thus, it is not known, which parameters influence the separation efficiency to what extent.

4. Due to the lack of understanding of the transport processes, design guidelines for zero-gravity distillation apparatuses do not exist yet. This holds true for the overall system dimensions and process parameters. Additionally, it is unclear how the capillary structure should be designed, which can have a relevant impact on the process, as suggested by heat pipe research.

From these conclusions the aims of this work are deducted.

In this work, an experimental setup is developed to investigate the relevant parameters in zero-gravity distillation with a high spatial resolution and with the possibility to exchange the capillary structure. The relevant variables are the temperature, the interface curvature, and the fluid composition. Secondly, a model is developed which couples hydrodynamics, heat transfer, and mass transfer in zero-gravity distillation columns with channel-shaped capillary structures. Both these methods serve to clarify the following questions:

1. Which process parameters influence the transport processes and thereby the separation efficiency in zero-gravity distillation columns?

2. To what extent is the process influenced by these parameters and how sensitive are the measured variables?

3. How does the capillary structure influence the transport processes and thereby the separation efficiency in zero-gravity distillation columns?

In Chapter 4 the experimental method is explained followed by the presentation of the experimental results in Chapter 5. Chapter 6 is dedicated to the model description. In Chapter 7, the results obtained with the model are shown and discussed. The thesis is concluded with a summary and an outlook in Chapter 8.

Chapter 4

Experimental Method

In this chapter the experimental method is explained. This includes the description of the experimental setup, measurement techniques, measurement procedure, and data evaluation.

The detailed description of the coupled transport processes in zero-gravity distillation demands a characterization of the liquid-vapor interface shape, measurements of wall and vapor temperatures, and an analysis of the fluid composition. In practice, zero-gravity distillation columns will mostly be used with a continuous feed and a continuous withdrawal of product streams. To reduce the complexity of the setup design and of evaluating the transport processes, zero-gravity distillation is only investigated at infinite reflux in this work. After the system is filled, no streams are added or withdrawn from the system. Instead, the concept of the experimental setup is similar to a flat heat pipe that uses a binary mixture as a fluid.

The concept is shown schematically in Figure 4.1. To analyze the separation of the mixture, a fluid withdrawal is implemented at the condenser. Here, the top product composition can be determined after the system has reached a steady state. To withdraw sufficient amounts of liquid for a composition analysis, a small reservoir at the condenser is necessary. Heat is not withdrawn directly from the capillary structure but from the back wall of the system. From this back wall, the liquid flows gravitationally driven into the reservoir.

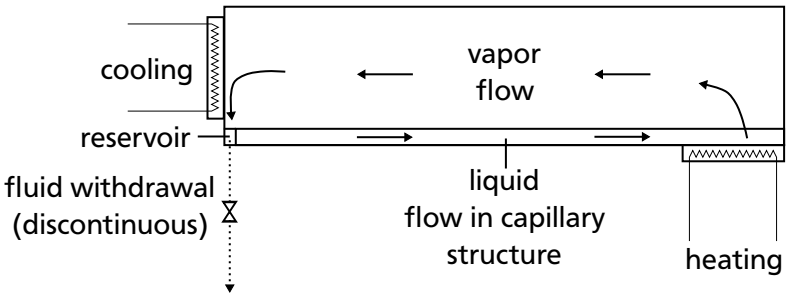

Figure 4.1: Experimental concept for the investigation of zero-gravity distillation at infinite reflux

4.1 Experimental Setup

In Figure 4.2, a top view photograph of the test cell and the setup periphery is shown. In the center of the picture, the test cell is located. Through the glass windows of the test cell, the capillary structure can be

seen. In Figure 4.3 a schematic further illustrates the components of the system. Again, the test cell can be seen in the center of the schematic.

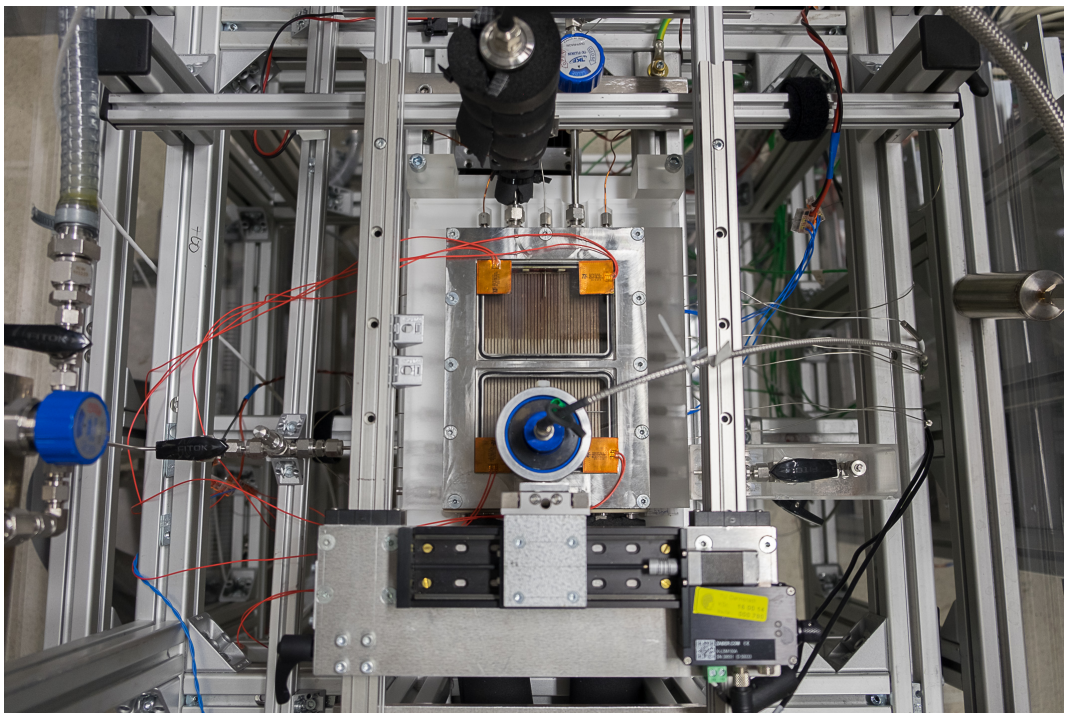

Figure 4.2: Picture of the experimental setup

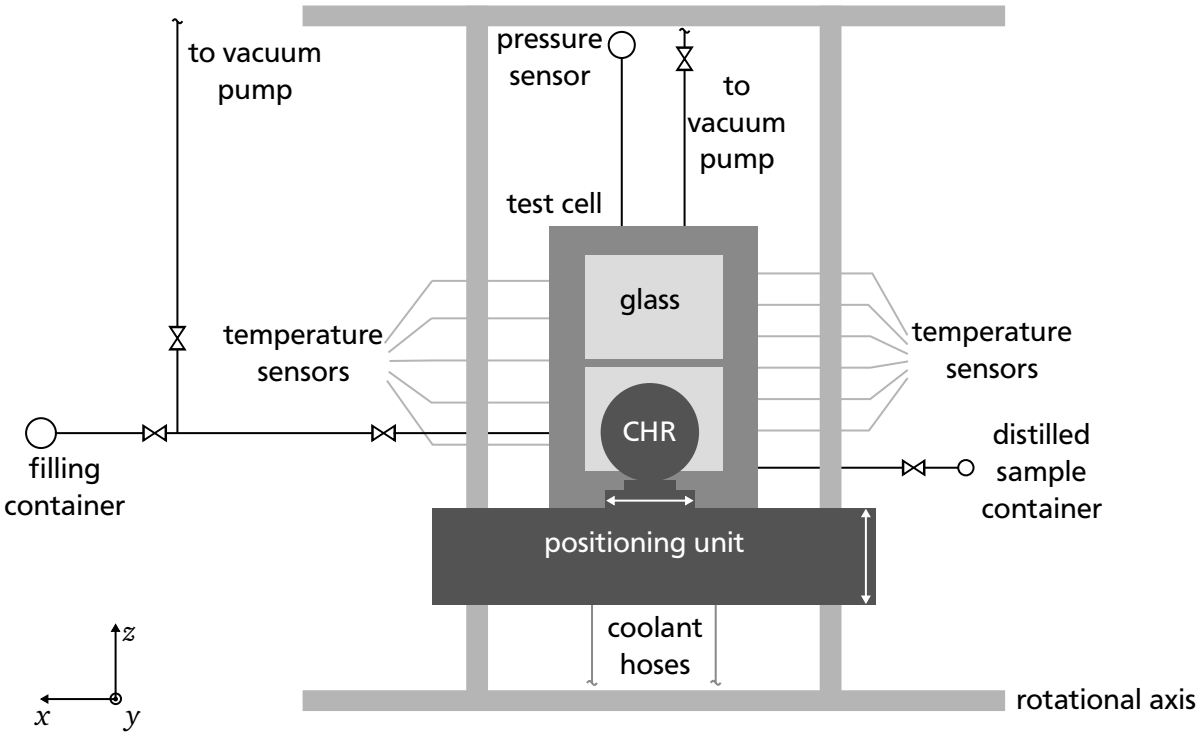

Figure 4.3: Schematic of the experimental setup

From the sides and the top, the test cell is thermally insulated with poly methyl methacrylate. From the bottom, the test cell is thermally insulated with polyoxymethylene and polystyrene. For simplicity, this insulation is not depicted in the schematic. In the photograph, the insulation on the top is taken off to

make the capillary structure visible. Additionally, the test cell is placed in a temperature controlled box to further reduce influences of the laboratory environment. The test cell lid has glass windows at the top through which the process can be observed. Through these glass windows, the position of the liquid-vapor interface shape is detected with a chromatic confocal sensor (CHR). It is electrically adjustable with a positioning unit parallel to the x-axis of the system, which is perpendicular to the main flow direction of the fluid. The sensor can be moved in z-direction with manual slides on aluminum rods. The test cell can be rotated around the rotational axis to change the influence of gravity on the process. The test cell is filled gravitationally driven from the filling container. A sample of the distilled fluid from the condenser reservoir can be withdrawn into an evacuated external container. The test cell and the periphery pipes can be evacuated by a vacuum pump through vacuum hoses. The process cooling at the condenser is executed with a bath thermostat. A coolant circulates through the back side of the main body of the test cell, which is shown at the bottom of the schematic. The evaporator is heated through electric heating foils, which are glued to the bottom of the copper plate lying in the test cell in which the capillary structure is milled. The static vapor pressure at the evaporator is measured with a pressure sensor. Thirteen temperature sensors are located in the copper plate and in the vapor phase.

4.1.1 Test Cell

In Figure 4.4 a section view of the test cell of the experimental setup is shown. The main body is milled of stainless steel. The test cell is 148.5 mm wide (x-direction), 208 mm long (z-direction) and 33.8 mm high (y-direction). Inside the test cell, a thermal insulation made of polyether ether ketone (PEEK) is located. The capillary structure milled into a copper plate is placed on top of this insulation. The copper plate with the capillary structure in the system is exchangeable. It is 153 mm long and 101.6 mm wide. The reservoir at the condenser wall is 3 mm long and 3 mm deep. The heat at the evaporator is supplied directly to the copper plate through heating foils above the insulation. The heating foils are 50.8 mm long in z-direction. Due to the high thermal conductivity of copper compared to PEEK it can be assumed that a negligible part of the supplied heat is conducted through the insulation. To the left of the section view, a lid made of PEEK is screwed onto the main body. Inside this lid, the coolant circulates and heat from the condenser section is withdrawn. The copper plate has a greater height at the evaporator than in the adiabatic zone. The thicker sections in the adiabatic zone between evaporator and condenser are the sections where the temperature sensors are located. Onto the top of the main test cell body a lid is screwed. The lid is sealed with an o-ring. In the lid two borosilicate glasses with a thickness of 5 mm are located. These are also sealed with o-rings. The height of the vapor area above the capillary structure is 15.2 mm from the top of the capillary structures to the bottom side of the windows. This height is determined by the measuring distance of the chromatic confocal sensor. All other connectors for temperature sensors or fluid connections are welded into the main body. The temperature sensors are clamped with polytetrafluorethylene tapers.

The temperature sensors are plugged into the copper plate inside the test cell alternately from both sides. Ten temperature sensors are located in the copper plate; three are located in the vapor phase. In Figure 4.5 the positions of the temperature sensors in the copper plate and in the vapor channel are illustrated. Five temperature sensors are plugged into the copper plate from the left side and another five sensors are plugged into the copper plate from the right side. All temperature sensors are plugged into

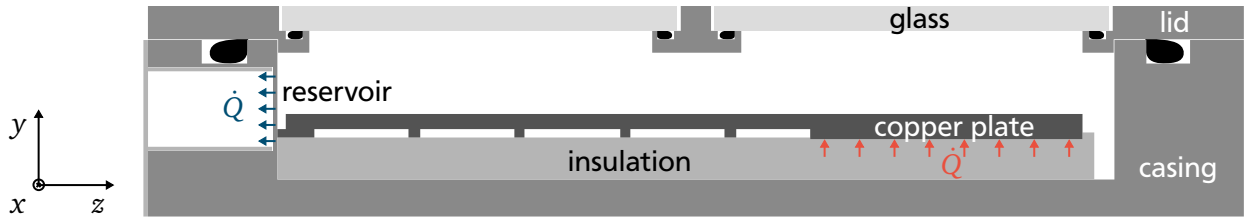

Figure 4.4: Schematic section view of the test cell of the experimental setup

the copper plate 20 mm deep. The three temperature sensors in the vapor phase are located at different axial positions z at the center of the plate in x-direction.

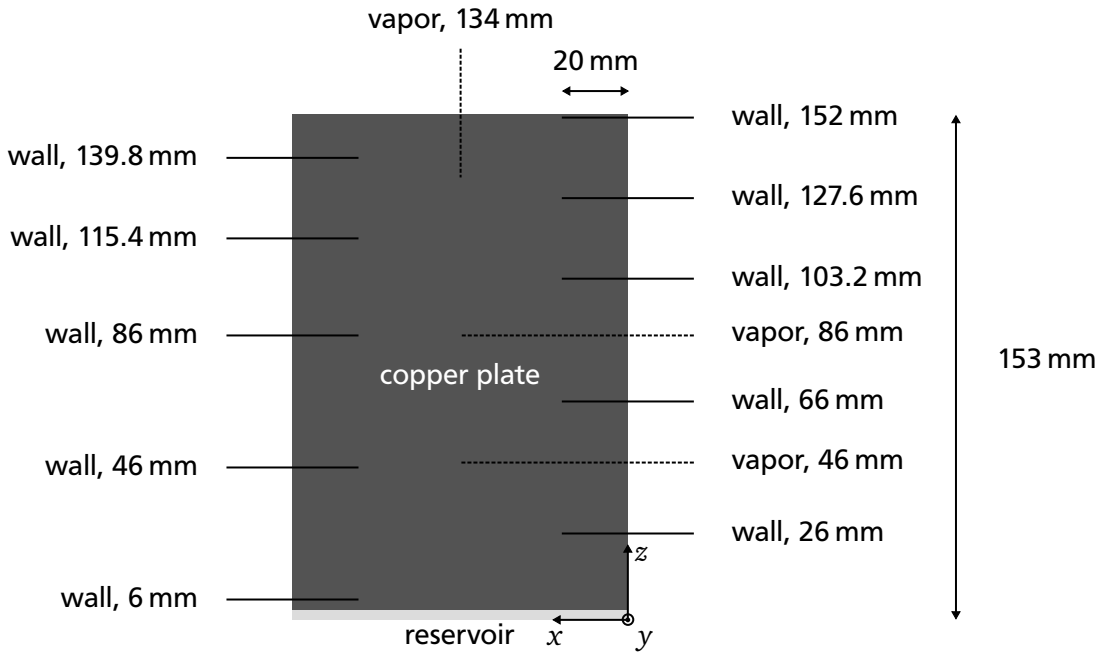

Figure 4.5: Positions of the temperature sensors in the system

To keep the influence of non-condensable gases to a minimum, the leakage rate should be as small as possible. The leakage rate of the test cell was determined with the rising-pressure method and constantly retested over the test runs. In this method, the system is evacuated and the rise in pressure over time at a controlled temperature is evaluated. First, residue of fluid desorbs from the test cell walls and leads to a non-constant gradient in pressure. Once an equilibrium is reached, leaks will result in a constant rise in pressure over time and the actual leakage rate can be determined [85]. With this method the leakage rate was measured at $1.5 \cdot 10^{-5}\,\mathrm{mbar\,l\,s^{-1}}$.

4.1.2 Capillary Structures

Within the scope of this work, two different capillary structures are investigated. In Figure 4.6 these capillary structures are shown. Both capillary structures consist of axial grooves with different cross sections. For one capillary structure these grooves have a triangular cross section. The parallel grooves are milled without gaps to the adjacent grooves. This capillary structure is referred to as triangular groove

structure in the following sections. The grooves of this capillary structure have an opening angle of $\alpha = 60°$ and an opening width of $W_1 = 2\,\text{mm}$ (see Figure 4.6). The second capillary structure has grooves with a rectangular cross section. Only in the evaporator section these grooves have additional micro grooves between the main axial grooves. The main axial grooves have a width of $W_1 = 1\,\text{mm}$ and a height of $h_1 = 1.7\,\text{mm}$. The micro grooves have a width and height of $W_2 = h_2 = 0.5\,\text{mm}$. The distance between the adjacent walls of the main grooves is $W_3 = 1.5\,\text{mm}$. This capillary structure is referred to as advanced rectangular groove structure in the following sections. The dimensions of the capillary structures are also shown in Table 4.1.

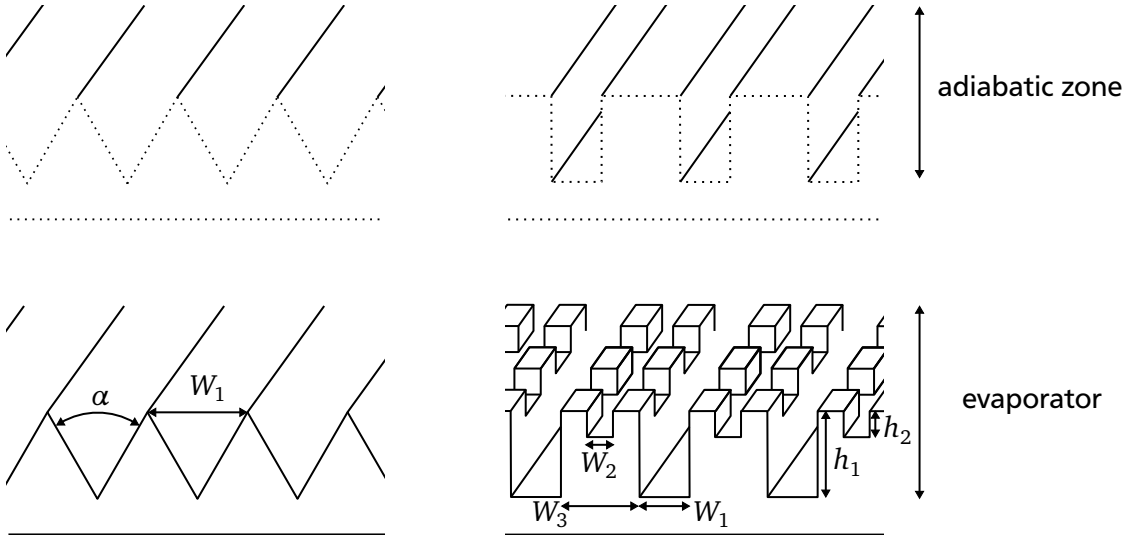

(a) Triangular groove structure

(b) Advanced rectangular groove structure

Figure 4.6: Experimentally investigated capillary structures

Table 4.1: Parameters of experimentally investigated capillary structures

Capillary structure	α in °	W_1 in mm	W_2 in mm	W_3 in mm	h_1 in mm	h_2 in mm
triangular groove structure	60	2	-	-	-	-
advanced rectangular groove structure	-	1	0.5	1.5	1.7	0.5

These capillary structures are chosen for different reasons. The triangular groove structure is chosen with a comparatively high opening width because of the good observability of the liquid-vapor interface shape. Since the groove walls are tilted towards the chromatic confocal sensor, the angle of the interface towards the horizontal axis will be smaller than for rectangular grooves for the same contact angle. This decreases the measuring error of the measurement technique used (see Section 4.2.1). For the advanced rectangular groove structure the focus is not on evaluating the liquid-vapor interface shape. One focus of optimizing capillary structures in heat pipes is generating a higher contact line length and thereby to enhance evaporation in the evaporator. To evaluate the influence of this optimization on zero-gravity distillation, this approach is chosen for the advanced rectangular groove structure. Here, the contact line

length in the evaporator is increased through micro grooves between the main grooves. The contact line length in the evaporator is higher than for the triangular groove structure.

The capillary structures are milled in a copper plate. If copper is in contact with oxygen, an oxidation process can occur over time. Hong *et al.* [29] observed a reduction of the contact angle for oxidized copper surfaces compared to polished copper surfaces. This change in wetting properties can affect the transport processes. To avoid this change in wetting properties over time, a pre-oxidization of the capillary structures is performed. Consequently, the aging process of the copper for the time of the experiments is suppressed. The pre-oxidization is performed according to the procedure suggested by Crößmann [14]. The capillary structure is first cleaned in an ultrasonic bath with acetone. Afterwards the capillary structure is put in an oven at a temperature of 300 °C for 35 minutes. Afterwards the capillary structure is cooled down and then cleaned in an ultrasonic bath for two minutes. The capillary structure is then built into the test cell. To further reduce the probability of an ongoing oxidation of the capillary structure, the test cell is evacuated after every test run and kept at sub-atmospheric pressure; thereby the amount of oxygen in the test cell is reduced compared to an atmospheric pressure.

4.1.3 Fluids

The fluids used in the experiments are water-ethanol mixtures of different compositions. In Figure 4.7, the vapor-liquid equilibrium for water and ethanol is shown at a pressure of 1013 mbar. It can be seen that water and ethanol form an azeotropic mixture at low water mole fractions. The exact position of this azeotropic point depends on the pressure. To the right of the azeotropic point, water is the less volatile component in this fluid system. It is observed that the slope of the vapor saturation temperature and of the liquid saturation temperature depends strongly on the molar composition of the mixture.

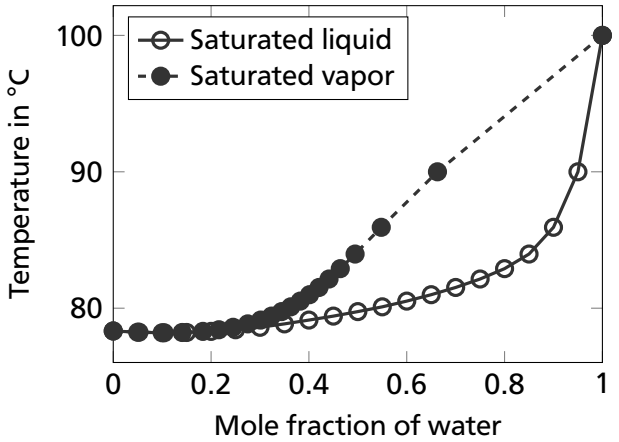

Figure 4.7: Experimentally determined vapor-liquid equilibrium of water-ethanol mixtures at a pressure of 1013 mbar from [22]

In Table 4.2 the surface tension σ, the liquid density ρ_L, and the enthalpy of evaporation Δh_{LV} are given for pure water and ethanol. The surface tension of water is more than three times as high as the surface tension of ethanol. The density of liquid water is almost 30 % higher than the density of liquid ethanol and the enthalpy of evaporation of water is almost 2.7 times as high as the enthalpy of evaporation of ethanol.

Table 4.2: Fluid properties of water and ethanol at a temperature of 50 °C [82]

Fluid	σ in N m^{-1}	ρ_L in kg m^{-3}	Δh_{LV} in kJ kg^{-1}
water	0.068	988.05	2381.96
ethanol	0.020	763.09	892.3

Degassing

Gases are soluble in liquids within certain limits. According to Henry's law, the partial pressure of a dissolved fluid is linearly dependent on the mole fraction of the component in the liquid phase for a constant temperature [73]. Thus, oxygen and nitrogen dissolve in fluids in contact with air. Only when fluids are kept in a pure vapor atmosphere, a negligible amount of non-condensable gases will be dissolved in the liquid phase. Crößmann [14] investigated the influence of non-condensable gases on evaporation from structured surfaces and concluded that an increasing partial pressure of non-condensable gases led to a decreasing heat transfer coefficient. The solubilities of oxygen and nitrogen are different in water and ethanol. Additionally, the solubility in mixtures of these is not linearly dependent on the composition. For measurements with non-condensable gases, this can lead to a poor comparability of experiments with different fluids. To ensure a good comparability of the experimental results, a pure vapor atmosphere is sought during the experiments. This makes degassing of the fluids necessary.

Shchukarev and Tolmacheva [70] investigated the solubility of oxygen in water and ethanol and mixtures of these for temperatures between 4 °C and 50 °C at atmospheric pressure. According to the authors, the solubility of oxygen in ethanol is 5 to 7.5 times higher than the solubility in water. The solubility of oxygen of the mixtures always lay below the weighted added value of the components' solubilities and mostly even below the solubility of only the corresponding ethanol fraction. Whereas the solubility in ethanol was not temperature dependent between 4 °C and 25 °C, the solubility decreased with rising temperature for water. Tokunaga [79] studied the solubilities of oxygen and nitrogen at different temperatures at atmospheric pressure in different alcoholic water mixtures. The data concerning the temperature dependency agrees well with the data gathered by Shchukarev and Tolmacheva [70]. The solubility of nitrogen in pure water was around 50 % of the solubility of oxygen in pure water and around 60 % of the solubility of oxygen in pure ethanol.

Degassing of fluids can be conducted with different methods. Vencel *et al.* [81] compared ultrasound degassing, nitrogen bubbling, and freeze pump thaw degassing regarding their efficiency in oxygen exclusion from organic solvents. The most effective method was found to be freeze pump thaw degassing. In this method, the liquid is frozen, then the vapor phase is withdrawn from the container with a vacuum pump. When the liquid thaws, non-condensable gases will move into the vapor phase. This process can be repeated multiple times in order to achieve a high reduction of the amount of non-condensable gases. While this process is very effective, it is also time consuming. Nitrogen bubbling mainly leads to a reduction of oxygen concentration in the liquid, whereas nitrogen remains dissolved. Degassing fluids in an ultrasonic bath is simple, but also led to the worst reduction of oxygen content in the tests of Vencel *et al.* [81].

The degassing method in this work needs to ensure a sufficient removal of non-condensable gases for all mixtures of water and ethanol. If a mixture is degassed, the composition can change due to the preferred evaporation of the more volatile component. Mixtures of water and ethanol with different compositions are investigated in this work and the test cell is refilled with new fluid prior to every experiment. Thus, a time consuming method is not feasible. Therefore, a repeated vacuum degassing method has been chosen. Following Henry's law, a reduction in pressure will also reduce the amount of dissolved gases in the liquids. Through repeated reduction of the pressure, the amount of non-condensable gases is reduced in this method. The degassing method is schematically illustrated in Figure 4.8.

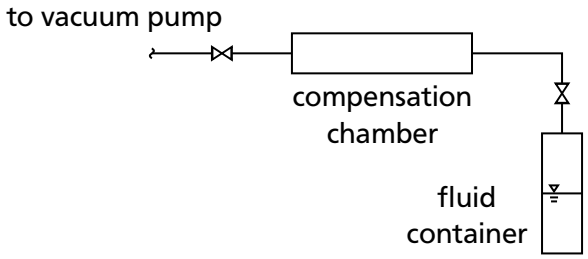

Figure 4.8: Schematic of the degassing procedure

The fluid container with non-degassed liquid under atmospheric pressure is attached to piping connected to a vacuum pump. Between the vacuum pump and fluid container, a hose with significantly higher volume than the fluid container serves as a compensation chamber. This chamber is evacuated at first while the valve to the fluid container is closed. Then the vacuum pump is switched off, the valve to the vacuum pump is closed and afterwards the valve to the fluid container is opened for 20 seconds. Air and vapor will then leave the fluid container towards the compensation chamber. Through the expansion of the gas phase the pressure in the vapor phase above the liquid is reduced. Thus, the solubility of non-condensable gases in the liquid phase is reduced and non-condensable gases leave the liquid phase. At the same time, the liquid partly evaporates. The valve to the fluid container is then closed again. A pause of 90 seconds follows. During this time, the compensation chamber is evacuated again. The process is repeated multiple times.

The efficiency of the process was tested with ethanol since this fluid has the highest solubility of non-condensable gases in this work. The test cell was filled with a fixed amount of liquid and the resulting pressure in the test cell at a controlled temperature of 28 °C was evaluated. The efficiency of the degassing procedure was then determined through a comparison between the saturation pressure of ethanol p_{sat} and the measured pressure in the test cell p. The number of repetitions of the above described process was varied with two and five degassing cycles. Additionally, the comparison was made without degassing the fluid. The results of the comparison of the vapor pressures are shown in Table 4.3.

The expected rise in pressure calculated with the leakage rate of the system was well below 1 mbar in the time frame of all measurements. It can be observed that the measured pressure in the system lies closer to the expected pressure from the saturation curve with an increasing number of repetitions. When the fluid was not degassed at all this resulted in a pressure in the system 8.3 mbar higher than the saturation pressure. For two degassing cycles the pressure lay 1.2 mbar above the expected saturation pressure. For five degassing cycles this difference was at 0.3 mbar. Since the gas solubility of water is

Table 4.3: Degassing efficiency for different executions of degassing cycles for ethanol; saturation pressures are taken from [44].

Degassing cycles	$p - p_{sat}$ in mbar
none	8.3
2	1.2
5	0.3

lower than the solubility of ethanol it was expected that five degassing cycles would be sufficient for water, as well. This was validated performing the same test for water. It could be seen that the pressure difference between the measured pressure and the expected saturation pressure for water was at less than 0.1 mbar.

Based on the presented results, five degassing cycles were chosen for all experiments. The compositions of the mixtures change through the degassing procedure. Due to the standardization of the degassing process, this change in composition is similar for each tested fluid composition over different test runs. To ensure the comparable composition of the fluids used in the experiments, the composition of the fluid is measured prior to every experiment (see Section 4.2.2).

4.2 Measurement Techniques and Data Acquisition

The measured variables in the experimental setup are the temperature, the pressure, the heat flow, the fluid composition and the position of the liquid-vapor interface. All pieces of data except the fluid composition are acquired with the software National Instruments LabVIEW. This software is also used to control the process. For the temperature measurements, thermocouples of type K and platinum resistance thermometers (Pt100) are used. The thermocouples are recorded with a National Instruments cRIO controller. The platinum resistance thermometers are connected to and recorded with bath thermostats. All temperature sensors inside the test cell were calibrated along the entire measurement section with a reference platinum resistance thermometer. The uncertainty along the entire measurement section is at ±185 mK.

The pressure in the vapor phase inside the system is measured with a pressure sensor which was calibrated by the manufacturer the uncertainty of which is at 0.05 % of the full scale, which is equivalent to 0.5 mbar [83]. The pressure is also read by the cRIO controller. The resistive heating foils are connected to a power supply unit. To control the heat flow, the current supplied by the power supply unit is set with an accuracy lower than 0.2 % [18]. The heat flow is calculated through the multiplication of the electric resistance of the heating foils with the current squared. The electric resistance of the heating foils is temperature dependent, which is taken into account for the calculation of the heat flow. In Appendix A, the experimental equipment is listed in a detailed manner.

A parameter of the experiments is the inclination angle. The copper plate is leveled with a spirit level which is placed directly on the capillary structure. The error limit of the spirit level used is at ±0.5° [28]. This error limit is a limit which the manufacturer must maintain in any case, which is why the uncertainty of the inclination angle will be significantly lower [45]. The absolute values of the inclination angles set in this work are of the same order of magnitude as the error tolerance of the spirit level.

In the following sections, the measurement of the liquid-vapor interface shape and the composition analysis are described.

4.2.1 Liquid-Vapor Interface Shape

Confocal-chromatic spectroscopy (CHR) is used to detect the liquid-vapor interface shape. As described in Section 2.3.2, this measurement technique was already used to detect the curvature change along the main flow axis in heat pipes filled with one-component fluids by the research group of Lefèvre.

The measurement principle of the CHR is shown in Figure 4.9. The following description of the measurement principle is based on [37]. CHR can be used to measure distances to objects or thicknesses of transparent objects. Through the chromatic aberration of an optical probe, white light is refracted in distinguishable angles for different wavelengths. If a surface is detected within the measurement range, a particular wavelength of the light will be reflected. The spectrometer of the CHR sensor exhibits a distinct peak at this wavelength. This wavelength can be associated with the distance from the sensor to the object. If the detected surface is transparent and a second surface is within the measurement range, a second peak can be observed in the spectrum. These two measured distances can be used to calculate the distance between these two surfaces. For this calculation, the refractive index of the transparent object between the two surfaces has to be known.

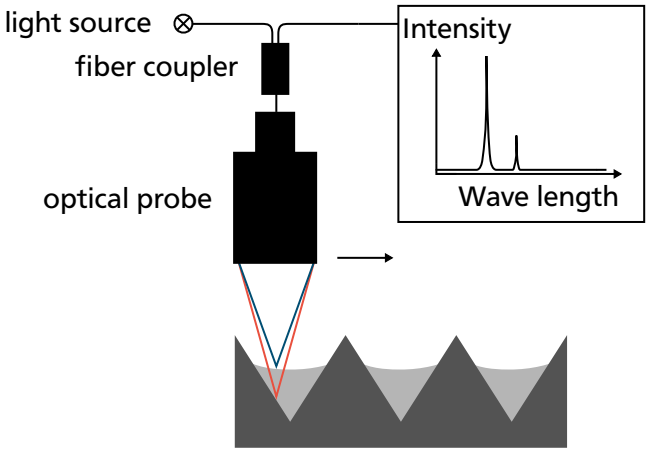

Figure 4.9: Measurement principle of the CHR sensor (adapted from [37]); in this illustration the sensor detects the liquid-vapor interface and the wall signal of a triangular groove structure.

The CHR sensor can only measure distances at one distinct point. In order to evaluate the shape of the liquid-vapor interface, the sensor needs to be moved. The sensor can be moved perpendicular to the main flow direction with an electrical positioning unit. While this positioning unit changes the position at a constant velocity, the sensor continuously measures the distance to detect the interface shape. The sensor is moved with a velocity of $0.125\,\mathrm{mm\,s^{-1}}$ over a length of 22 mm, which means it can detect the menisci in eleven grooves for the triangular groove structure. A measuring frequency of 250 Hz is used.

In this experimental setup, the CHR sensor is used to detect the liquid-vapor interface through glass windows. Due to the high reflection of glasses, only a small fraction of the light emitted by the sensor is transmitted through the glass. Additionally, the change in the transmission of gas and glass leads to a deflection of the light beams, which increases the measurement error, especially for curved surfaces like

the liquid-vapor interface. For the glass used in this setup, the magnitude of this error was evaluated. The post-processing procedure to recalculate the liquid-vapor interface shape from the measured signal taking the measurement error into account is described in Section 4.4.1.

4.2.2 Composition Analysis

The fluid composition is quantitatively analyzed with nuclear magnetic resonance (NMR) spectroscopy in this work. The samples analyzed are a sample of the initial fluid with which the test cell is filled and a sample of the liquid at the condenser collected after finishing the experiment. The volume of the samples is approximately 50 µl. The initial fluid is analyzed in order to ensure a specified initial fluid composition with respect to the change in composition through degassing. The liquid at the condenser is analyzed in order to evaluate the separation of the mixture. In NMR spectroscopy, a magnetic field is imposed on a liquid sample. The nuclear magnetic moment is stimulated through the magnetic field. Atoms which exhibit magnetic moments different from zero generate a resonance signal, which can be detected by a spectrometer. An example for these atoms is the H^1 isotope. Different molecules generate distinguishable resonance signal shapes due to the magnetic interaction of the different nuclei. In the resulting spectrum, the peak shapes are characteristic for different molecules. These and further fundamentals on NMR spectroscopy can be found in [24].

To detect spectra of ethanol-water mixtures and evaluate the composition, the H^1 isotope can be used. According to Malz and Jancke [49] the measurement uncertainty of NMR spectroscopy strongly depends on the measuring procedure and data evaluation. For this reason Malz and Jancke [49] developed a measuring and evaluation protocol for NMR measurements of the H^1 isotope. In the scope of their study, various samples were measured with this protocol at different laboratories and the measurement uncertainty of the molar composition was determined to be at 1.5 % with a confidence interval of 95 %. The uncertainty of the NMR measurements in this work is estimated to be at the same value.

4.3 Measurement Procedure

Prior to every test run, fluid is mixed and degassed according to the procedure described in Section 4.1.3. The test cell is preheated and the ambient temperature in the temperature controlled box is set to a fixed value. The test cell is filled with a fixed volume of liquid (13.5 ml for the triangular groove structure and 16.2 ml for the advanced rectangular groove structure). After the test cell is filled, a sample is withdrawn from the pipe below the filling container to determine its composition. The heating and cooling duty are increased stepwise in order to reach a steady state condition in the system. The thermostat cooling the condenser is controlled using an external Pt100 sensor. This sensor is plugged in the copper plate at the position $z = 152\,\text{mm}$ (see Figure 4.5). The bath temperature of the thermostat is controlled in a way that the value of the external sensor at position $z = 152\,\text{mm}$ is at 37 °C. Once a steady state condition is achieved, the CHR sensor is used to subsequently measure the liquid-vapor interface shape at four different axial positions in the system. These are scanned in the same order every time. When the CHR measurements are finished, a sample is withdrawn from the reservoir in order to evaluate the composition at the condenser.

4.4 Data Evaluation

The data gathered is only evaluated in a steady state. The criterion used to define the steady state is that the absolute value of the difference of any wall temperature in a time period of 840 s is less than 0.2 K. The mean values of the temperatures, pressure, and the heat flux are averaged over this time period of 840 s.

4.4.1 Evaluation of Chromatic Confocal Distance Measurements

The CHR measurements are used to calculate the curvature of the liquid-vapor interface. It is assumed that the curvature is constant for each cross section of a meniscus. Under this assumption, the interface shape can be approximated as an arc of a circle. As described in Section 4.2.1, the measurements of the liquid-vapor interface cross-section shape are afflicted with a relevant error. Thus, before a circular fit to the interface can be applied, the interface position needs to be reconstructed. The measurement error of the CHR sensor is dependent on the inclination angle of the measured surface to the horizontal. This error is approximated by a polynomial dependent on the angle to the horizontal of the measured surface. This measurement error needs to be added to the unknown real interface position to obtain the measurement signal. With a least squares method, the deviation of the measured signal from the sum of an estimated interface position and the corresponding measurement error is minimized. Thereby, the interface position is determined. Due to the sign of the measurement error, the interface is always below the non-corrected measured signal. Only inclination angles of the interface up to 14° to the horizontal are taken into account for the calculation of the curvature. With this corrected signal, a circle is fitted and the curvature radius is calculated.

In Figure 4.10, the circle fit to the interface position is illustrated together with the filled groove signal of the CHR sensor and the signal corresponding to the position of the empty groove. The empty groove signal was measured with the CHR sensor in a dry state of the system. This empty groove signal agrees well with the real profile of the manufactured structure. For the filled groove signal, the CHR sensor detects the liquid-vapor interface in the vicinity of the center of the groove. In the upper parts of the groove, the CHR sensor detects the dry groove wall. In the region in between, the algorithm does not detect the liquid-vapor interface. The intensity of the liquid-vapor interface signal is too weak because of the high inclination in these regions. In some cases, a wall signal is detected instead. This detected wall signal is influenced by the liquid because of the change in the refractive index from the vapor to the liquid phase. Compared to the empty groove, the wall is detected closer to the sensor in these regions. Thus, the point at which the filled groove signal starts to deviate from the empty groove signal is the point where the refractive index changes and the wall is wetted. This point can be compared to the intersection point of the circle fit and the empty groove signal. The region around these two points is depicted in the "magnifying glass" in Figure 4.10. This comparison was undertaken for a test run with pure ethanol. Of the tested fluids, pure ethanol has the best wetting properties and thus the interface has a comparatively high curvature. For this reason, the angle error and therefore the deviations of the measured signal from the real interface position are expected to be the highest for pure ethanol. For the tested grooves at the evaporator, the calculated distance between the calculated intersection point and the point at which the refractive index changes was always below 100 μm at the upward inclined groove wall. This shows that

the determined curvature radius fits to the measurements of the wall detected through the liquid. In the results presented in Chapter 5, the error bars of the curvature radii represent the standard deviation of the mean curvature radius over different grooves.

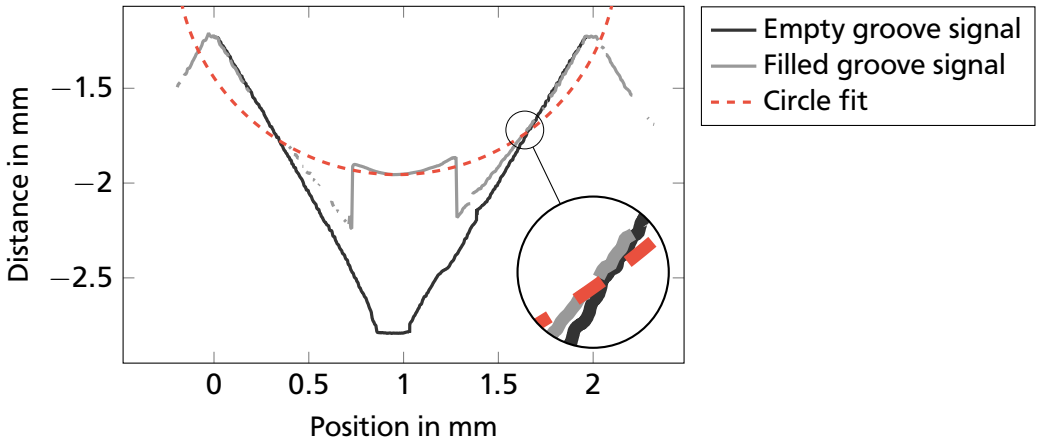

Figure 4.10: Comparison of measured CHR signal with circle fit and measured empty groove signal

4.4.2 Calculation of Interface Composition

The three temperature measurements in the vapor phase at the axial positions $z = 46\,\text{mm}$, $z = 86\,\text{mm}$, and $z = 134\,\text{mm}$ are used to calculate the interface composition along the main flow axis of the system. Under the assumption that the temperature in the vapor phase is constant at every axial position, the interface temperature is equal to the measured vapor temperature. With the measured pressure, the vapor-liquid equilibrium can be used to determine the interface composition from the vapor temperatures. The vapor-liquid equilibrium data is taken from Lemmon *et al.* [44]. The uncertainties of the calculated compositions are depicted in Chapter 5. As a measure for the uncertainty of the temperature measurements, the standard deviation of the temperature measurements over the steady state condition is added to the uncertainty of the temperature sensors along the entire measurement section ($\pm 185\,\text{mK}$).

4.4.3 Calculation of Capillary Pressure

To calculate the distribution of the capillary pressure with Equation 2.10, the surface tensions and the curvature radii need to be determined. From the calculated interface compositions, the surface tensions at the axial positions $z = 46\,\text{mm}$, $z = 86\,\text{mm}$, and $z = 134\,\text{mm}$ can be determined. The curvature radii are measured at different axial positions. Therefore, the surface tensions at the axial positions $z = 46\,\text{mm}$, $z = 86\,\text{mm}$, and $z = 134\,\text{mm}$ are linearly interpolated or extrapolated to the positions where the curvature radii are measured ($z = 30.5\,\text{mm}$, $z = 55.5\,\text{mm}$, $z = 95.5\,\text{mm}$, and $z = 115.5\,\text{mm}$). Table 4.4 gives an overview on how the surface tensions at the positions of the curvature radius measurements are calculated. The capillary pressure at the positions of the curvature radius measurements can then be evaluated. The uncertainty of the calculated capillary pressure is dependent on the uncertainty of the surface tension and on the uncertainty of the measured curvature radii. The uncertainty of the surface tension results from the uncertainty of the vapor temperature measurements. The standard deviation over the different

grooves is taken as uncertainty of the curvature radii. Both uncertainties are propagated in the calculation of the capillary pressure and shown in the diagrams in Chapter 5 as error bars.

Table 4.4: Calculation of surface tensions at different axial positions

Distance of curvature radius measurement from condenser	Calculation of surface tension
$z = 30.5$ mm	linearly extrapolated from calculated surface tensions at $z = 46$ mm and $z = 86$ mm
$z = 55.5$ mm	linearly interpolated from calculated surface tensions at $z = 46$ mm and $z = 86$ mm
$z = 95.5$ mm	linearly interpolated from calculated surface tensions at $z = 86$ mm and $z = 134$ mm
$z = 115.5$ mm	linearly interpolated from calculated surface tensions at $z = 86$ mm and $z = 134$ mm

Chapter 5

Experimental Results

In this chapter, the results of the experiments are presented. Firstly, the results obtained with the triangular groove structure are discussed. Afterwards, the results obtained with the advanced rectangular groove structure are presented. In Table 5.1 the parameters of the experiments are shown. For the triangular groove structure, three heat fluxes at the evaporator, four overall average fluid compositions, and three inclination angles were tested. The experiment with an overall average ethanol mole fraction of $\widetilde{x}_{\mathrm{E,OA}} = 0.55$, a heat flux at the evaporator of $\dot{q}_{\mathrm{ev}} = 4000\,\mathrm{W\,m^{-2}}$, and an inclination angle of $\beta = 0°$ was chosen as reference experiment. In the following diagrams, the results of the reference experiment are always shown in turquoise color. The parameters heat flux, composition, and inclination angle were varied independently from each other. For the varied heat flux and inclination, the measured overall average ethanol mole fractions vary between $\widetilde{x}_{\mathrm{E,OA}} = 0.55$ and $\widetilde{x}_{\mathrm{E,OA}} = 0.56$. The reasons for this are deviations in the mixing and degassing of the supplied liquid and the uncertainty of the NMR measurements (see Section 4.2.2). For the advanced rectangular groove section, three fluid compositions were tested at a heat flux at the evaporator of $\dot{q}_{\mathrm{ev}} = 4000\,\mathrm{W\,m^{-2}}$ and an inclination angle of $\beta = 0°$. All sets of parameters were repeated at least two times and showed a good repeatability.

Table 5.1: Parameters of experiments

Capillary structure	Heat flux at the evaporator $\dot{q}_{\mathrm{ev}}$ in $\mathrm{W\,m^{-2}}$	Overall average mole fraction of ethanol $\widetilde{x}_{\mathrm{E,OA}}$	Inclination angle β in °
triangular groove structure	2000, 4000, 6000	0.38, 0.55, 0.71, 0.9	−0.4, 0, 0.4
advanced rectangular groove structure	4000	0.56, 0.73, 0.9	0

The results of the measurements are mostly presented as functions of the distance from the condenser back wall. The evaporator is at the right end of the diagrams in these cases.

5.1 Triangular Groove Structure

For the triangular groove structure, measurements with different overall average fluid compositions, heat fluxes, and inclination angles are compared to each other.

5.1.1 Influence of the Mixture Composition

In Figure 5.1, the temperatures in the wall of the capillary structure and in the vapor phase are shown over the distance from the condenser for four overall average ethanol mole fractions. The temperature furthest from the condenser is controlled at 37 °C. The temperature closest to the condenser wall decreases with decreasing overall average ethanol mole fraction. Thus, more heat is conducted along the metal plate towards the condenser for decreasing overall average ethanol mole fractions. In general, the wall temperatures increase almost monotonically from the condenser to the evaporator for the overall average ethanol mole fractions $\widetilde{x}_{\mathrm{E,OA}} = 0.71$ and $\widetilde{x}_{\mathrm{E,OA}} = 0.90$. For the overall average ethanol mole fractions $\widetilde{x}_{\mathrm{E,OA}} = 0.38$ and $\widetilde{x}_{\mathrm{E,OA}} = 0.55$, this is not the case, especially not in the evaporator. The temperature sensors are plugged into the metal plate alternately from different sides (compare Figure 4.5). It is likely that the wall temperature is not constant at every axial position for these experiments. Closer to the condenser, this trend is less observable. In the right part of Figure 5.1, the vapor temperatures for the four different experiments can be seen. These are measured at three axial positions in the system. Similarly to the wall temperatures, the vapor temperatures increase towards the evaporator for every experiment. With decreasing overall average ethanol mole fraction, the vapor temperature difference between the temperature measured in the evaporator and the temperature closest to the condenser decreases.

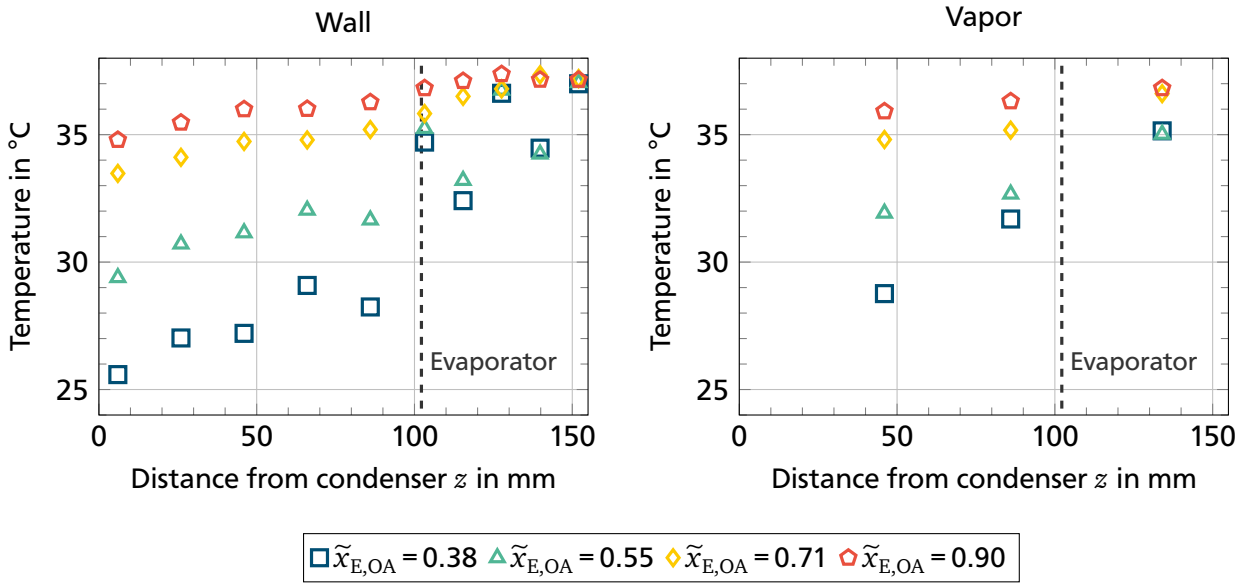

Figure 5.1: Temperatures in the walls of the capillary structure (left) and in the vapor phase (right) over the length of the triangular groove structure for a heat flux of $\dot{q}_{\mathrm{ev}} = 4000\,\mathrm{W\,m^{-2}}$ and an inclination angle of $\beta = 0°$ for four different overall average ethanol mole fractions ($\widetilde{x}_{\mathrm{E,OA}} = 0.38$, $\widetilde{x}_{\mathrm{E,OA}} = 0.55$, $\widetilde{x}_{\mathrm{E,OA}} = 0.71$, and $\widetilde{x}_{\mathrm{E,OA}} = 0.90$)

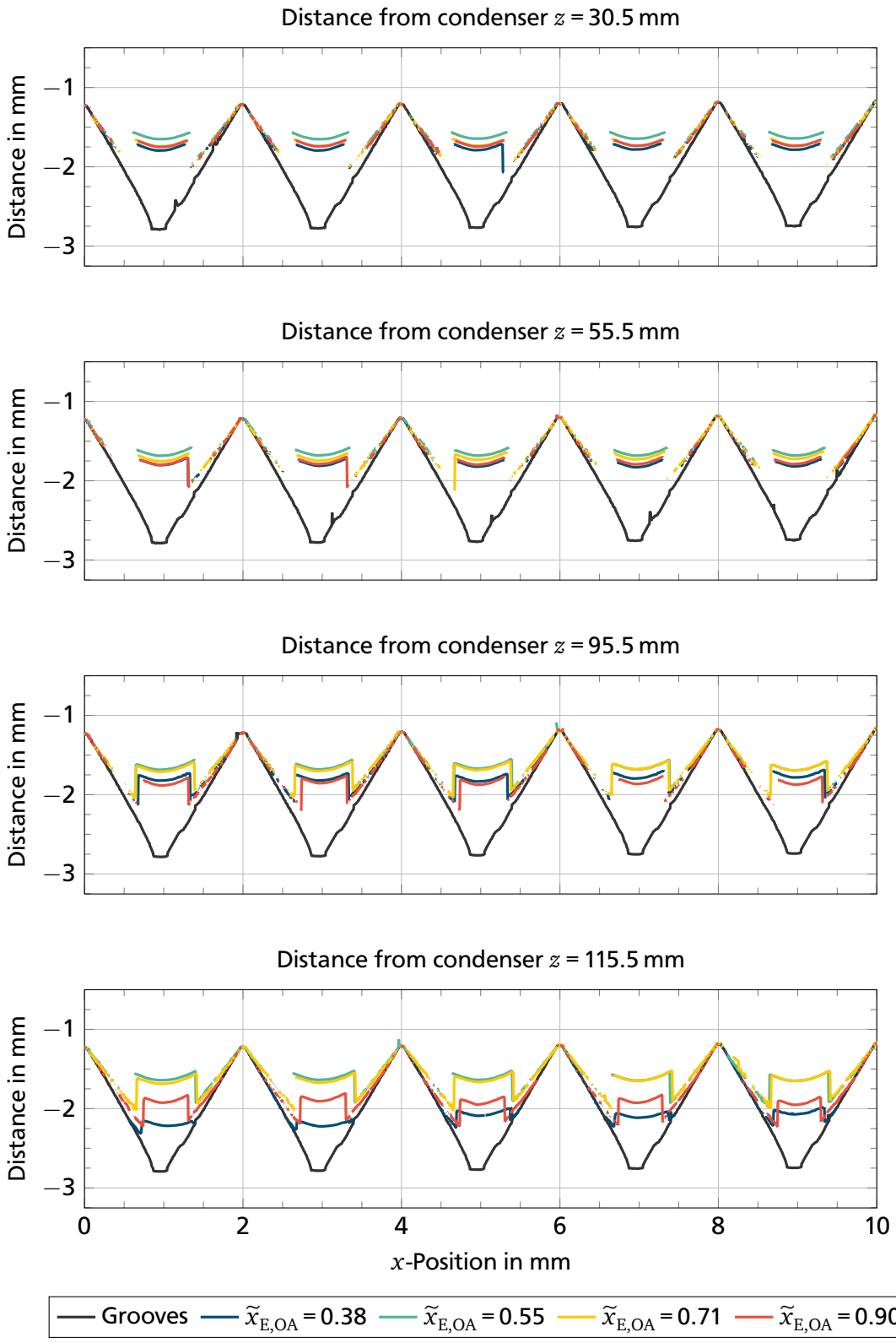

Figure 5.2: Liquid-vapor interface shape at different axial positions (z = 30.5 mm, z = 55.5 mm, z = 95.5 mm, and z = 115.5 mm) in the system for a heat flux of $\dot{q}_{\mathrm{ev}} = 4000\,\mathrm{W\,m^{-2}}$ and an inclination angle of $\beta = 0°$ for four different overall average ethanol mole fractions ($\widetilde{x}_{\mathrm{E,OA}} = 0.38$, $\widetilde{x}_{\mathrm{E,OA}} = 0.55$, $\widetilde{x}_{\mathrm{E,OA}} = 0.71$, and $\widetilde{x}_{\mathrm{E,OA}} = 0.90$)

In Figure 5.2, excerpts of the measurements performed with the CHR sensor for the four experiments are shown. These measurements are not corrected with the error described in Section 4.4.1. Five parallel grooves are shown in the diagrams. At the top, the results for the position closest to the condenser are depicted ($z = 30.5\,\mathrm{mm}$). The distance from the condenser increases towards the bottom of the page. Additionally, measurements of the grooves in a dry state are shown in the diagrams. For the overall average ethanol mole fraction $\widetilde{x}_{\mathrm{E,OA}} = 0.55$, the grooves are filled closest to the top at every position. The menisci in the different grooves at every axial position have a similar shape and groove filling for this experiment. The experiment with the overall average ethanol mole fraction $\widetilde{x}_{\mathrm{E,OA}} = 0.38$ exhibits a strong decrease in groove filling between position $z = 95.5\,\mathrm{mm}$ and position $z = 115.5\,\mathrm{mm}$. At position $z = 115.5\,\mathrm{mm}$ the menisci are less symmetric than at the other three positions and the inclination of the menisci towards the adjacent channel walls varies more strongly. For the overall average ethanol mole fraction $\widetilde{x}_{\mathrm{E,OA}} = 0.71$, the menisci lie closer to the groove bottom than for the overall average ethanol mole fraction $\widetilde{x}_{\mathrm{E,OA}} = 0.55$ at the two positions closer to the condenser. At the two positions further away from the condenser, the groove filling and menisci shapes are similar to the values for the overall average ethanol mole fraction $\widetilde{x}_{\mathrm{E,OA}} = 0.55$. For the highest overall average ethanol mole fraction $\widetilde{x}_{\mathrm{E,OA}} = 0.90$, the menisci lie closer to the groove bottom than for the overall average ethanol mole fraction $\widetilde{x}_{\mathrm{E,OA}} = 0.55$ at every axial position. For this experiment and for the overall average ethanol mole fraction $\widetilde{x}_{\mathrm{E,OA}} = 0.38$ it is most likely that a higher amount of the liquid agglomerates at the condenser than in the other two experiments.

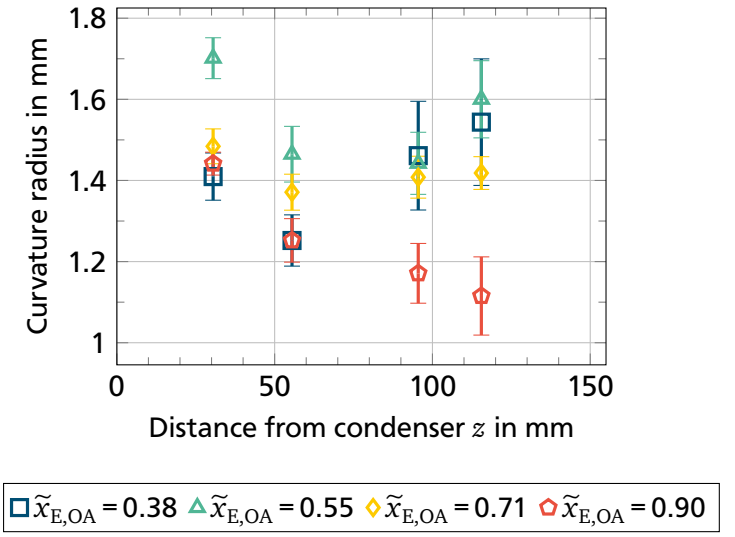

Figure 5.3: Mean curvature radii with standard deviations over the length of the triangular groove structure for a heat flux of $\dot{q}_{\mathrm{ev}} = 4000\,\mathrm{W\,m^{-2}}$ and an inclination angle of $\beta = 0°$ for four different overall average ethanol mole fractions ($\widetilde{x}_{\mathrm{E,OA}} = 0.38$, $\widetilde{x}_{\mathrm{E,OA}} = 0.55$, $\widetilde{x}_{\mathrm{E,OA}} = 0.71$, and $\widetilde{x}_{\mathrm{E,OA}} = 0.90$)

In Figure 5.3, the calculated mean values of the curvature radii in the parallel grooves at the four different distances from the condenser are depicted. Additionally, the standard deviation of the different curvature radii at each axial position is shown. The different experiments do not follow a general trend. For the overall average ethanol mole fraction $\widetilde{x}_{\mathrm{E,OA}} = 0.38$, the mean curvature radius decreases from position $z = 30.5\,\mathrm{mm}$ to $z = 55.5\,\mathrm{mm}$. From this position towards the evaporator the mean curvature radius increases. As it can be observed in Figure 5.2, the groove filling decreases monotonically towards

the evaporator for this overall average fluid composition. The standard deviation of the curvature radii increases monotonically for this experiment from the condenser to the evaporator. Compared to the other experiments, the standard deviation at the evaporator ($z = 115.5\,\mathrm{mm}$) is higher. The standard deviation of the experiment with the overall average ethanol mole fraction $\widetilde{x}_{\mathrm{E,OA}} = 0.55$ is at similar values to the experiment with the overall average ethanol mole fraction $\widetilde{x}_{\mathrm{E,OA}} = 0.38$ at the two positions next to the condenser. At the two positions $z = 95.5\,\mathrm{mm}$ and $z = 115.5\,\mathrm{mm}$, the standard deviation is lower. For this mixture composition, a decrease in the mean curvature radius from the condenser to position $z = 95.5\,\mathrm{mm}$ can be seen. From this position to position $z = 115.5\,\mathrm{mm}$, the curvature radius increases. For the overall average ethanol mole fraction $\widetilde{x}_{\mathrm{E,OA}} = 0.71$, a slight increase in curvature radius from position $z = 55.5\,\mathrm{mm}$ to $z = 115.5\,\mathrm{mm}$ can be observed. The standard deviation of the curvature radii is comparatively low at every axial position for this mixture. When further increasing the overall average ethanol mole fraction to $\widetilde{x}_{\mathrm{E,OA}} = 0.90$, the curvature radii do not increase towards the evaporator. For this overall average ethanol mole fraction, a monotonic decrease in curvature radii can be observed from condenser to evaporator.

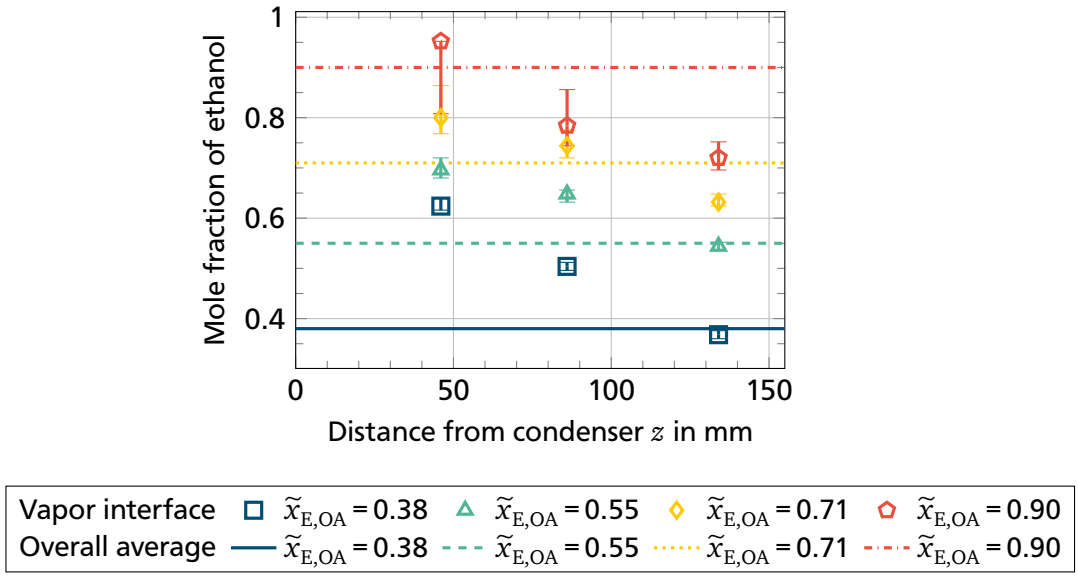

Figure 5.4: Vapor ethanol mole fractions at the interface calculated from vapor temperature measurements compared to overall average ethanol mole fractions over the length of the triangular groove structure for a heat flux of $\dot{q}_{\mathrm{ev}} = 4000\,\mathrm{W\,m^{-2}}$ and an inclination angle of $\beta = 0°$ for four different overall average ethanol mole fractions ($\widetilde{x}_{\mathrm{E,OA}} = 0.38$, $\widetilde{x}_{\mathrm{E,OA}} = 0.55$, $\widetilde{x}_{\mathrm{E,OA}} = 0.71$, and $\widetilde{x}_{\mathrm{E,OA}} = 0.90$)

Based on the evaluation procedure described in Section 4.4.2, the calculated vapor ethanol mole fractions at the interface $\widetilde{y}_{\mathrm{E,int}}$ over the distance from the condenser are presented in Figure 5.4 for the four experiments. Additionally, the overall average ethanol mole fraction is plotted. The compositions calculated from the vapor temperatures all show a decrease in the interface ethanol mole fraction towards the evaporator. No clear trend can be observed, which would indicate stronger changes in the interface composition in different sections of the systems. With increasing the overall average ethanol mole fraction, the ethanol mole fraction at the interface increases at every position. The relative position compared to the overall average ethanol mole fraction varies for the different experiments. The vapor interface ethanol mole fraction is higher than the overall average ethanol mole fraction for the experiments $\widetilde{x}_{\mathrm{E,OA}} = 0.38$ and $\widetilde{x}_{\mathrm{E,OA}} = 0.55$ at the two positions closer to the condenser. In the evaporator, the vapor interface ethanol

mole fraction is at similar values as the overall average ethanol mole fraction for these experiments. For the two highest overall average ethanol mole fractions, the vapor interface ethanol mole fractions at the evaporator are at lower values than the overall average ethanol mole fraction. Closer to the condenser, the difference between the vapor interface ethanol mole fraction and the overall average ethanol mole fraction decreases with increasing the overall average ethanol mole fraction.

In Figure 5.5, the distribution of the capillary pressure in the system is shown, calculated with the method explained in Section 4.4.3. For all experiments, the capillary pressure increases from the condenser to the evaporator. This observation is in accordance with the expectations, since the liquid pressure must decline towards the evaporator. This means that the capillary pressure has to increase towards the evaporator for a horizontal system. At the position closest to the condenser, the capillary pressure decreases with increasing the overall average ethanol mole fraction. Excluding the highest overall average ethanol mole fraction $\widetilde{x}_{\mathrm{E,OA}} = 0.90$, this observation is valid for all the other axial positions, as well.

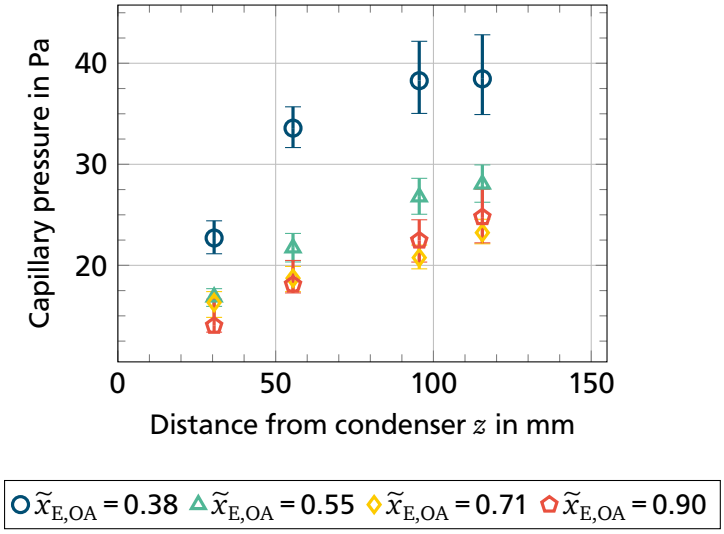

Figure 5.5: Capillary pressure calculated from temperature measurements and CHR measurements over the length of the triangular groove structure for a heat flux of $\dot{q}_{\mathrm{ev}} = 4000\,\mathrm{W\,m^{-2}}$ and an inclination angle of $\beta = 0°$ for four different overall average ethanol mole fractions ($\widetilde{x}_{\mathrm{E,OA}} = 0.38$, $\widetilde{x}_{\mathrm{E,OA}} = 0.55$, $\widetilde{x}_{\mathrm{E,OA}} = 0.71$, and $\widetilde{x}_{\mathrm{E,OA}} = 0.90$)

In Figure 5.6, the difference between the ethanol mole fraction of the distilled sample withdrawn at the condenser $\widetilde{x}_{\mathrm{E,D}}$ and the overall average ethanol mole fraction $\widetilde{x}_{\mathrm{E,OA}}$ is plotted for the different overall average mixture compositions. This difference is formed to evaluate the separation efficiency. The ethanol mole fraction of the condenser sample is higher than the overall average ethanol mole fraction for every experiment. This meets the expectations since ethanol is the more volatile component in the system and should therefore agglomerate at the condenser. The increase in ethanol mole fraction is highest for the overall average ethanol mole fraction $\widetilde{x}_{\mathrm{E,OA}} = 0.38$ at a value of $\widetilde{x}_{\mathrm{E,D}} - \widetilde{x}_{\mathrm{E,OA}} = 0.16$. With increasing the overall average ethanol mole fraction, the difference between the distilled condenser ethanol mole fraction and the overall average ethanol mole fraction decreases monotonically. For an overall average ethanol mole fraction of $\widetilde{x}_{\mathrm{E,OA}} = 0.90$, the increase is only at a value of $\widetilde{x}_{\mathrm{E,D}} - \widetilde{x}_{\mathrm{E,OA}} = 0.03$. This mixture is close to the azeotropic point of the vapor-liquid equilibrium.

In Table 5.2, the measured pressures in the system in a steady-state condition are shown. Since the temperature furthest from the condenser is controlled at a fixed value, the resulting pressures vary for the

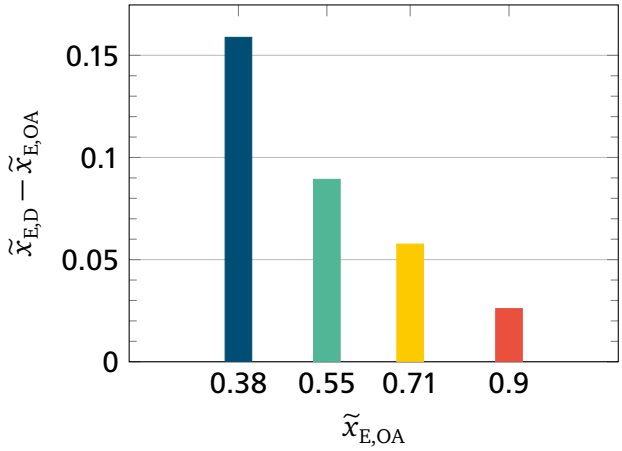

Figure 5.6: Difference between distilled condenser ethanol mole fraction and overall average ethanol mole fraction for the triangular groove structure for a heat flux of $\dot{q}_{\mathrm{ev}} = 4000\,\mathrm{W\,m^{-2}}$ and an inclination angle of $\beta = 0°$ for four different overall average ethanol mole fractions ($\widetilde{x}_{\mathrm{E,OA}} = 0.38$, $\widetilde{x}_{\mathrm{E,OA}} = 0.55$, $\widetilde{x}_{\mathrm{E,OA}} = 0.71$, and $\widetilde{x}_{\mathrm{E,OA}} = 0.90$)

different experiments. When increasing the overall average ethanol mole fraction, the pressure in the system measured at the evaporator increases. The reason for this is the higher vapor pressure of ethanol compared to water.

Table 5.2: Pressures of the experiments with varied fluid composition for the triangular groove structure

	$\widetilde{x}_{\mathrm{E,OA}} = 0.38$	$\widetilde{x}_{\mathrm{E,OA}} = 0.55$	$\widetilde{x}_{\mathrm{E,OA}} = 0.71$	$\widetilde{x}_{\mathrm{E,OA}} = 0.90$
p in mbar	85.5	109.0	134.0	144.6

Discussion of the Influence of the Mixture Composition

For the varied fluid composition, the magnitude of the axially conducted heat flows differs. For higher ethanol fractions, the axially conducted heat flow decreases, which can be seen from the wall temperatures in Figure 5.1. The vapor-liquid equilibrium (Figure 4.7) shows that for higher ethanol fractions, the absolute value of the slope of the saturation lines is considerably lower than for low ethanol fractions. Thus, the mixture behavior is closer to pure fluids towards higher ethanol fractions. At the evaporator, the vapor interface ethanol fraction is lower than the overall average ethanol fraction in the system, especially for higher overall average ethanol fractions (see Figure 5.4). Taking the vapor-liquid equilibrium into account, the liquid interface ethanol fraction will be even lower than the vapor interface ethanol fraction. Due to the negligible mass of the vapor phase compared to the overall mass, this means that the mean axial liquid ethanol fraction is most likely higher than the vapor interface ethanol fraction. For low overall average ethanol fractions, this trend is inverted. Here, the vapor interface ethanol fraction is mostly higher than the overall average ethanol mole fraction. Thus, the sign of the composition gradients in the liquid phase changes depending on the fluid composition. The change in surface tension along the main flow axis influences the curvature radii (see Figure 5.3). The general trend of the capillary pressure meets the expectations of an increasing capillary pressure towards the evaporator, although the high increase in capillary pressure from position $z = 30.5\,\mathrm{mm}$ to position $z = 55.5\,\mathrm{mm}$ for the lowest overall average

ethanol mole fraction is unexpected. Based on the temperature distribution in the walls of the capillary structure, the flow rates are most likely the smallest in this case.

5.1.2 Influence of the Heat Flux

In this section, the influence of the heat flux supplied to the system at the evaporator is evaluated. Three heat fluxes are compared for a mixture with the overall average ethanol mole fraction $\widetilde{x}_{\mathrm{E,OA}} = 0.55$ to $\widetilde{x}_{\mathrm{E,OA}} = 0.56$. In Figure 5.7, the temperature distributions in the walls of the capillary structure and in the vapor phase are shown for the three experiments. The temperature furthest from the condenser is controlled at 37 °C. With increasing the heat flux, the axially conducted heat increases and, thus, the minimum wall temperature in the metal plate decreases. The temperature difference in the metal plate between the temperature furthest from the condenser and the temperature closest to the condenser increases from $\Delta t = 4.6\,°\mathrm{C}$ for the lowest heat flux, over $\Delta t = 7.7\,°\mathrm{C}$ for the middle heat flux to $\Delta t = 11\,°\mathrm{C}$ for the highest heat flux. These temperature differences lead to the conclusion that both the axially conducted heat flow and the evaporative heat flow increase with increasing the heat flux. Alternating temperatures between the different sides of the system can be observed in the evaporator for all the heat fluxes. With increasing the heat flux, the temperature differences between the different sides of the system increase. Similar to the wall temperatures, the absolute value of the temperature difference in the vapor phase between the positions $z = 134\,\mathrm{mm}$ and $z = 46\,\mathrm{mm}$ increases from $\Delta t = 2.5\,°\mathrm{C}$ over $\Delta t = 3.1\,°\mathrm{C}$ to $\Delta t = 4.5\,°\mathrm{C}$ with increasing the heat flux.

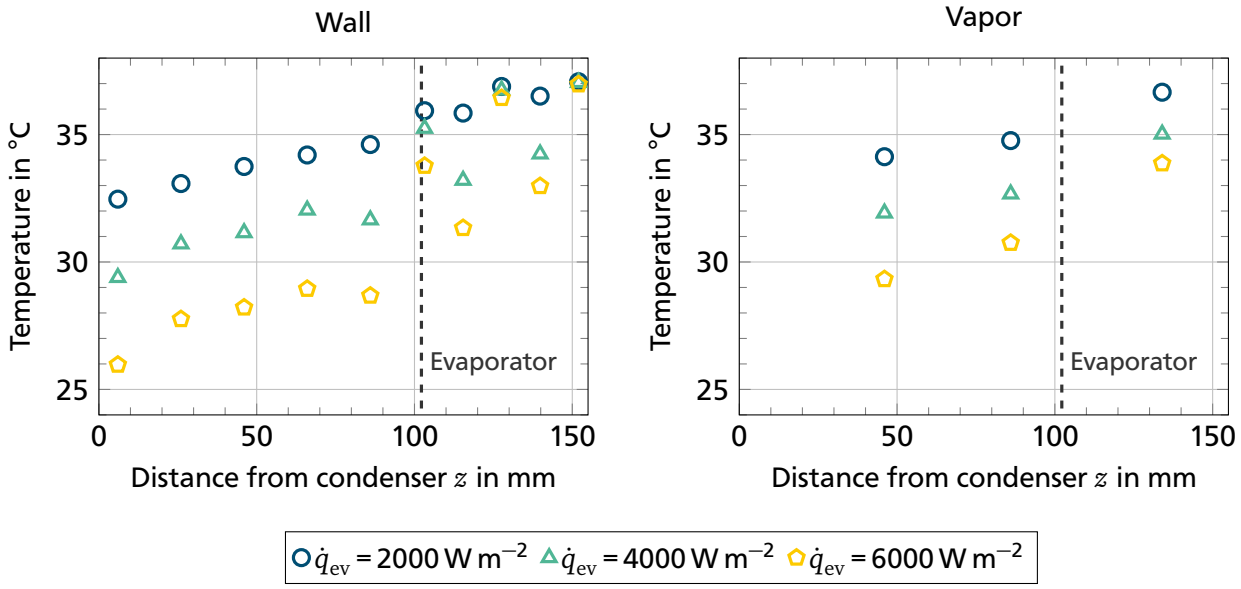

Figure 5.7: Temperatures in the walls of the capillary structure (left) and in the vapor phase (right) over the length of the triangular groove structure for an overall average ethanol mole fraction of $\widetilde{x}_{\mathrm{E,OA}} = 0.55$ to $\widetilde{x}_{\mathrm{E,OA}} = 0.56$ and an inclination angle of $\beta = 0°$ for three different heat fluxes ($\dot{q}_{ev} = 2000\,\mathrm{W\,m^{-2}}$, $\dot{q}_{ev} = 4000\,\mathrm{W\,m^{-2}}$, and $\dot{q}_{ev} = 6000\,\mathrm{W\,m^{-2}}$)

In Figure 5.8, the uncorrected results of the CHR measurements at the different positions in the system are depicted for the different heat fluxes. The groove filling is the highest for the lowest heat flux at every axial position. The menisci at the position $z = 30.5\,\mathrm{mm}$ for the heat fluxes $\dot{q}_{ev} = 4000\,\mathrm{W\,m^{-2}}$

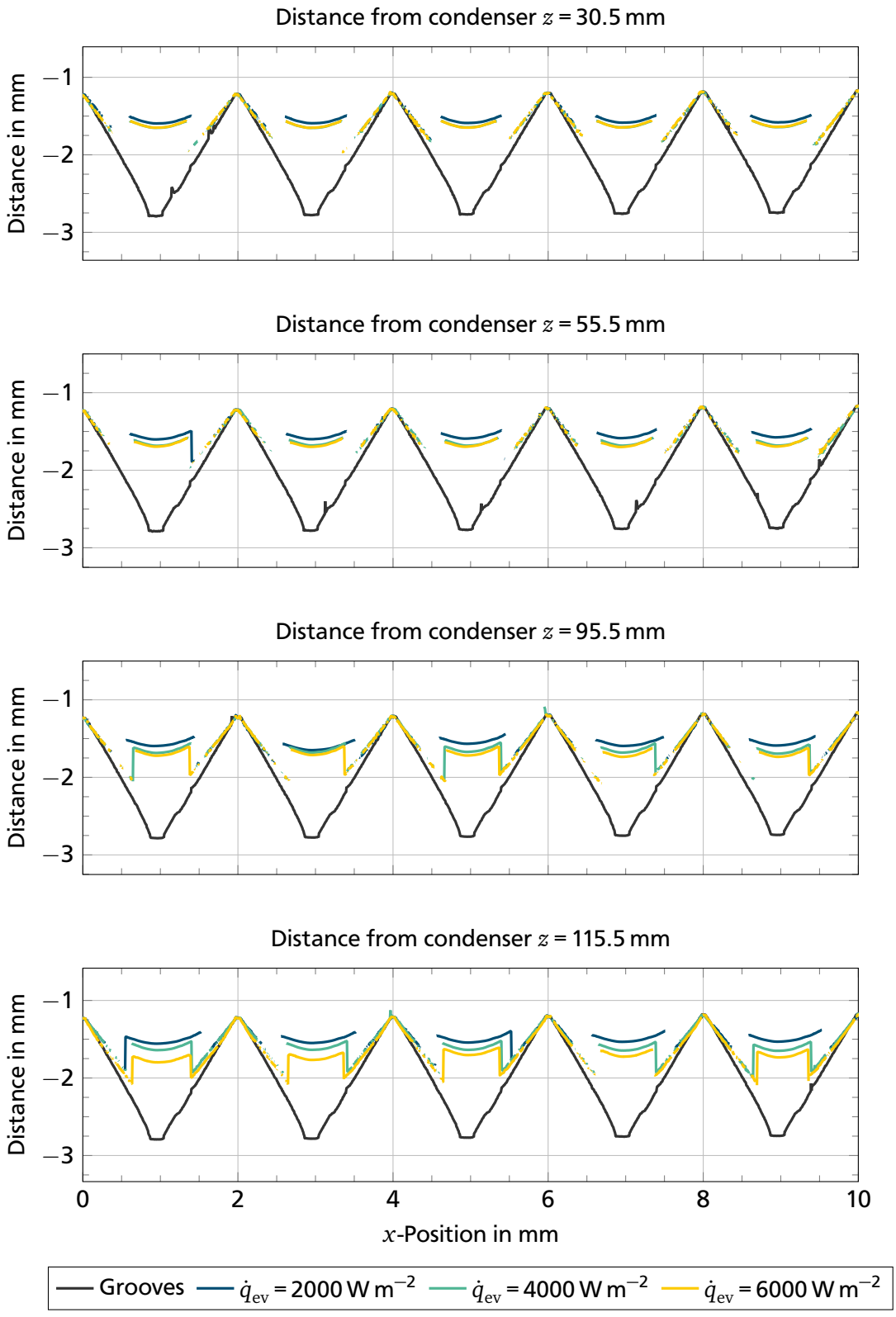

Figure 5.8: Liquid-vapor interface shape at different axial positions (z = 30.5 mm, z = 55.5 mm, z = 95.5 mm, and z = 115.5 mm) in the system for an overall average ethanol mole fraction of $\widetilde{x}_{E,OA}$ = 0.55 to $\widetilde{x}_{E,OA}$ = 0.56 and an inclination angle of β = 0° for three different heat fluxes ($\dot{q}_{ev}$ = 2000 W m^{-2}, $\dot{q}_{ev}$ = 4000 W m^{-2}, and $\dot{q}_{ev}$ = 6000 W m^{-2})

and $\dot{q}_{ev} = 6000\,W\,m^{-2}$ are almost identical. With increasing distance from the condenser, the shape of the menisci differs more strongly for the varied heat fluxes. For the highest heat flux, the decrease in groove filling towards the evaporator is the strongest. The groove filling for the lowest heat flux is nearly independent from the axial position. For the heat flux $\dot{q}_{ev} = 4000\,W\,m^{-2}$ the menisci lie between the lowest heat flux and the highest heat flux in the evaporator.

In Figure 5.9, the mean curvature radii in the parallel grooves at the four different distances from the condenser are depicted. For every heat flux, the mean curvature radius decreases strongly from position $z = 30.5\,mm$ to position $z = 55.5\,mm$. For the heat flux $\dot{q}_{ev} = 2000\,W\,m^{-2}$ the curvature radius increases to position $z = 95.5\,mm$ and remains nearly constant to position $z = 115.5\,mm$. For the two higher heat fluxes, the curvature radius is nearly constant for positions $z = 55.5\,mm$ and $z = 95.5\,mm$. For both heat fluxes, an increase in the mean curvature radius can be observed from position $z = 95.5\,mm$ to position $z = 115.5\,mm$. At each axial position, the curvature radii decrease with increasing the heat flux. For all experiments, the standard deviation of the measured curvature radii increases towards the evaporator.

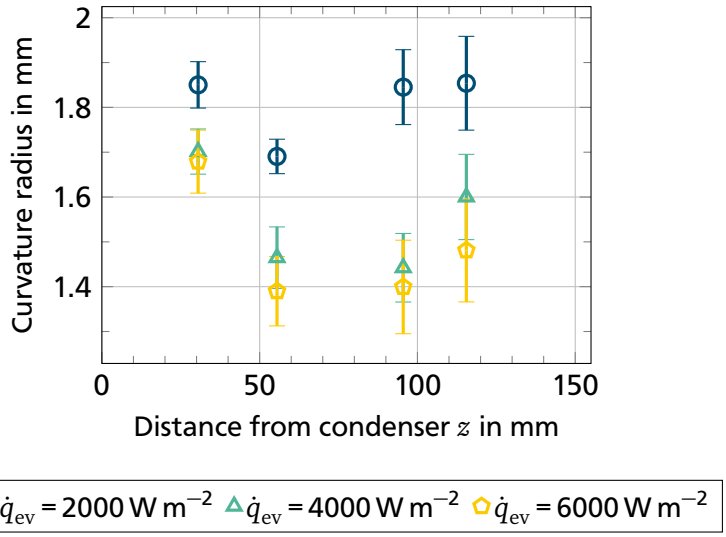

Figure 5.9: Mean curvature radii with standard deviations over the length of the capillary structure for an overall average ethanol mole fraction of $\widetilde{x}_{E,OA} = 0.55$ to $\widetilde{x}_{E,OA} = 0.56$ and an inclination angle of $\beta = 0°$ for three different heat fluxes ($\dot{q}_{ev} = 2000\,W\,m^{-2}$, $\dot{q}_{ev} = 4000\,W\,m^{-2}$, and $\dot{q}_{ev} = 6000\,W\,m^{-2}$)

In Figure 5.10, the calculated vapor ethanol mole fraction at the liquid-vapor interface is shown. Additionally, the overall average ethanol mole fraction is depicted. The interface ethanol mole fraction calculated from the vapor temperatures decreases monotonically towards the evaporator for all the heat fluxes. With increasing the heat flux the vapor ethanol mole fraction at the interface decreases at every axial position. At the position closest to the condenser, the ethanol fractions lie closer to each other than those at the position furthest away from the condenser. For the highest heat flux, the vapor interface ethanol mole fraction at the evaporator is lower than the overall average ethanol mole fraction. For the two lower heat fluxes, the vapor interface ethanol mole fraction is always equal to or above the overall average ethanol mole fraction.

In Figure 5.11, the calculated distribution of the capillary pressure is presented. For all the heat fluxes, the capillary pressure increases towards the evaporator. Whereas the influence of the heat flux on the

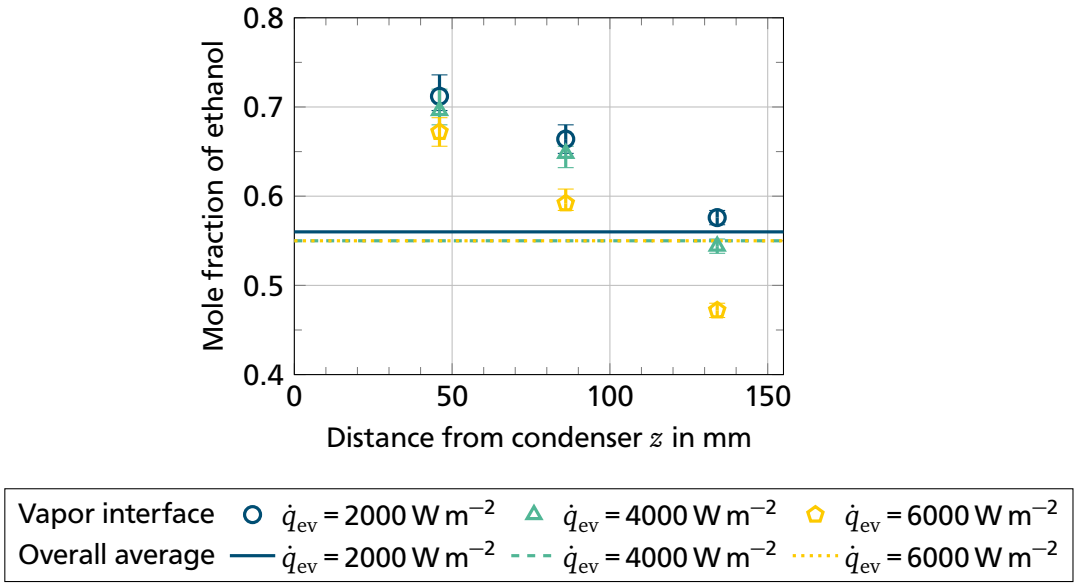

Figure 5.10: Vapor ethanol mole fractions at the interface calculated from vapor temperature measurements compared to overall average ethanol mole fractions over the length of the triangular groove structure for an overall average ethanol mole fraction of $\widetilde{x}_{E,OA} = 0.55$ to $\widetilde{x}_{E,OA} = 0.56$ and an inclination angle of $\beta = 0°$ for three different heat fluxes ($\dot{q}_{ev} = 2000\ W\,m^{-2}$, $\dot{q}_{ev} = 4000\ W\,m^{-2}$, and $\dot{q}_{ev} = 6000\ W\,m^{-2}$)

capillary pressure is weak close to the condenser, the capillary pressures differ more strongly towards the evaporator. With increasing the heat flux, the capillary pressure increases at every axial position. Thus, the capillary pressure difference between the position furthest from the condenser and closest to the condenser increases with increasing the heat flux. This observation meets the expectations, since the evaporative mass flow increases with increasing the heat flux. Thus, a higher capillary pressure difference is needed to sustain the fluid circulation.

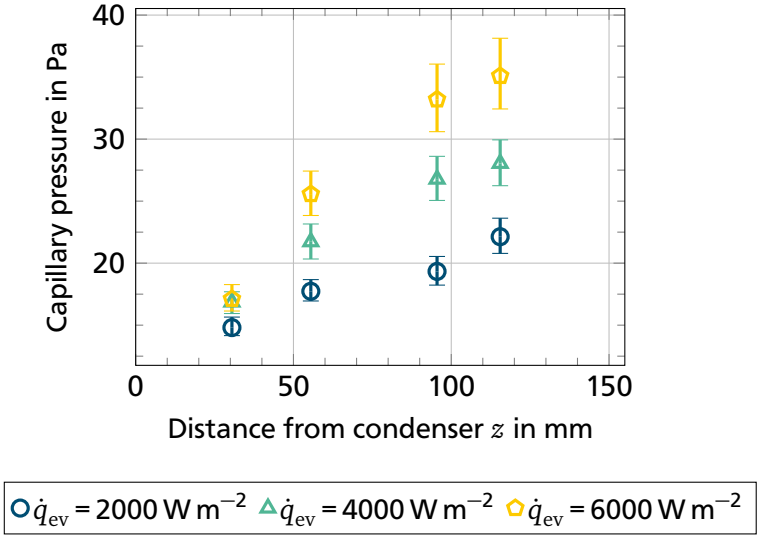

Figure 5.11: Capillary pressure calculated from temperature measurements and CHR measurements over the length of the triangular groove structure for an overall average ethanol mole fraction of $\widetilde{x}_{E,OA} = 0.55$ to $\widetilde{x}_{E,OA} = 0.56$ and an inclination angle of $\beta = 0°$ for three different heat fluxes ($\dot{q}_{ev} = 2000\ W\,m^{-2}$, $\dot{q}_{ev} = 4000\ W\,m^{-2}$, and $\dot{q}_{ev} = 6000\ W\,m^{-2}$)

In Figure 5.12, the difference between the distilled condenser ethanol mole fraction and the overall average ethanol mole fraction is presented for the three experiments. With increasing the heat flux, this difference decreases. Thus, the separation gets worse. The measured difference is at a value of $\widetilde{x}_{\mathrm{E,D}} - \widetilde{x}_{\mathrm{E,OA}} = 0.13$ for the lowest heat flux, at a value of $\widetilde{x}_{\mathrm{E,D}} - \widetilde{x}_{\mathrm{E,OA}} = 0.09$ for the heat flux $\dot{q}_{\mathrm{ev}} = 4000\,\mathrm{W\,m^{-2}}$ and at a value of $\widetilde{x}_{\mathrm{E,D}} - \widetilde{x}_{\mathrm{E,OA}} = 0.06$ for the highest heat flux. Since no statements on the mean axial composition can be drawn from the vapor interface ethanol fractions shown in Figure 5.10, these values cannot be directly put in context with the distilled condenser mole fraction.

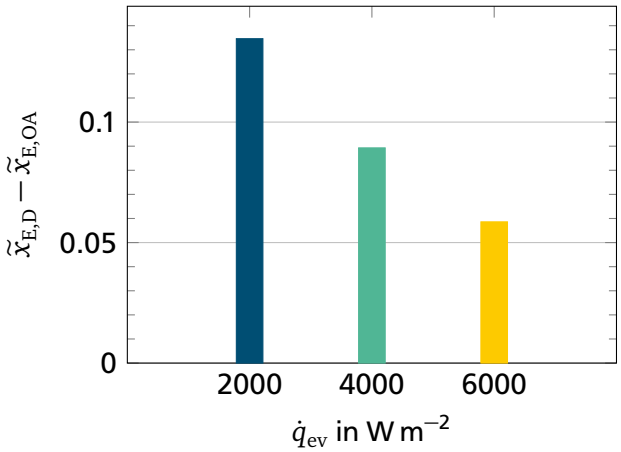

Figure 5.12: Difference between distilled condenser ethanol mole fraction and overall average ethanol mole fraction for the triangular groove structure for an overall average ethanol mole fraction of $\widetilde{x}_{\mathrm{E,OA}} = 0.55$ to $\widetilde{x}_{\mathrm{E,OA}} = 0.56$ and an inclination angle of $\beta = 0°$ for three different heat fluxes ($\dot{q}_{\mathrm{ev}} = 2000\,\mathrm{W\,m^{-2}}$, $\dot{q}_{\mathrm{ev}} = 4000\,\mathrm{W\,m^{-2}}$, and $\dot{q}_{\mathrm{ev}} = 6000\,\mathrm{W\,m^{-2}}$)

In Table 5.3, the measured pressures in the system in a steady-state condition are shown. With increasing the heat flux, the pressure decreases. Since the wall temperature furthest from the condenser was fixed for all experiments, the vapor temperatures at the evaporator are similar for all the heat fluxes. Because of the increasing axial temperature differences in the vapor phase with increasing the heat flux, the average vapor temperature decreases with increasing the heat flux. This leads to a reduction of the vapor pressure.

Table 5.3: Pressures of the experiments with varied heat flux for the triangular groove structure

	$\dot{q}_{\mathrm{ev}} = 2000\,\mathrm{W\,m^{-2}}$	$\dot{q}_{\mathrm{ev}} = 4000\,\mathrm{W\,m^{-2}}$	$\dot{q}_{\mathrm{ev}} = 6000\,\mathrm{W\,m^{-2}}$
p in mbar	124.6	109.0	92.2

Discussion of the Influence of the Heat Flux

With increasing the heat flux, the axial flow rate increases. Additionally, the axially conducted heat flow increases. The resulting interface compositions show that the fraction of ethanol at the interface increases with decreasing heat flux. Additionally, the absolute difference of the interface ethanol mole fraction between the position closest to the condenser and the position at the evaporator increases with increasing heat flux. The ethanol fraction of the sample withdrawn at the condenser gets higher with a lower heat flux. Thus, the separation is the strongest in this case; therefore, the ethanol fraction at the

evaporator must also be lower for this experiment. This means that the difference between the liquid interface fraction of ethanol and the axial mean liquid fraction of ethanol at the evaporator must be the highest for the lowest heat flux. With increasing the heat flux, the liquid gets pulled back further in the grooves. The capillary pressure difference rises with increasing the heat flux.

5.1.3 Influence of the Inclination

In this section, three experiments with similar overall average fluid compositions are evaluated at three different inclination angles $\beta = -0.4°$, $\beta = 0°$, and $\beta = 0.4°$ for the same heat flux. A positive inclination angle indicates that the evaporator lies above the condenser. For a negative inclination angle, the evaporator lies below the condenser. In Figure 5.13, the measured temperatures in the walls of the capillary structure and in the vapor phase are shown for the three values of the inclination angle. With increasing the inclination, the minimum temperature in the wall of the capillary structure closest to the condenser decreases. For all inclination angles, a spread between the wall temperatures of the different sides in the system can be seen. Referring to the positions of the temperature sensors shown in Figure 4.5, the temperatures in the walls are lower on the left side of the system for the inclination angles $\beta = 0°$ and $\beta = 0.4°$, whereas the temperatures are lower on the right side of the system for the inclination angle $\beta = -0.4°$. The vapor temperatures increase monotonically from the condenser to the evaporator. The measured vapor temperature difference between position $z = 46\,\text{mm}$ and position $z = 134\,\text{mm}$ is lowest for the horizontal system with $\Delta t = 3.1\,°\text{C}$ and at a maximum of $\Delta t = 4.3\,°\text{C}$ for the positive inclination angle.

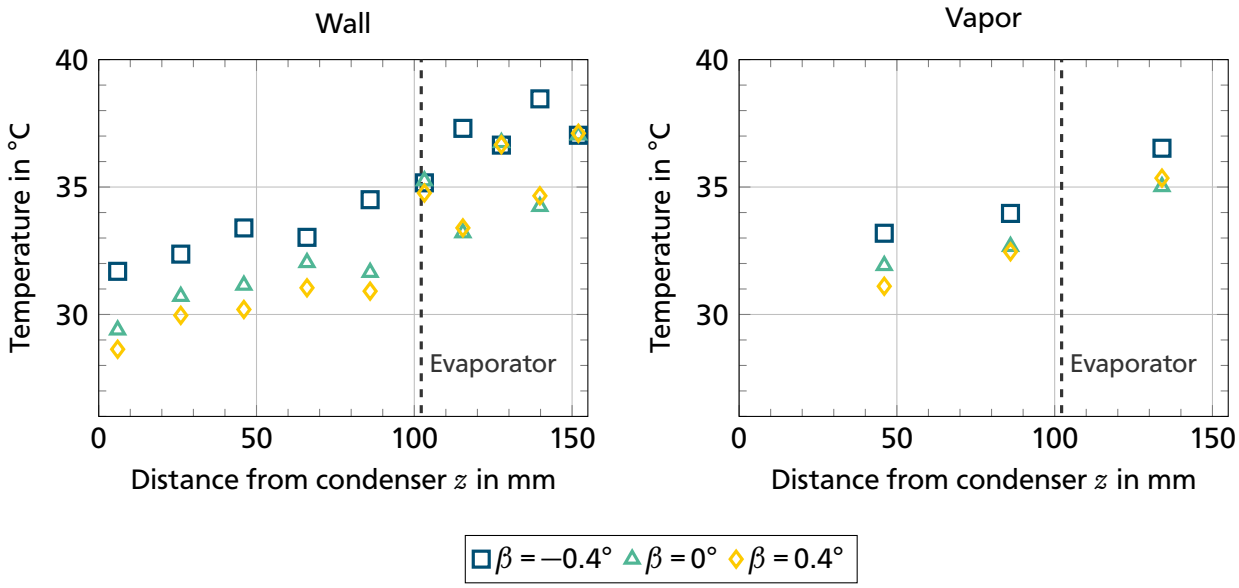

Figure 5.13: Temperatures in the walls of the capillary structure (left) and in the vapor phase (right) over the length of the triangular groove structure for an overall average ethanol mole fraction of $\widetilde{x}_{\text{E,OA}} = 0.55$ to $\widetilde{x}_{\text{E,OA}} = 0.56$ and a heat flux of $\dot{q}_{\text{ev}} = 4000\,\text{W m}^{-2}$ for three different inclination angles ($\beta = -0.4°$, $\beta = 0°$, and $\beta = 0.4°$)

In Figure 5.14, the measurements of the CHR sensor over five grooves at different axial positions in the system are shown for the three different inclination angles. At the position closest to the condenser, the

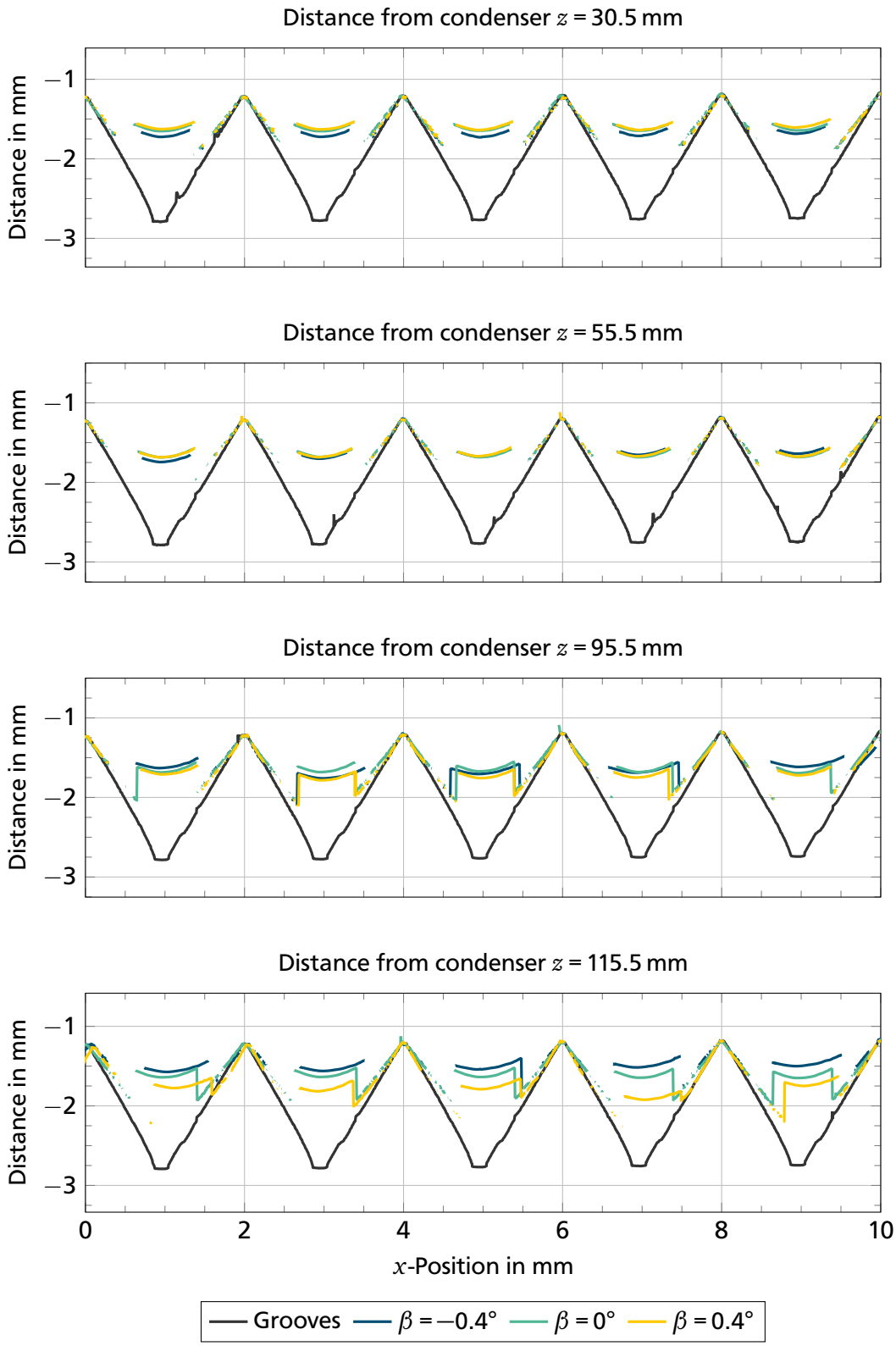

Figure 5.14: Liquid-vapor interface shape at different axial positions (z = 30.5 mm, z = 55.5 mm, z = 95.5 mm and z = 115.5 mm) in the system for an overall average ethanol mole fraction of $\widetilde{x}_{\mathrm{E,OA}} = 0.55$ to $\widetilde{x}_{\mathrm{E,OA}} = 0.56$ and a heat flux of $\dot{q}_{\mathrm{ev}} = 4000\,\mathrm{W\,m^{-2}}$ for three different inclination angles ($\beta = -0.4°$, $\beta = 0°$, and $\beta = 0.4°$)

groove filling and curvature is similar for the two test runs with the inclination angles $\beta = 0°$ and $\beta = 0.4°$. The grooves at the negative inclination are filled less. At the position $z = 55.5\,\text{mm}$ the menisci look very similar for all three experiments. Moving closer towards the evaporator, the differences between the experiments get stronger. At position $z = 95.5\,\text{mm}$, slight differences in the groove filling can be observed between the different experiments but also from one groove to another. At the position $z = 115.5\,\text{mm}$, the groove filling is very similar to the other axial positions for the experiment with a horizontal plate. At this position, the strongest differences to the experiments with negative and positive inclination can be seen. At a negative inclination angle, gravity assists the liquid flow and the groove filling is higher at the evaporator than at the positions before. For the positive inclination angle, gravity depletes the liquid flow. A decrease in filling ratio from the condenser to the evaporator can be observed for this experiment. At position $z = 115.5\,\text{mm}$, strong differences in the meniscus shapes between the parallel grooves can be observed for the positive inclination angle.

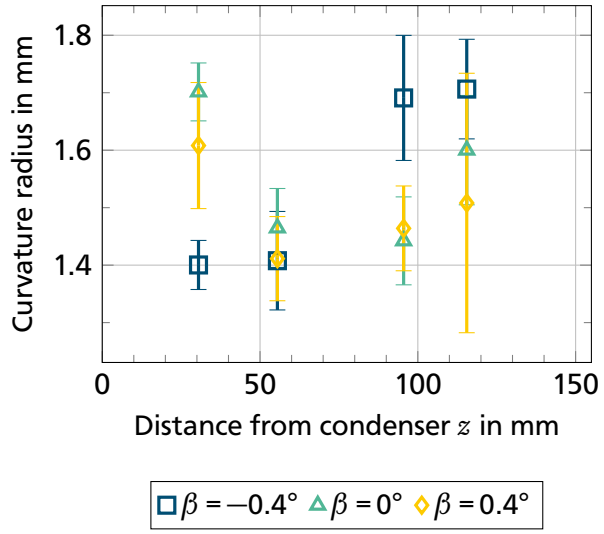

Figure 5.15: Mean curvature radii with standard deviations over the length of the triangular groove structure for an overall average ethanol mole fraction of $\widetilde{x}_{\text{E,OA}} = 0.55$ to $\widetilde{x}_{\text{E,OA}} = 0.56$ and a heat flux of $\dot{q}_{\text{ev}} = 4000\,\text{W m}^{-2}$ for three different inclination angles ($\beta = -0.4°$, $\beta = 0°$, and $\beta = 0.4°$)

In Figure 5.15, the mean curvature radii are shown over the length of the system. The distributions of the curvature radii for the different experiments intersect and do not follow a general trend. Similar to the experiments with varied fluid composition and heat flux, the curvature radius decreases from position $z = 30.5\,\text{mm}$ to position $z = 55.5\,\text{mm}$ for the experiments in horizontal position and at $\beta = 0.4°$. For the negative inclination angle, the curvature radius remains almost constant between these positions. A strong increase in curvature radius can be observed for this inclination angle from $z = 55.5\,\text{mm}$ to position $z = 95.5\,\text{mm}$. From this position towards the evaporator, only a slight increase in curvature radius can be observed. For the positive inclination angle, an increase in mean curvature radius can be seen from position $z = 55.5\,\text{mm}$ to position $z = 115.5\,\text{mm}$. It is noteworthy that the standard deviation at the position $z = 115.5\,\text{mm}$ is comparatively high for this experiment. The strong differences in meniscus shapes observed in Figure 5.14 explain the high value of the standard deviation at this position. For the experiment with a horizontal plate, a slight decrease in curvature radius can be observed from

$z = 55.5\,\text{mm}$ to position $z = 95.5\,\text{mm}$. The curvature radius then strongly increases in the evaporator zone.

In Figure 5.16, the composition at the interface over the length of the system calculated from the vapor temperatures, as well as the overall average ethanol mole fractions are depicted. The ethanol fraction at the interface calculated from the temperatures decreases monotonically for every experiment. The absolute value of the slope in horizontal position is lower than for the two inclined systems. With increasing the inclination, the ethanol fraction at the interface decreases at every axial position. The vapor interface ethanol mole fractions are mostly higher than or equal to the overall average ethanol mole fraction for all experiments. Only for the positive inclination angle, is the vapor interface ethanol mole fraction in the evaporator clearly below the overall average ethanol mole fraction in the system.

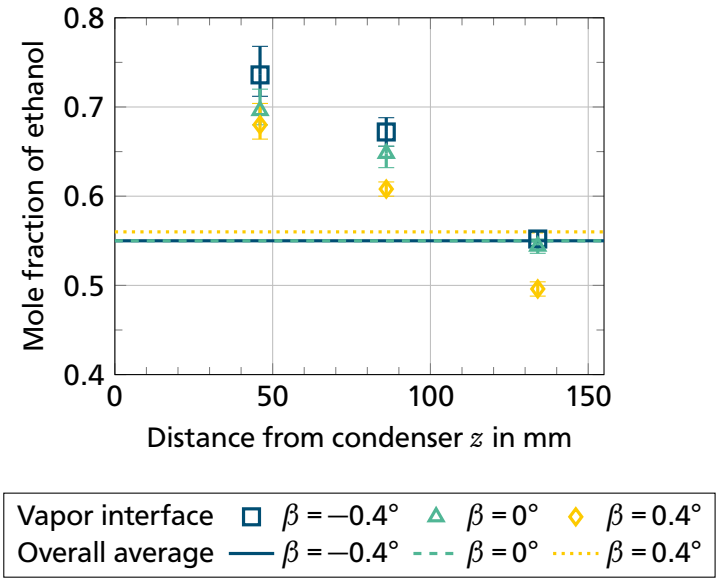

Figure 5.16: Vapor ethanol mole fractions at the interface calculated from vapor temperature measurements compared to overall average ethanol mole fractions over the length of the triangular groove structure for an overall average ethanol mole fraction of $\widetilde{x}_{\text{E,OA}} = 0.55$ to $\widetilde{x}_{\text{E,OA}} = 0.56$ and a heat flux of $\dot{q}_{\text{ev}} = 4000\,\text{W m}^{-2}$ for three different inclination angles ($\beta = -0.4°$, $\beta = 0°$, and $\beta = 0.4°$)

In Figure 5.17, the calculated distributions of the capillary pressure are shown for the experiments with varied inclinations. The capillary pressures closest to the condenser are very similar for the different inclination angles. Towards the evaporator, the capillary pressures deviate more strongly. The increase in capillary pressure is smallest for the experiment with the negative inclination angle. Since gravity assists the liquid flow, a smaller capillary pressure difference is needed to sustain the fluid circulation. The capillary pressure difference between the position furthest from the condenser and closest to the condenser is highest for the experiment with the positive inclination angle. Here, gravity works against the liquid flow and the capillary pressure difference must therefore increase. Due to the high standard deviation of the measured curvature radii, the uncertainty of the capillary pressure at position $z = 115.5\,\text{mm}$ is comparatively high for this experiment. As expected, the horizontal experiment shows an increase in capillary pressure which is in between the other two experiments.

In Figure 5.18, the difference between the distilled condenser ethanol mole fraction and the overall average ethanol mole fraction is shown. For the negative inclination angle, this difference is the highest

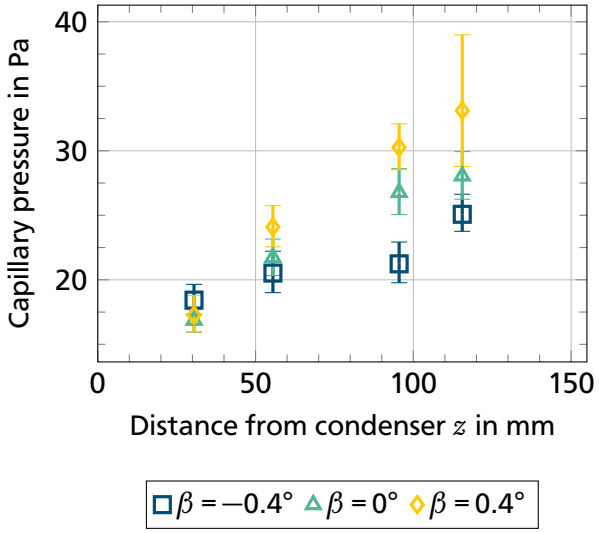

Figure 5.17: Capillary pressure calculated from temperature measurements and CHR measurements over the length of the triangular groove structure for an overall average ethanol mole fraction of $\widetilde{x}_{\mathrm{E,OA}} = 0.55$ to $\widetilde{x}_{\mathrm{E,OA}} = 0.56$ and a heat flux of $\dot{q}_{\mathrm{ev}} = 4000\,\mathrm{W\,m^{-2}}$ for three different inclination angles ($\beta = -0.4°$, $\beta = 0°$, and $\beta = 0.4°$)

with a value above 0.2. The difference between the experiment with a horizontal plate and the experiment with a positive inclination is small. The strong difference between the negatively inclined case and the other two cases is not evident from the vapor interface ethanol fractions shown in Figure 5.16. Nevertheless, the results shown in Figure 5.16 are not in contradiction to the ones shown in Figure 5.18 since one cannot deduce the mean axial ethanol mole fractions from the interface ethanol fractions.

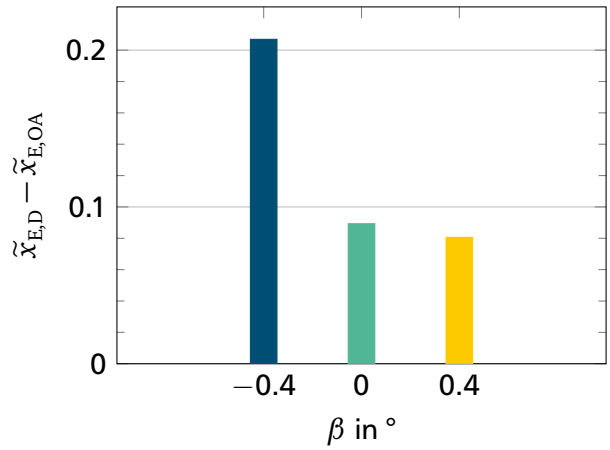

Figure 5.18: Difference between distilled condenser ethanol mole fraction and overall average ethanol mole fraction for the triangular groove structure for an overall average ethanol mole fraction of $\widetilde{x}_{\mathrm{E,OA}} = 0.55$ to $\widetilde{x}_{\mathrm{E,OA}} = 0.56$ and a heat flux of $\dot{q}_{\mathrm{ev}} = 4000\,\mathrm{W\,m^{-2}}$ for three different inclination angles ($\beta = -0.4°$, $\beta = 0°$, and $\beta = 0.4°$)

In Table 5.4 the measured pressures in the system for the experiments with varied inclination angles are presented. With increasing the inclination angle, the pressure in the system decreases.

Table 5.4: Pressures of the experiments with varied inclination for the triangular groove structure

	$\beta = -0.4°$	$\beta = 0°$	$\beta = 0.4°$
p in mbar	119.8	109.0	103.1

Discussion of the Influence of the Inclination

Changing the inclination in the system has a strong influence on the measured curvature radii and the resulting capillary pressure. Whereas the measured curvature radii differ strongly from groove to groove in the evaporator when gravity works against the liquid flow (positive inclination angle), the menisci in the evaporator are more uniform when gravity supports the liquid flow (negative inclination angle). In the range of these measurements, the impact of the changed inclination on the heat transfer processes is relatively low for the inclination angles $\beta = 0°$ and $\beta = 0.4°$. Only for the negative inclination angle, are the differences in the temperatures stronger. Here, the temperature difference between the two sides of the system, which can be seen for all experiments with varied inclination, is shifted to the other side of the system. The reason for this shift is not clearly identifiable. Due to the higher mean temperature for the negative inclination, the pressure in the system is the highest compared to the horizontal and the positively inclined experiment. For the negative inclination, the measured change in the ethanol fractions between the distilled condenser sample and the overall average is significantly higher than for the other experiments.

5.2 Advanced Rectangular Groove Structure

In the following section the results for the advanced rectangular groove structure (see Figure 4.6b) are presented. For this capillary structure, three different mixtures were tested. Due to the smaller channels and the higher inclination of the channel walls, the CHR measurement technique is less suitable for this capillary structure and was therefore not used in these experiments. For this capillary structure, the overall average ethanol mole fractions $\widetilde{x}_{\mathrm{E,OA}} = 0.56$, $\widetilde{x}_{\mathrm{E,OA}} = 0.73$, and $\widetilde{x}_{\mathrm{E,OA}} = 0.90$ were tested. In Figure 5.19, the temperatures in the walls of the capillary structures and in the vapor phase are depicted for the three experiments. The temperatures at the position closest to the condenser lie closely to each other for all three experiments. Similar to the triangular groove structure, a temperature difference can be observed between the different sides of the system for the experiments with the overall average ethanol mole fractions $\widetilde{x}_{\mathrm{E,OA}} = 0.56$ and $\widetilde{x}_{\mathrm{E,OA}} = 0.73$. For these two experiments, these temperature differences are shifted in opposite directions. For the vapor phase, a clearer trend can be seen. Here, the lowest overall average ethanol mole fraction shows the highest temperature difference between the temperature measured closest to the condenser and furthest from the condenser.

In Figure 5.20, the vapor ethanol mole fraction at the interface calculated from the temperature measurements in the vapor phase over the distance from the condenser is shown for three values of the overall average ethanol mole fraction. With increasing distance from the condenser, the ethanol fraction at the interface decreases monotonically for all experiments. For higher overall average ethanol mole fractions, the ethanol fraction at the interface is higher at every axial position. For the overall average ethanol mole fraction $\widetilde{x}_{\mathrm{E,OA}} = 0.56$, the vapor interface ethanol mole fraction is higher than the overall

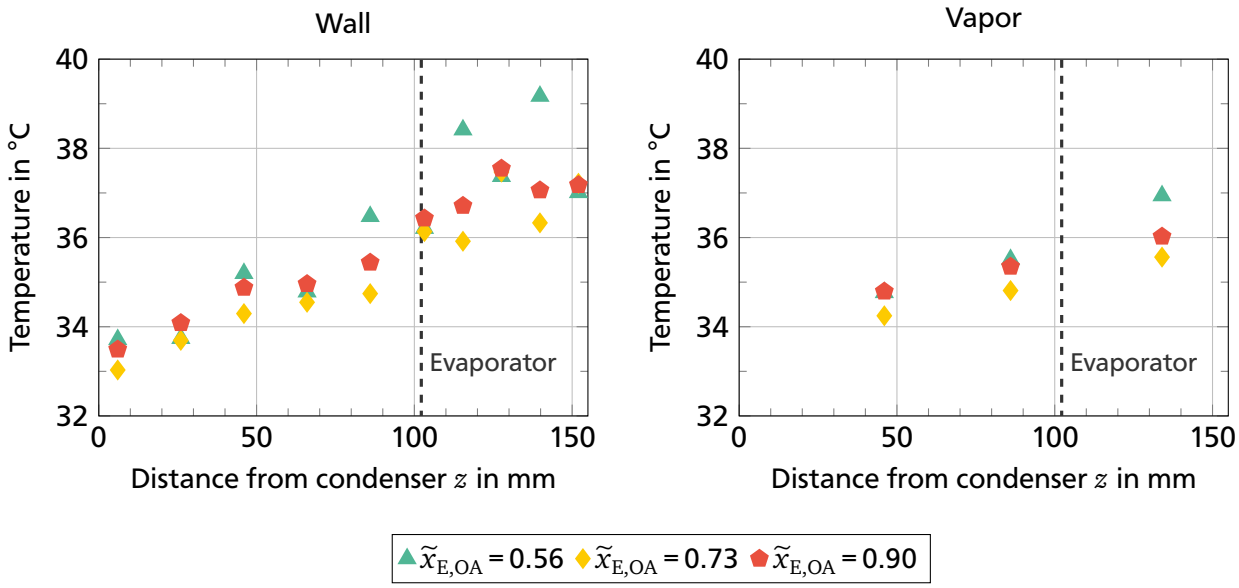

Figure 5.19: Temperatures in the walls of the capillary structure (left) and in the vapor phase (right) over the length of the advanced rectangular groove structure for a heat flux of $\dot{q}_{ev} = 4000\,\mathrm{W\,m^{-2}}$ and an inclination angle of $\beta = 0°$ for three different overall average ethanol mole fractions ($\widetilde{x}_{E,OA} = 0.56$, $\widetilde{x}_{E,OA} = 0.73$, and $\widetilde{x}_{E,OA} = 0.90$)

average ethanol mole fraction at every axial position. For the highest overall average ethanol mole fraction $\widetilde{x}_{E,OA} = 0.90$, the vapor ethanol mole fraction at the interface is always lower than the overall average ethanol mole fraction. The vapor ethanol mole fractions at the interface for the overall average ethanol mole fraction $\widetilde{x}_{E,OA} = 0.73$ are higher or lower than the overall average ethanol mole fraction depending on the axial position.

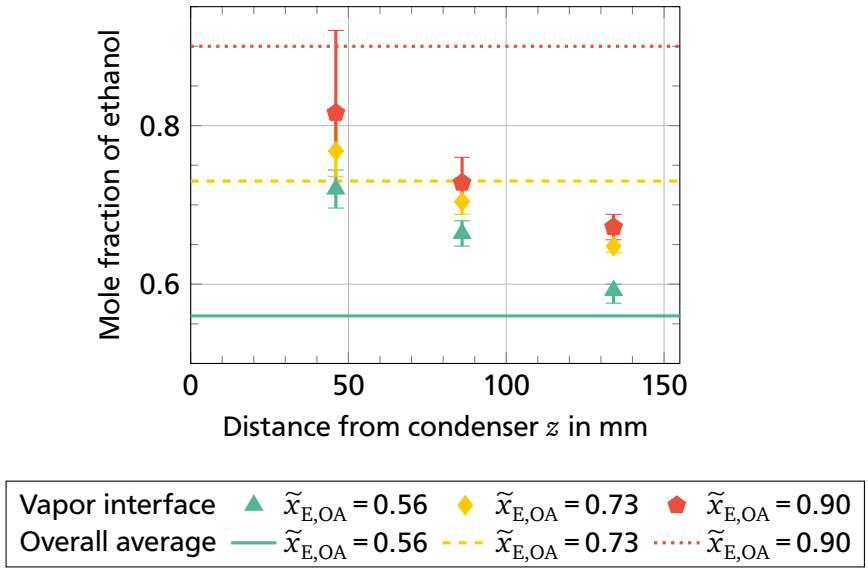

Figure 5.20: Vapor ethanol mole fractions at the interface calculated from vapor temperature measurements over the length of the advanced rectangular groove structure for a heat flux of $\dot{q}_{ev} = 4000\,\mathrm{W\,m^{-2}}$ and an inclination angle of $\beta = 0°$ for three different overall average ethanol mole fractions ($\widetilde{x}_{E,OA} = 0.56$, $\widetilde{x}_{E,OA} = 0.73$, and $\widetilde{x}_{E,OA} = 0.90$)

In Figure 5.21, the difference between the ethanol fraction in the distilled sample withdrawn at the condenser and the overall average ethanol mole fraction is shown. With increasing the overall average ethanol mole fraction, this difference decreases. Whereas this difference is at a value of $\widetilde{x}_{\mathrm{E,D}} - \widetilde{x}_{\mathrm{E,OA}} = 0.11$ for the overall average ethanol mole fraction $\widetilde{x}_{\mathrm{E,OA}} = 0.56$, it is only at a value of $\widetilde{x}_{\mathrm{E,D}} - \widetilde{x}_{\mathrm{E,OA}} = 0.02$ for the overall average ethanol mole fraction $\widetilde{x}_{\mathrm{E,OA}} = 0.73$ and close to zero for the overall average ethanol mole fraction $\widetilde{x}_{\mathrm{E,OA}} = 0.90$.

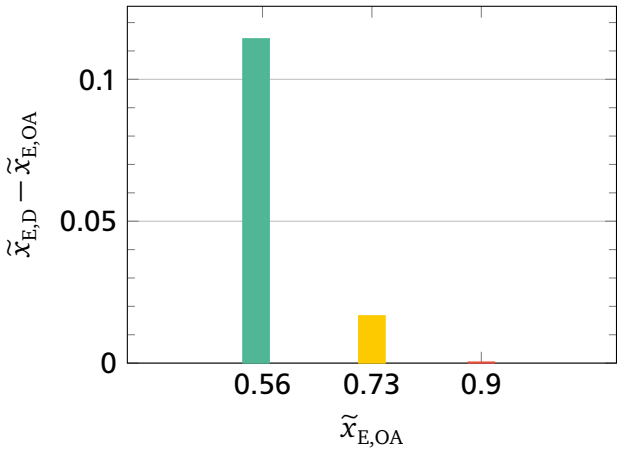

Figure 5.21: Difference between distilled condenser ethanol mole fraction and overall average ethanol mole fraction for the advanced rectangular groove structure for a heat flux of $\dot{q}_{\mathrm{ev}} = 4000\,\mathrm{W\,m^{-2}}$ and an inclination angle of $\beta = 0°$ for three different overall average ethanol mole fractions ($\widetilde{x}_{\mathrm{E,OA}} = 0.56$, $\widetilde{x}_{\mathrm{E,OA}} = 0.73$, and $\widetilde{x}_{\mathrm{E,OA}} = 0.90$)

In Table 5.5 the measured pressures are shown for the three experiments. The pressure is lowest for the overall average ethanol mole fraction $\widetilde{x}_{\mathrm{E,OA}} = 0.73$. Thus, the pressure does not monotonically increase with increasing the overall average ethanol mole fraction. Corresponding to the temperature shift in the walls above the controlled 37 °C at $z = 152\,\mathrm{mm}$ for $\widetilde{x}_{\mathrm{E,OA}} = 0.56$, the vapor temperatures and the pressure are comparatively high for this mixture. The pressure is higher for $\widetilde{x}_{\mathrm{E,OA}} = 0.56$ than for the experiment with $\widetilde{x}_{\mathrm{E,OA}} = 0.73$.

Table 5.5: Pressures of the experiments with varied fluid composition for the advanced rectangular groove structure

	$\widetilde{x}_{\mathrm{E,OA}} = 0.56$	$\widetilde{x}_{\mathrm{E,OA}} = 0.73$	$\widetilde{x}_{\mathrm{E,OA}} = 0.90$
p in mbar	129.3	128.6	134.2

5.3 Comparison of Capillary Structures

In Figure 5.22, the comparison of the temperature distributions for the triangular groove structure and the advanced rectangular groove structure is shown for an overall average ethanol mole fraction of $\widetilde{x}_{\mathrm{E,OA}} = 0.55$ and $\widetilde{x}_{\mathrm{E,OA}} = 0.56$. The minimum wall temperature close to the condenser is considerably lower for the triangular groove structure than for the advanced rectangular groove structure. For both experiments, a temperature difference between the different sides of the system can be observed. While

the temperature furthest from the condenser is controlled at 37 °C in both experiments, the temperature distribution in the walls of the capillary structure is shifted to higher values for the advanced rectangular groove structure and shifted to lower values for the triangular groove structure. Nevertheless, the temperature difference between the maximum wall temperature and the minimum wall temperature is considerably smaller for the advanced rectangular groove structure. The temperature difference between the sensor furthest from the condenser and the sensor closest to the condenser in the vapor phase is at 2.2 °C for the advanced rectangular groove structure and at 3.1 °C for the triangular groove structure.

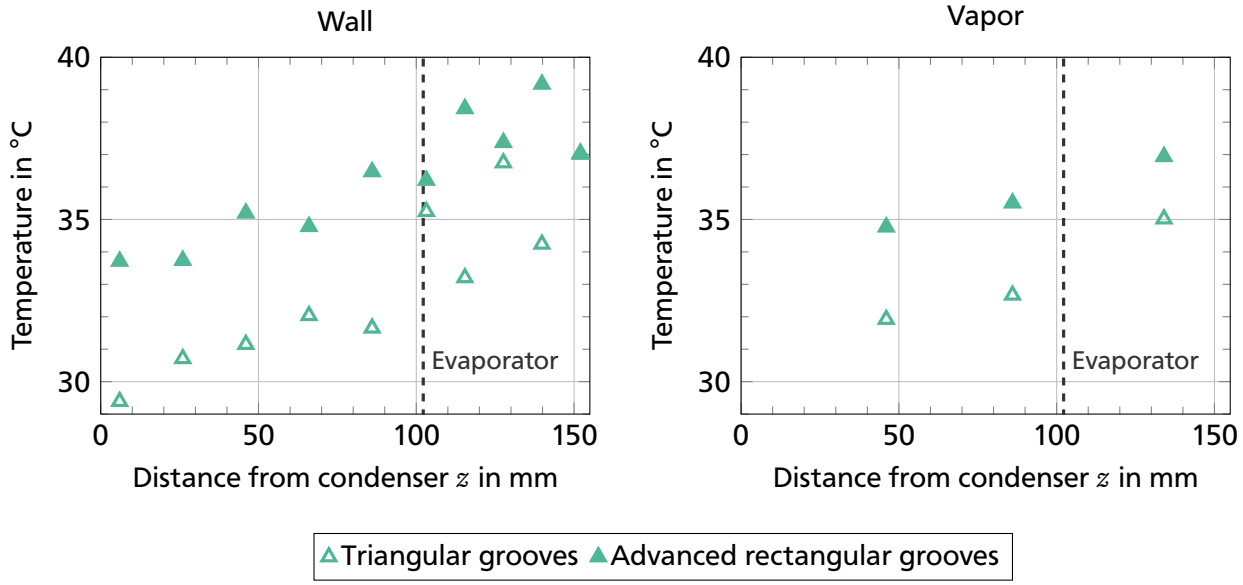

Figure 5.22: Temperatures in the walls of the capillary structure (left) and in the vapor phase (right) over the length of the system for an overall average ethanol mole fraction of $\widetilde{x}_{\mathrm{E,OA}} = 0.55$ to $\widetilde{x}_{\mathrm{E,OA}} = 0.56$, a heat flux of $\dot{q}_{\mathrm{ev}} = 4000\,\mathrm{W\,m^{-2}}$, and an inclination angle of $\beta = 0°$ for the triangular groove structure and the advanced rectangular groove structure

In Figure 5.23, the temperature distributions are evaluated for the overall average ethanol fraction $\widetilde{x}_{\mathrm{E,OA}} = 0.71$ and $\widetilde{x}_{\mathrm{E,OA}} = 0.73$. For this overall average fluid composition, the wall temperatures are similar to each other. Whereas a temperature difference between the sides of the system can be observed for the advanced rectangular groove structure, it can barely be observed for the triangular groove structure. For the vapor temperatures, the difference between the temperature furthest from the condenser and the temperature closest to the condenser is higher for the triangular groove structure. This observation agrees with the comparison of the vapor temperatures for the overall average ethanol mole fraction $\widetilde{x}_{\mathrm{E,OA}} = 0.55/0.56$.

In Figure 5.24, the distribution of the vapor interface ethanol fraction in the system is shown for an overall average ethanol mole fraction of $\widetilde{x}_{\mathrm{E,OA}} = 0.55$ and $\widetilde{x}_{\mathrm{E,OA}} = 0.56$. For the advanced rectangular groove structure, the ethanol mole fraction at the interface is always higher than for the triangular groove structure. For the advanced rectangular groove structure, the vapor interface mole fraction is considerably higher than the overall average ethanol mole fraction at every axial position. For the triangular groove structure, the vapor ethanol mole fraction at the interface is slightly below the overall average ethanol mole fraction in the evaporator. At the other two positions, it is clearly higher than the overall average ethanol mole fraction. The difference between the distilled condenser ethanol mole fraction and the overall

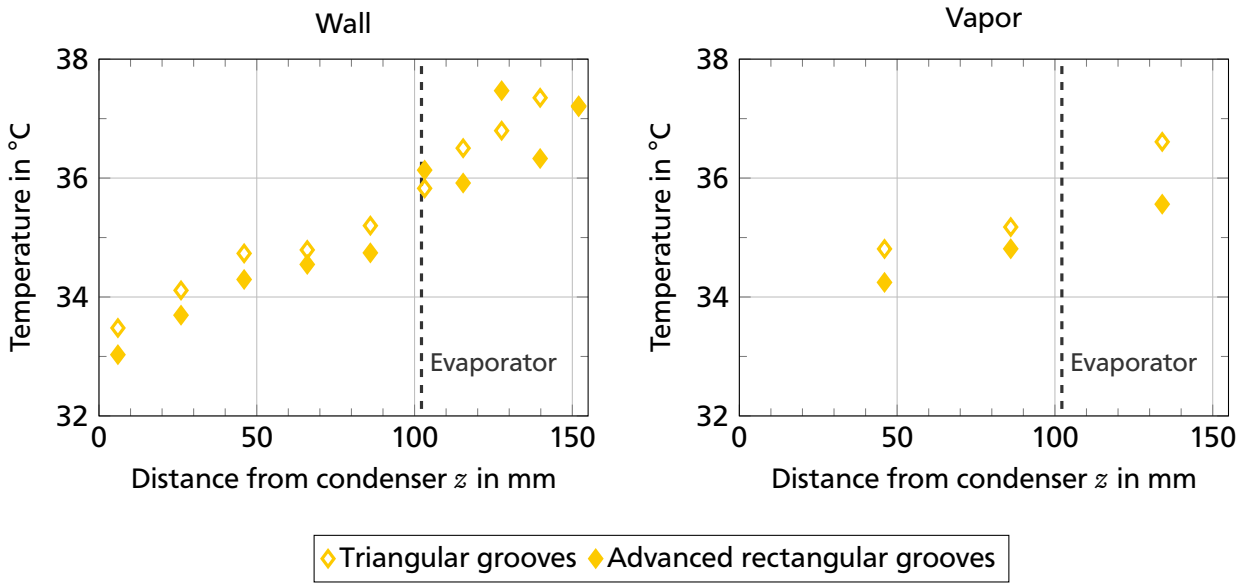

Figure 5.23: Temperatures in the walls of the capillary structure (left) and in the vapor phase (right) over the length of the system for an overall average ethanol mole fraction of $\widetilde{x}_{\mathrm{E,OA}} = 0.71$ to $\widetilde{x}_{\mathrm{E,OA}} = 0.73$, a heat flux of $\dot{q}_{\mathrm{ev}} = 4000\,\mathrm{W\,m^{-2}}$, and an inclination angle of $\beta = 0°$ for the triangular groove structure and the advanced rectangular groove structure

average ethanol mole fraction is at $\widetilde{x}_{\mathrm{E,D}} - \widetilde{x}_{\mathrm{E,OA}} = 0.11$ for the advanced rectangular groove structure and at a value of $\widetilde{x}_{\mathrm{E,D}} - \widetilde{x}_{\mathrm{E,OA}} = 0.09$ for the triangular groove structure. Thus, the measured separation is stronger for the advanced rectangular groove structure. The measured pressure is considerably lower for the triangular groove structure in this case.

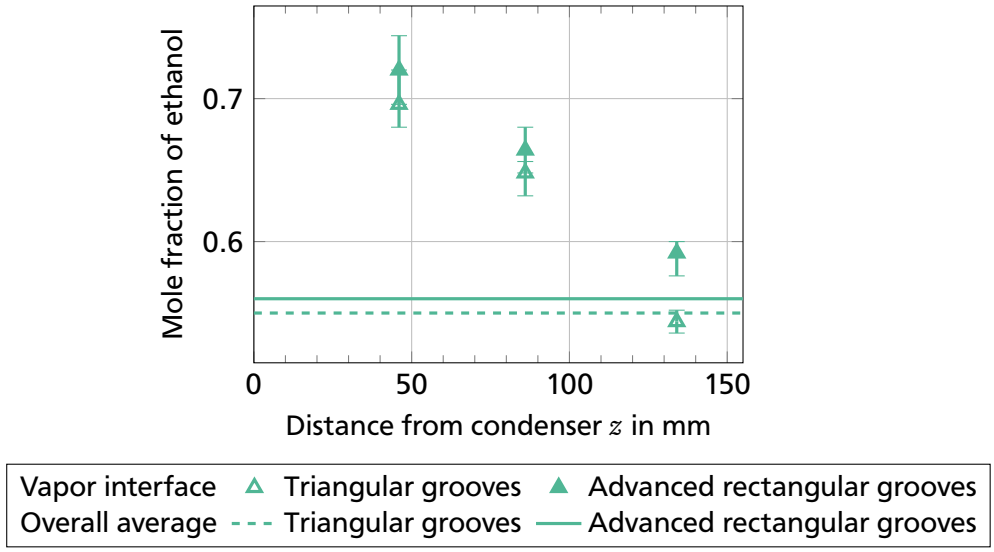

Figure 5.24: Vapor ethanol mole fractions at the interface calculated from vapor temperature measurements over the length of the system for an overall average ethanol mole fraction of $\widetilde{x}_{\mathrm{E,OA}} = 0.55$ to $\widetilde{x}_{\mathrm{E,OA}} = 0.56$, a heat flux of $\dot{q}_{\mathrm{ev}} = 4000\,\mathrm{W\,m^{-2}}$, and an inclination angle of $\beta = 0°$ for the triangular groove structure and the advanced rectangular groove structure

For the overall average ethanol mole fraction $\widetilde{x}_{\mathrm{E,OA}} = 0.71/0.73$, the distributions of the vapor interface ethanol mole fractions intersect with each other. This can be observed in Figure 5.25. The interface ethanol mole fraction is higher for the advanced triangular groove structure than for the triangular groove structure in the evaporator. This trend is inverted at the other two axial positions. For both capillary structures, the vapor interface ethanol mole fraction is clearly below the overall average ethanol mole fraction in the evaporator. For the triangular groove structure, the vapor interface ethanol mole fraction is considerably higher than the overall average ethanol mole fraction at the other two axial positions. For the advanced rectangular groove structure, it is only higher than the overall average ethanol mole fraction at the position closest to the condenser. The difference between the ethanol fraction in the distilled sample at the condenser and the overall average ethanol mole fraction is higher for the triangular groove structure than for the advanced triangular groove structure for this overall average composition (0.06 to 0.02). The measured pressure is considerably lower for the advanced rectangular groove structure in this case.

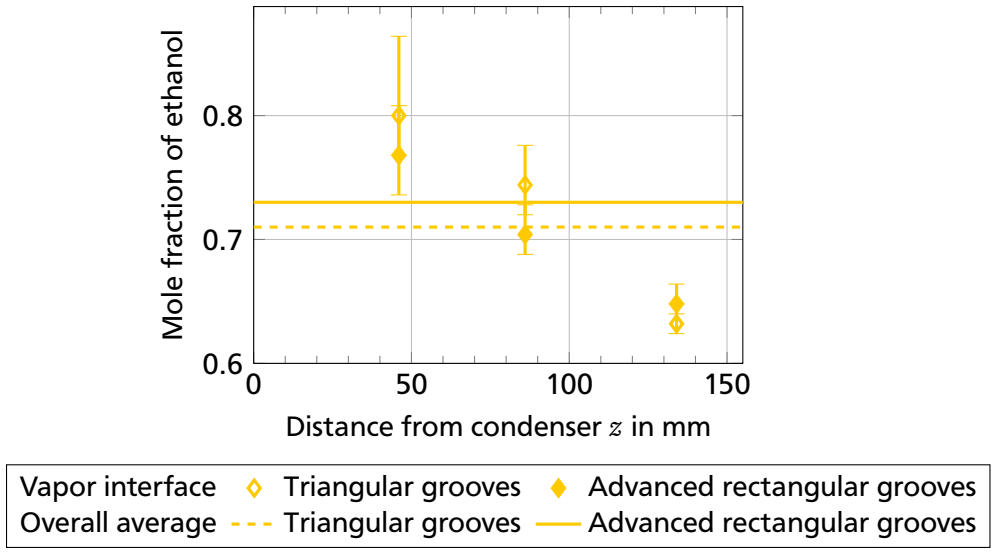

Figure 5.25: Vapor ethanol mole fractions at the interface calculated from vapor temperature measurements over the length of the system for an overall average ethanol mole fraction of $\widetilde{x}_{\mathrm{E,OA}} = 0.71$ to $\widetilde{x}_{\mathrm{E,OA}} = 0.73$, a heat flux of $\dot{q}_{\mathrm{ev}} = 4000\,\mathrm{W\,m^{-2}}$, and an inclination angle of $\beta = 0°$ for the triangular groove structure and the advanced rectangular groove structure

Discussion of the Influence of the Capillary Structure

For the advanced rectangular groove structure, the curvatures at the liquid-vapor interface were not measured. The temperature shifts in different directions make the quantitative comparison of the wall temperatures between both structures challenging. Nevertheless, the wall temperatures for the experiments with $\widetilde{x}_{\mathrm{E,OA}} = 0.55/0.56$ show lower temperature differences between the evaporator and the condenser for the advanced capillary structure. This suggests that the advanced rectangular groove structure facilitates evaporation and, consequently, the axial heat conduction is reduced compared to the triangular groove structure. The results on the mixture separation vary depending on the overall average fluid composition. Differences can also be observed in the calculated vapor interface ethanol mole fractions for both capillary structures. Additionally, the measured pressures differ between the

capillary structures. For the lower overall average ethanol mole fraction, the pressure is higher for the advanced rectangular groove structure. For the higher overall average ethanol mole fraction, the pressure is lower for the advanced rectangular groove structure. Thus, no clear conclusion can be drawn about which capillary structure propagates separation of the mixture. A reason for this could be the pressure variation between the different experiments. For the ethanol mole fraction $\widetilde{x}_{\mathrm{E,OA}} = 0.55/0.56$ the pressure is considerably higher for the experiment with the advanced rectangular groove structure, which is in contrast to the pressures measured for $\widetilde{x}_{\mathrm{E,OA}} = 0.71/0.73$. This could influence the transport processes in the system and, especially, the vapor diffusion coefficients.

5.4 Conclusions

In the experimental investigations, the influence of different operating parameters on the measured variables was evaluated. For lower overall average fractions of ethanol and for lower heat fluxes, the difference between the distilled condenser sample and the overall average ethanol mole fraction increases. When varying the overall average fluid composition and the heat flux, the axial mass flow rate changes. For lower flow rates, the mass transfer processes perpendicular to the main flow direction have a higher relative impact. This may promote a better separation. For both a decreasing overall average ethanol fraction and a decreasing heat flux, the axial flow rates decrease. For the varied fluid composition, the separation can additionally be influenced by the vapor-liquid equilibrium. Because of the different surface tensions of water and ethanol, the separation of the mixture strongly influences the curvature distributions. Additionally, a pullback of the liquid towards the bottom of the capillary structure is observed for some sets of parameters. This pullback can especially be seen when the system gets closer to its limits. These limits are low overall average fractions of ethanol, which lead to a decreased wetting performance, relatively high heat fluxes and relatively high inclinations with the evaporator above the condenser. To draw conclusions on the influence of the curvature change on the process, the underlying mass transfer phenomena need to be further understood. The varied inclination mainly influences the hydrodynamics and thus the curvature of the liquid-vapor interface. The increasing separation with decreasing inclination angle might therefore be caused by changing mass transfer processes because of the relatively strong curvature changes towards the evaporator. The relations of the compositions at the interface compared to the local mean compositions at the corresponding axial positions vary. This was shown with the distribution of the vapor interface ethanol mole fractions in the system. Whereas the interface liquid ethanol fraction is higher than the local average liquid ethanol fraction for some sets of parameters, the opposite is true for other parameters. In many cases, a higher separation was achieved when the vapor interface ethanol fraction at the evaporator was equal to or even lower than the overall average ethanol mole fraction. One parameter, which was not pointedly varied during the scope of these experiments, is the pressure. In the vapor phase, the diffusion coefficient can vary considerably with changing pressure. Due to the control of the wall temperature furthest from the condenser, the pressure resulting in the system is different for every set of parameters. The comparison of the capillary structures shows that general statements on the influence of the capillary structure on the separation cannot be made with the gathered data.

A quantification of the separation efficiency with the McCabe-Thiele method is not conducted for the experiments in this work. As described above, no profound conclusions on the local mean composition

of the liquid at each axial position can be drawn from the evaluated interface compositions. Thus, the McCabe-Thiele method cannot be applied.

CHAPTER 6

Model of Zero-Gravity Distillation

In this chapter, a theoretical-numerical model of the transport processes in zero-gravity distillation columns with channel-shaped capillary structures is developed. Hydrodynamics, heat transfer, and mass transfer are coupled in the model. In contrast to existing models, the influence of the channel geometry with non-constant area of flow is taken into account. The distributions of the capillary pressure, the curvature radii at the liquid-vapor interface, the fluid composition, and the wall temperature are determined. Micro region heat transfer is included in the model in case of evaporation. In the following sections, the modeling approach and the derivation of the model equations are described.

6.1 Modeling Approach

In the described model, zero-gravity distillation is investigated in a closed system at infinite reflux and in a steady-state condition. The governing equations for transport processes in the vapor, liquid, and solid phases are formulated separately and coupled with each other. The influence of the geometry in every cross section is described through geometric factors. With this approach, the resulting differential equations for the curvature, the wall temperature, and the component concentrations can be formulated dependent only on the axial coordinate z. A schematic of the modeled system with the coordinate system used is shown in Figure 6.1.

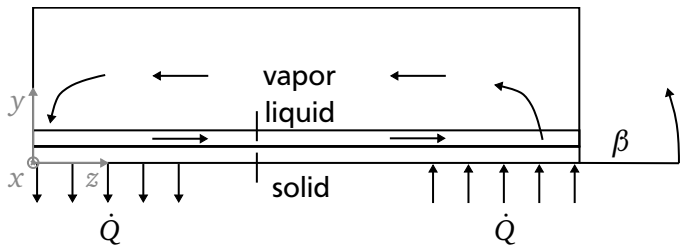

Figure 6.1: Schematic of the modeled system

The heat flow $\dot{Q}$ is supplied to the solid walls of the capillary structure in the evaporator and withdrawn from the solid walls of the capillary structure in the condenser. The boundaries to the left and right of the

system are assumed to be adiabatic. In a cylindric zero-gravity distillation column, the upper boundary of the system is a symmetric boundary. In a flat system, the upper boundary is an adiabatic system wall.

In order to evaluate the transport processes in the system, the governing equations are developed in the following sections. As introduced in Section 2.2.1, the dimensionless numbers characterizing the system are evaluated in different coordinate directions to deduce the model assumptions. These assumptions are:

- In the liquid flow, viscous forces outweigh inertial forces (creeping flow, $Re_{x,\mathrm{L}} \ll 1$, $Re_{y,\mathrm{L}} \ll 1$, and $Re_{z,\mathrm{L}} \ll 1$). For similar systems, this assumption was already used by Brandt *et al.* [10] and Crößmann [14].

- The axially conducted heat in the walls of the capillary structure significantly exceeds the axial heat transport by convection and conduction in the liquid phase. For metallic solids, the thermal conductivity is usually several orders of magnitude higher than for liquids (compare [82]). Thus, for similar dimensions of the liquid cross section area and the wall cross section area and similar temperature gradients, the axially conducted heat in the walls outweighs the conducted heat in the liquid phase. The Prandtl number for alcohols like ethanol is of the order of magnitude of $O\left(10^{1}\right)$ at ambient temperature (compare [82]). Assuming Reynolds numbers of $O\left(10^{-1}\right)$ (creeping flows) the Péclet number for heat transfer is of the order of magnitude of $O\left(1\right)$. Thus, axial heat conduction and convection are of similar magnitude in the liquid phase. For this reason, axial heat conduction in the liquid phase is neglected, as well.

- Perpendicular to the main flow direction, heat transfer through conduction dominates over convective heat transfer in the liquid phase ($Pe_{x,\mathrm{L}} \ll 1$ and $Pe_{y,\mathrm{L}} \ll 1$). As shown before, heat conduction and convection are of similar magnitude in the liquid phase in main flow direction z. Since the velocities perpendicular to the main flow direction are much smaller, heat conduction dominates in this direction.

- In the main flow direction, convective mass transfer dominates over diffusive mass transfer in the liquid phase and in the vapor phase ($Pe'_{z,\mathrm{L}} \gg 1$ and $Pe'_{z,\mathrm{V}} \gg 1$). In the liquid phase, the Schmidt numbers are expected to be much higher than unity due to the small diffusion coefficients. Thus, Péclet numbers much larger than one can be reached even for creeping flows. In the vapor phase, the Reynolds numbers are expected to be much higher than in the liquid phase. Thus, Péclet numbers much larger than one can be reached despite the anticipated lower Schmidt numbers in the vapor phase. This assumption is in accordance with the models of Tschernjaew *et al.* [80] and Seok and Hwang [68].

- Perpendicular to the main flow direction, mass transfer through diffusion dominates over convective mass transfer in the liquid phase and in the vapor phase ($Pe'_{x,\mathrm{L}} \ll 1$, $Pe'_{y,\mathrm{L}} \ll 1$, $Pe'_{x,\mathrm{V}} \ll 1$, and $Pe'_{y,\mathrm{V}} \ll 1$). This assumption is in accordance with most of the previous models for zero-gravity distillation ([56, 57, 68, 80]). The only model also including convection is the one of Ramirez-Gonzalez *et al.* [53]. In their model, empirical correlations for the mass transfer coefficients are used.

6.2 Hydrodynamics

The hydrodynamics in the system is described in a similar way as in the works of Brandt *et al.* [10] and Crößmann [14] for heat pipes and heat pipe evaporators, respectively. First, the mass balance is formulated for the system, which is schematically depicted as a portion of a re-entrant channel with the length $\mathrm{d}z$ (Figure 6.2). The liquid phase and the vapor phase flow counter currently. The mass flow is equal to zero at the boundaries of the system and the phase change mass flow leaving the liquid phase must enter the vapor phase in every section. Thus, the axial mass flows in the vapor and in the liquid phase are the same. For both phases the mass balance can be written as

$$\dot{M}_z - \dot{M}_{z+\mathrm{d}z} = \mathrm{d}\dot{M}_{\mathrm{PC}}, \tag{6.1}$$

where $\dot{M}_z$ and $\dot{M}_{z+\mathrm{d}z}$ are the axial mass flows and $\mathrm{d}\dot{M}_{\mathrm{PC}}$ is the phase change mass flow. The axial mass flow is

$$\dot{M}_z = \overline{w}\,\rho\,A, \tag{6.2}$$

where $\overline{w}$ is the mean flow velocity and A is the area of flow. Using only the linear term of a Taylor series for $\dot{M}_z$, the difference between the axial mass flows $\dot{M}_z$ and $\dot{M}_{z+\mathrm{d}z}$ is

$$\dot{M}_z - \dot{M}_{z+\mathrm{d}z} = -\frac{\mathrm{d}\dot{M}_z}{\mathrm{d}z}\,\mathrm{d}z = -\frac{\mathrm{d}\left(\overline{w}\,\rho\,A\right)}{\mathrm{d}z}\,\mathrm{d}z. \tag{6.3}$$

Thus, the mass balance is

$$-\frac{\mathrm{d}\left(\overline{w}\,\rho\,A\right)}{\mathrm{d}z} = \frac{\mathrm{d}\dot{M}_{\mathrm{PC}}}{\mathrm{d}z}. \tag{6.4}$$

The Navier-Stokes equation in the main flow direction z for incompressible fluids and steady state is:

$$\rho\left(u\frac{\partial w}{\partial x} + v\frac{\partial w}{\partial y} + w\frac{\partial w}{\partial z}\right) = f_z - \frac{\partial p}{\partial z} + \frac{\partial}{\partial x}\left(\mu\frac{\partial w}{\partial x}\right) + \frac{\partial}{\partial y}\left(\mu\frac{\partial w}{\partial y}\right) + \frac{\partial}{\partial z}\left(\mu\frac{\partial w}{\partial z}\right), \tag{6.5}$$

where u and v are the velocities in the directions x and y and f_z are the body forces in the direction of z. The terms on the left side of Equation 6.5 are the inertial terms. The derivatives of the viscosity multiplied with the derivatives of the main flow velocity w are the viscous terms. As stated previously, inertial forces are neglected in the main flow direction. Pressure gradients perpendicular to the main flow direction are neglected, as well. The body forces and the pressure gradient in the vapor phase are small compared to those in the liquid phase. For this reason, the vapor phase is not considered further. The derivative of the liquid pressure according to the Young-Laplace equation is

$$\frac{\mathrm{d}p_{\mathrm{L}}}{\mathrm{d}z} = -C\,\frac{\mathrm{d}\sigma}{\mathrm{d}z} - \sigma\,\frac{\mathrm{d}C}{\mathrm{d}z}. \tag{6.6}$$

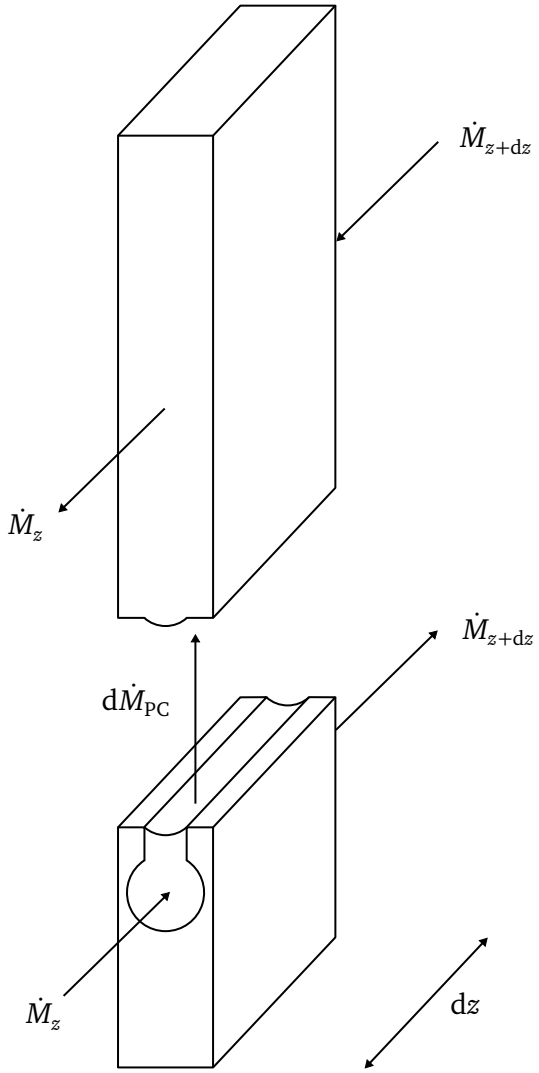

Figure 6.2: Mass balances in the liquid and in the vapor phase

In contrast to the models developed by Brandt *et al.* [10] and Crößmann [14] for one-component systems, the change in surface tension along the main flow axis is taken into account. The body forces in z-direction are gravitational forces, which are dependent on the inclination angle of the system β according to

$$f_z = \rho_{\mathrm{L}}\, g \sin\beta, \tag{6.7}$$

with the gravitational acceleration g. The viscosity of the liquid is assumed to be constant in every cross section. The viscous forces in axial direction are assumed to be much smaller than in every cross section

$$\left|\frac{\partial^2 w_{\mathrm{L}}}{\partial z^2}\right| \ll \left|\frac{\partial^2 w_{\mathrm{L}}}{\partial x^2}\right|, \tag{6.8}$$

$$\left|\frac{\partial^2 w_{\mathrm{L}}}{\partial z^2}\right| \ll \left|\frac{\partial^2 w_{\mathrm{L}}}{\partial y^2}\right|. \tag{6.9}$$

Therefore, the term $\frac{\partial^2 w_\mathrm{L}}{\partial z^2}$ is neglected. Inserting Equations 6.6 and 6.7 and considering Equations 6.8 and 6.9, the simplified Navier-Stokes equation can be rearranged, which leads to

$$\frac{\mathrm{d}C}{\mathrm{d}z} = -\frac{\rho_\mathrm{L}}{\sigma} g \sin\beta - \frac{C}{\sigma}\frac{\mathrm{d}\sigma}{\mathrm{d}z} - \frac{\mu_\mathrm{L}}{\sigma}\left(\frac{\partial^2 w_\mathrm{L}}{\partial x^2} + \frac{\partial^2 w_\mathrm{L}}{\partial y^2}\right). \tag{6.10}$$

In accordance with Xu and Carey [86], the influence of the viscous forces in every cross section can be replaced by a term dependent on the Fanning friction factor f_F, the Reynolds number $Re_{z,\mathrm{L}}$, the mean flow velocity $\overline{w}_\mathrm{L}$, and the hydraulic diameter d_H of the channel

$$\frac{\partial^2 w_\mathrm{L}}{\partial x^2} + \frac{\partial^2 w_\mathrm{L}}{\partial y^2} = 2 f_\mathrm{F} Re_{z,\mathrm{L}} \frac{\overline{w}_\mathrm{L}}{d_\mathrm{H}^2}. \tag{6.11}$$

According to Damean and Regtien [15], the Fanning friction factor f_F is the ratio of the Poiseuille number Po to the Reynolds number $Re_{z,\mathrm{L}}$

$$f_\mathrm{F} = \frac{Po}{Re_{z,\mathrm{L}}}. \tag{6.12}$$

The Poiseuille number is only dependent on the geometry and describes the influence of the cross section geometry on the pressure losses of the flow due to friction. It only has to be calculated once for the geometry. Thus, the calculation of the Poiseuille number simplifies the calculation of the curvature over z. Inserting Equation 6.12 into Equation 6.13 leads to the equation

$$\frac{\partial^2 w_\mathrm{L}}{\partial x^2} + \frac{\partial^2 w_\mathrm{L}}{\partial y^2} = 2 Po \frac{\overline{w}_\mathrm{L}}{d_\mathrm{H}^2}. \tag{6.13}$$

In this work, Equation 6.13 is solved with a finite element method. For a prescribed source term on the right side of Equation 6.13, the mean axial velocity $\overline{w}_\mathrm{L}$ can be evaluated as a result of the simulation. With the prescribed source term and the hydraulic diameter d_H, the Poiseuille number can be calculated. The boundary conditions for the simulation are shown in Figure 6.3 for half of a re-entrant channel. The velocity at the channel wall is set equal to zero. At the middle plane of the channel, the derivative of the velocity in normal direction is equal to zero due to the channel symmetry. At the interface, the shear forces imposed by the vapor and Marangoni flows are neglected. Based on this assumption, the boundary condition at the liquid-vapor interface is a zero-gradient condition.

With the Poiseuille number, the overall differential equation for the curvature is given by

$$\frac{\mathrm{d}C}{\mathrm{d}z} = -\frac{\rho_\mathrm{L}}{\sigma} g \sin\beta - \frac{C}{\sigma}\frac{\mathrm{d}\sigma}{\mathrm{d}z} - 2\frac{\mu_\mathrm{L}}{\sigma} Po \frac{\overline{w}_\mathrm{L}}{d_\mathrm{H}^2}. \tag{6.14}$$

The curvature radius of the liquid-vapor interface can be evaluated as the inverse value of the curvature C. The first summand on the right side represents the curvature change due to gravity, the second summand

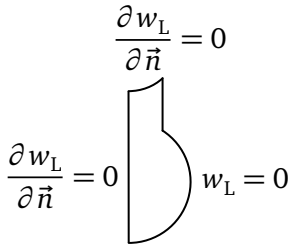

Figure 6.3: Boundary conditions for the solution of the two-dimensional Poisson equation for the main flow velocity w_L at a re-entrant channel geometry

represents the curvature change due to a change in composition and the third summand describes the curvature change due to friction.

6.3 Heat Transfer

Ideally, conjugate heat transfer should be described in the solid, liquid, and vapor phase, taking into account conduction, convection, and phase change. However, this task is very complex. With the assumptions above, the problem can be simplified. For the solid phase, axial heat transfer is important while it is negligible for the liquid phase. In the liquid phase, heat transfer perpendicular to the main flow direction is significant. Thus, heat transfer in the liquid and solid phase can be treated separately. Heat transport in the vapor phase is neglected. The differential equation for the wall temperature distribution is derived from the energy balance in the wall of the capillary structure. The solid wall exchanges heat with the liquid phase. Heat transfer in the liquid phase can be distinguished in micro region heat transfer and macroscopic heat transfer. The coupling of these transport processes with the energy balance of the wall is described in the following section.

A schematic of the energy balance of the metal plate for half the channel width $\frac{W}{2}$ over a length $\mathrm{d}z$ is shown in Figure 6.4. The schematic displays a section in the evaporator of the system. In the evaporator, a heat flux $\dot{q}_{\mathrm{BF}}$ is supplied to the metal plate from the bottom ($\dot{q}_{\mathrm{BF}} > 0$). In the condenser, heat is withdrawn from the metal plate from the bottom ($\dot{q}_{\mathrm{BF}} < 0$). In the adiabatic zone, $\dot{q}_{\mathrm{BF}}$ is equal to zero. The heat flow $\mathrm{d}\dot{Q}_{\mathrm{mac}}$ is transferred from the wall through the macroscopic liquid meniscus towards the liquid-vapor interface. Additionally, the heat flow $\mathrm{d}\dot{Q}_{\mathrm{mic}}$ is transferred through the micro region towards the liquid-vapor interface. At $x = \frac{W}{2}$, the wall is adiabatic with respect to symmetry. Heat is axially conducted through the walls of the capillary structure. The axial heat flow $\dot{Q}_z$ enters the system, while the axial heat flow $\dot{Q}_{z+\mathrm{d}z}$ leaves the system. At $x = 0$, the system boundary is thermally insulated.

The energy balance for the depicted section of the wall can be formulated as

$$\dot{Q}_z - \dot{Q}_{z+\mathrm{d}z} = \mathrm{d}\dot{Q}_{\mathrm{mac}} + \mathrm{d}\dot{Q}_{\mathrm{mic}} - \dot{q}_{\mathrm{BF}} \frac{W}{2} \mathrm{d}z. \tag{6.15}$$

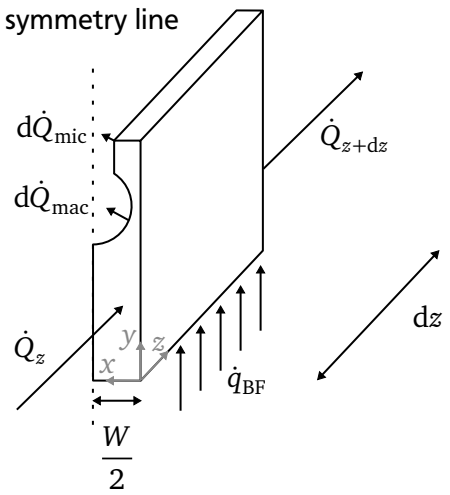

Figure 6.4: Energy balance of the wall of the capillary structure

Based on the assumption that all the heat transferred between the solid and the liquid is consumed by phase change at the same axial position, the overall phase change heat flow $d\dot{Q}_{PC}$ is

$$d\dot{Q}_{PC} = d\dot{Q}_{mac} + d\dot{Q}_{mic}. \tag{6.16}$$

Assuming a metallic solid, the thermal resistance of the plate is small. For the investigated zero-gravity distillation systems thus far, the axial length of the metal plate is much larger than the length scales in every cross section. Thus, it is assumed that the wall temperature is approximately uniform in every cross section and the heat conduction in the solid phase is one-dimensional. These assumptions are similar to the thin fin approximation for a constant wall cross section [69]. With Fourier's law, the axially conducted heat flow can be described through

$$\dot{Q}_z = -\lambda_S \frac{1}{2} A_S \frac{dT_S}{dz}, \tag{6.17}$$

with the thermal conductivity of the solid λ_S and the constant area of the channel wall A_S. Using only the linear term of a Taylor series for $\dot{Q}_z$ and inserting Equation 6.17, the difference between the axially conducted heat flows $\dot{Q}_z$ and $\dot{Q}_{z+dz}$ is given by

$$\dot{Q}_z - \dot{Q}_{z+dz} = -\frac{d\dot{Q}_z}{dz} dz = \lambda_S \frac{1}{2} A_S \frac{d^2 T_S}{dz^2} dz. \tag{6.18}$$

Inserting Equation 6.18 in Equation 6.15 and rearranging the resulting equation leads to the differential equation for the wall temperature

$$\frac{d^2 T_S}{dz^2} = \frac{2}{\lambda_S A_S} \frac{d\dot{Q}_{mac}}{dz} + \frac{2}{\lambda_S A_S} \frac{d\dot{Q}_{mic}}{dz} - \frac{\dot{q}_{BF} W}{\lambda_S A_S}. \tag{6.19}$$

The macroscopic heat flow $d\dot{Q}_{mac}$ and the micro region heat flow $d\dot{Q}_{mic}$ still need to be described. Due to the small length scales of the micro region, intermolecular forces and the thermal resistance of the liquid-vapor interface need to be taken into account in the micro region. Therefore, the macroscopic heat flow and the micro region heat flow need to be treated separately. If the micro-region heat transfer were not taken into account, the determined evaporative heat and mass flows would be less accurate. In this work, the distribution of the composition in the micro region is of no further interest. For simplicity, the micro region heat transfer for the mixture is evaluated treating the mixture as a pure fluid with constant weighted averaged properties in this work. For the investigated system in this work, the contact line velocity is equal to zero. A detailed derivation of the micro region model used and an explanation of the solution algorithm can be found in the work of Batzdorf [7]. Micro region heat transfer is only accounted for in the case of evaporation, but not in the case of condensation. The length of the micro region is assumed to be 1 µm. The micro region heat flow can be formulated as the integral heat flow per length in the micro region $\dot{q}_{mic}$ multiplied with the length of the section

$$d\dot{Q}_{mic} = \dot{q}_{mic}\, dz. \tag{6.20}$$

This heat flow is non-linearly dependent on the liquid composition and the temperature difference between the saturation temperature at the interface and the solid. It is calculated separately with the micro region model and fed to the differential equation for the wall temperature depending on the liquid composition and the temperature difference between the interface and the solid.

The heat transferred to the macroscopic liquid meniscus $d\dot{Q}_{mac}$ can be determined by formulating the energy balance of the liquid phase. As stated in Section 6.1, the axial heat transport in the liquid phase is neglected. Under the assumption that conduction in the liquid dominates over convection perpendicular to the main flow direction, the energy balance for the liquid phase can be formulated as a two-dimensional Laplace equation

$$\frac{\partial^2 T_L}{\partial x^2} + \frac{\partial^2 T_L}{\partial y^2} = 0. \tag{6.21}$$

Similar to the procedure described for calculating the Poiseuille number, this two-dimensional equation can be solved with a finite element method to derive a geometric factor, which describes the influence of the channel geometry and the interface shape on the macroscopic heat transport. A sketch of the boundary conditions of the two-dimensional Laplace equation is shown in Figure 6.5. For simplicity, a uniform temperature T_{int} at the liquid-vapor interface is assumed, which is the saturation temperature corresponding to the local liquid composition. The micro region is implemented as a circular section of the meniscus with a radius of 1 µm from the contact line position. Since heat conduction in the micro-region is commonly assumed to be one-dimensional normal to the interface, the system is isolated to the micro region as shown in the magnifying glass. The liquid is also isolated to the channel center line due to symmetry. At the wall, a uniform temperature T_S is assigned in accordance with the assumption of a constant wall temperature in every cross section. Γ is the coordinate along the liquid-vapor interface.

The heat flow conducted through the macroscopic meniscus is linearly dependent on the temperature difference between the channel wall and the liquid-vapor interface. The geometric factor φ can therefore

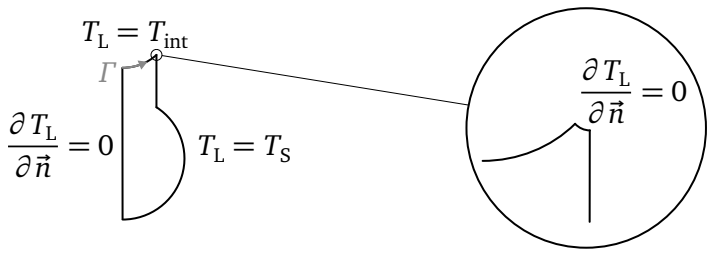

Figure 6.5: Boundary conditions of the two-dimensional energy balance in the liquid phase

be defined as the ratio of the heat flow conducted through the macroscopic meniscus divided by the thermal conductivity of the liquid multiplied with the temperature difference between the channel wall and the interface

$$\varphi = \frac{\int_0^{\Gamma_{tot}} \frac{dT_L}{d\vec{n}} d\Gamma}{T_S - T_{int}} \tag{6.22}$$

where Γ_{tot} is the total length of the interface. The factor φ can be interpreted as a conductive transport coefficient of the macroscopic meniscus. The macroscopic heat transfer can then be written as

$$d\dot{Q}_{mac} = \lambda_L \varphi \, (T_S - T_{int}) \, dz. \tag{6.23}$$

Inserting Equations 6.20 and 6.23 in Equation 6.19 leads to the differential equation for the wall temperature

$$\frac{d^2 T_S}{dz^2} = 2 \frac{\lambda_L}{\lambda_S A_S} \varphi \, (T_S - T_{int}) - \frac{\dot{q}_{BF} W}{\lambda_S A_S} + 2 \frac{\dot{q}_{mic}}{\lambda_S A_S}. \tag{6.24}$$

6.4 Mass Transfer

With component balances, separate equations for the concentrations of the two components in the liquid and in the vapor phase can be derived. The procedure is similar for the vapor phase and for the liquid phase. In Figure 6.6, the component balances in the liquid phase and in the vapor phase are shown for a component i. Vapor and liquid flow counter currently. The axial molar flow $\dot{N}_{z,i}$ changes due to evaporation (or condensation). The rate of phase change molar flow is denoted by $d\dot{N}_{i,PC}$. The flow leaving the liquid phase enters the vapor phase.

The component balance over the length dz for the liquid and for the vapor phase is therefore

$$\dot{N}_{z,i} - \dot{N}_{z+dz,i} = d\dot{N}_{i,PC}. \tag{6.25}$$

Neglecting diffusive flows in axial direction, the axial flow $\dot{N}_{z,i}$ is

$$\dot{N}_{z,i} = \overline{w}\, \overline{c}_i A, \tag{6.26}$$

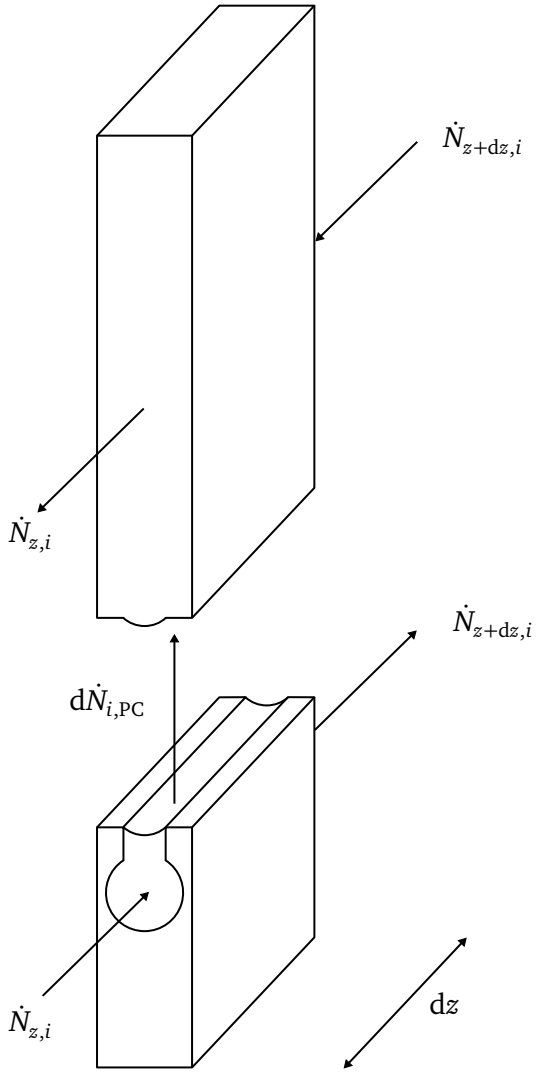

Figure 6.6: Component balances in the liquid and in the vapor phase

with the axial mean concentration of component i $\overline{c}_i$. Since axial diffusion is neglected, the component velocities are the same for both components. Thus, no distinction between mass averaged and molar averaged velocities has to be made and the mean flow velocity $\overline{w}$ is the same as in the mass balances. Using only the linear term of a Taylor series for $\dot{N}_{z,i}$, the difference in axial flows is given through

$$\dot{N}_{z,i} - \dot{N}_{z+\mathrm{d}z,i} = -\frac{\mathrm{d}\dot{N}_{z,i}}{\mathrm{d}z}\,\mathrm{d}z = -\frac{\mathrm{d}\left(\overline{w}\,\overline{c}_i A\right)}{\mathrm{d}z}\,\mathrm{d}z. \tag{6.27}$$

Inserting Equation 6.27 in Equation 6.25 leads to the differential equation for the mean concentration of component i

$$\frac{\mathrm{d}\left(\overline{w}\,\overline{c}_i A\right)}{\mathrm{d}z} + \frac{\mathrm{d}\dot{N}_{i,\mathrm{PC}}}{\mathrm{d}z} = 0. \tag{6.28}$$

The phase change flow of component i $\mathrm{d}\dot{N}_{i,\mathrm{PC}}$ in every cross section needs to be determined. It is assumed that diffusion is the only transport process perpendicular to the main flow direction. Thus, the convection-diffusion equation reduces to

$$D\left(\frac{\partial^2 c_i}{\partial x^2}+\frac{\partial^2 c_i}{\partial y^2}\right)=s_c \tag{6.29}$$

in every cross section. Here, s_c is a source term, which accounts for the convective mass transport in axial direction. For simplification, this source term is assumed to be constant. In reality, s_c is not constant, but is dependent on the distribution of the axial flow velocity. Equation 6.29 is a two-dimensional Poisson equation and is solved with a finite element method for the liquid and for the vapor phase. The boundary conditions of the two systems are depicted in Figure 6.7. In the vapor phase, zero-gradient conditions account for symmetry and system boundaries at all boundaries except the liquid-vapor interface. Here, a constant interface concentration is prescribed. At the wall of the liquid channel, a zero-gradient condition is applied. The same boundary condition is applied in the middle of the channel with respect to symmetry. At the interface, a constant liquid interface concentration is prescribed.

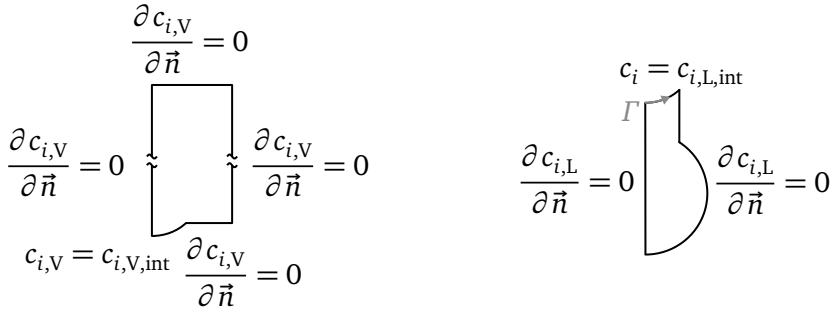

(a) Vapor phase **(b)** Liquid phase

Figure 6.7: Boundary conditions of the two-dimensional component balances in the vapor phase and in the liquid phase

Considering the liquid phase, the diffusive flow per axial length over the interface is

$$\frac{\mathrm{d}\dot{N}_{i,\mathrm{PC}}}{\mathrm{d}z}=-2\,D_{\mathrm{L}}\int_0^{\Gamma_{\mathrm{tot}}}\frac{\mathrm{d}c_{i,\mathrm{L}}}{\mathrm{d}\vec{n}}\mathrm{d}\Gamma, \tag{6.30}$$

since $\mathrm{d}\dot{N}_{i,\mathrm{PC}}$ is defined as positive for a negative concentration gradient in normal direction at the interface in the liquid phase. The factor two accounts for the fact that only half the channel is evaluated in the two-dimensional model. This flow is proportional to the difference between the mean concentration in the channel $\overline{c}_{i,\mathrm{L}}$ and the interface concentration $c_{i,\mathrm{L,int}}$

$$\frac{\mathrm{d}\dot{N}_{i,\mathrm{PC}}}{\mathrm{d}z}=2\,D_{\mathrm{L}}\,\psi_{\mathrm{L}}\left(\overline{c}_{i,\mathrm{L}}-c_{i,\mathrm{L,int}}\right), \tag{6.31}$$

with the proportionality factor ψ_L. Considering the vapor phase, the diffusive flow per axial length over the interface is

$$\frac{\mathrm{d}\dot{N}_{i,\mathrm{PC}}}{\mathrm{d}z} = 2\,D_\mathrm{V} \int_0^{\Gamma_\mathrm{tot}} \frac{\mathrm{d}c_{i,\mathrm{V}}}{\mathrm{d}\vec{n}} \mathrm{d}\Gamma, \tag{6.32}$$

since $\mathrm{d}\dot{N}_{i,\mathrm{PC}}$ is defined as positive for a positive concentration gradient at the interface in the vapor phase. This flow is proportional to the difference between the mean concentration in the vapor phase $\overline{c}_{i,\mathrm{V}}$ and the interface concentration in the vapor phase $c_{i,\mathrm{V,int}}$

$$\frac{\mathrm{d}\dot{N}_{i,\mathrm{PC}}}{\mathrm{d}z} = -2\,D_\mathrm{V}\,\psi_\mathrm{V}\left(\overline{c}_{i,\mathrm{V}} - c_{i,\mathrm{V,int}}\right), \tag{6.33}$$

with the proportionality factor ψ_V. ψ can then be calculated by equaling Equations 6.30 and 6.31 and Equations 6.32 and 6.33 and rearranging for ψ through

$$\psi = \frac{-\int_0^{\Gamma_\mathrm{tot}} \frac{\mathrm{d}c_i}{\mathrm{d}\vec{n}} \mathrm{d}\Gamma}{\overline{c}_i - c_{i,\mathrm{int}}}. \tag{6.34}$$

ψ can be interpreted as a diffusive transport coefficient perpendicular to the main flow direction. It is only dependent on the channel geometry and the interface curvature. Inserting Equation 6.31 in Equation 6.28, the differential equation for the liquid phase concentration of component i is

$$\frac{\mathrm{d}\left(\overline{w}_\mathrm{L}\,\overline{c}_{i,\mathrm{L}} A_\mathrm{L}\right)}{\mathrm{d}z} + 2\,D_\mathrm{L}\,\psi_\mathrm{L}\left(\overline{c}_{i,\mathrm{L}} - c_{i,\mathrm{L,int}}\right) = 0. \tag{6.35}$$

Inserting Equation 6.33 in Equation 6.28, the differential equation for the concentration of component i in the vapor phase is

$$\frac{\mathrm{d}\left(\overline{w}_\mathrm{V}\,\overline{c}_{i,\mathrm{V}} A_\mathrm{V}\right)}{\mathrm{d}z} - 2\,D_\mathrm{V}\,\psi_\mathrm{V}\left(\overline{c}_{i,\mathrm{V}} - c_{i,\mathrm{V,int}}\right) = 0. \tag{6.36}$$

From the concentrations of the components, the overall mean concentrations or the overall concentrations at the interface in the two phases can be calculated as the sum of the two component concentrations

$$c = c_\mathrm{A} + c_\mathrm{B}. \tag{6.37}$$

The mole fractions in the liquid phase $\widetilde{x}_i$ and in the vapor phase $\widetilde{y}_i$ can then be calculated according to

$$\widetilde{x}_i = \frac{c_{i,\mathrm{L}}}{c_\mathrm{L}} \tag{6.38}$$

and

$$\widetilde{y}_i = \frac{c_{i,\mathrm{V}}}{c_{\mathrm{V}}}. \tag{6.39}$$

As stated in Section 6.2, the axial mass flows in the liquid and vapor phase are the same. Since no reactions occur in the system, the same holds true for the total axial molar flows and the axial molar flows of both components in the liquid and vapor phase. Together with the negligence of axial diffusion it follows that the mean mole fractions of the components in the liquid phase $\overline{\widetilde{x}}_i$ and in the vapor phase $\overline{\widetilde{y}}_i$ must be equal to each other at every axial position in the system. A detailed derivation of this equality is given in Appendix B.1.

6.5 Coupling of Differential Equations

Altogether, six ordinary differential equations and one coupling equation describe the process. The differential equations are the mass balances in the liquid and in the vapor phase (Equation 6.4), the component balances in the liquid and vapor phase for component A (Equations 6.35 and 6.36), and the differential equations for the curvature (Equation 6.14) and the wall temperature (Equation 6.24). In the overall mass balances, the phase change mass flow $\mathrm{d}\dot{M}_{\mathrm{PC}}$ can be formulated as the sum of the phase change molar flows $\mathrm{d}\dot{N}_{i,\mathrm{PC}}$ in both phases multiplied with the molar masses $\widetilde{M}_i$. The phase change molar flows in the liquid and vapor phase must be equal to each other. Thus, the six differential equations are

$$-\frac{\mathrm{d}\left(\overline{w}_{\mathrm{L}}\,\rho_{\mathrm{L}}\,A_{\mathrm{L}}\right)}{\mathrm{d}z} = 2\,\psi_{\mathrm{L}}\,D_{\mathrm{L}}\left(\overline{c}_{\mathrm{A,L}} - c_{\mathrm{A,L,int}}\right)\widetilde{M}_{\mathrm{A}} + 2\,\psi_{\mathrm{L}}\,D_{\mathrm{L}}\left(\overline{c}_{\mathrm{B,L}} - c_{\mathrm{B,L,int}}\right)\widetilde{M}_{\mathrm{B}}, \tag{6.40}$$

$$-\frac{\mathrm{d}\left(\overline{w}_{\mathrm{V}}\,\rho_{\mathrm{V}}\,A_{\mathrm{V}}\right)}{\mathrm{d}z} = 2\,\psi_{\mathrm{L}}\,D_{\mathrm{L}}\left(\overline{c}_{\mathrm{A,L}} - c_{\mathrm{A,L,int}}\right)\widetilde{M}_{\mathrm{A}} + 2\,\psi_{\mathrm{L}}\,D_{\mathrm{L}}\left(\overline{c}_{\mathrm{B,L}} - c_{\mathrm{B,L,int}}\right)\widetilde{M}_{\mathrm{B}}, \tag{6.41}$$

$$-\frac{\mathrm{d}\left(\overline{w}_{\mathrm{L}}\,\overline{c}_{\mathrm{A,L}}\,A_{\mathrm{L}}\right)}{\mathrm{d}z} = 2\,D_{\mathrm{L}}\,\psi_{\mathrm{L}}\left(\overline{c}_{\mathrm{A,L}} - c_{\mathrm{A,L,int}}\right), \tag{6.42}$$

$$-\frac{\mathrm{d}\left(\overline{w}_{\mathrm{V}}\,\overline{c}_{\mathrm{A,V}}\,A_{\mathrm{V}}\right)}{\mathrm{d}z} = 2\,D_{\mathrm{L}}\,\psi_{\mathrm{L}}\left(\overline{c}_{\mathrm{A,L}} - c_{\mathrm{A,L,int}}\right), \tag{6.43}$$

$$\frac{\mathrm{d}C}{\mathrm{d}z} = -\frac{\rho_{\mathrm{L}}}{\sigma}\,g\sin\beta - \frac{C}{\sigma}\,\frac{\mathrm{d}\sigma}{\mathrm{d}z} - 2\,\frac{\mu_{\mathrm{L}}}{\sigma}\,Po\,\frac{\overline{w}_{\mathrm{L}}}{d_{\mathrm{H}}^2}, \tag{6.44}$$

$$\frac{\mathrm{d}^2 T_{\mathrm{S}}}{\mathrm{d}z^2} = 2\,\frac{\lambda_{\mathrm{L}}}{\lambda_{\mathrm{S}} A_{\mathrm{S}}}\,\varphi\,\left(T_{\mathrm{S}} - T_{\mathrm{int}}\right) - \frac{\dot{q}_{\mathrm{BF}}\,W}{\lambda_{\mathrm{S}} A_{\mathrm{S}}} + 2\,\frac{\dot{q}_{\mathrm{mic}}}{\lambda_{\mathrm{S}} A_{\mathrm{S}}}. \tag{6.45}$$

The differential equations are coupled through the phase change heat flow defined in Equation 6.16. The phase change heat flow over the entire channel is equal to the sum of the phase change molar flows multiplied with the molar enthalpies of evaporation of the components

$$2\left(\lambda_{\mathrm{L}}\,\varphi\,\left(T_{\mathrm{S}}-T_{\mathrm{int}}\right)+\dot{q}_{\mathrm{mic}}\right)=2\,\psi_{\mathrm{L}}\,D_{\mathrm{L}}\left(\overline{c}_{\mathrm{A,L}}-c_{\mathrm{A,L,int}}\right)\Delta\widetilde{h}_{\mathrm{LV,A}}+2\,\psi_{\mathrm{L}}\,D_{\mathrm{L}}\left(\overline{c}_{\mathrm{B,L}}-c_{\mathrm{B,L,int}}\right)\Delta\widetilde{h}_{\mathrm{LV,B}}. \tag{6.46}$$

These seven equations contain seven independent variables, which are the mean axial flow velocities in the liquid and vapor phase $\overline{w}_{\mathrm{L}}$ and $\overline{w}_{\mathrm{V}}$, the curvature C, the mean concentrations of component A in the liquid and in the vapor phase $\overline{c}_{\mathrm{A,L}}$ and $\overline{c}_{\mathrm{A,V}}$, the temperature in the solid wall T_{S}, and the temperature at the interface T_{int}. The mean concentrations of component B are dependent on the mean concentrations of component A (see Appendix B.2). The interface concentrations of components A and B $c_{\mathrm{A,L,int}}$ and $c_{\mathrm{B,L,int}}$ are functions of the interface temperature T_{int} with respect to the vapor-liquid equilibrium. The integral micro region heat flow per length $\dot{q}_{\mathrm{mic}}$ depends on the interface temperature, the temperature of the solid wall, and the interface composition and is calculated with the micro region model. The transport coefficients and areas of flow in the liquid and vapor phase are dependent on the curvature of the liquid-vapor interface. Under the assumption of an ideal mixture, the overall densities in the two phases are calculated according to the mixing rule given in [82]. With the component densities ρ_{A} and ρ_{B} the mixture density is

$$\rho=\left(\frac{\overline{c}_{\mathrm{A}}}{\overline{c}}\,\frac{1}{\rho_{\mathrm{A}}}+\frac{\overline{c}_{\mathrm{B}}}{\overline{c}}\,\frac{1}{\rho_{\mathrm{B}}}\right)^{-1}. \tag{6.47}$$

All other unknowns in the equations are either model parameters or fluid properties.

The boundary conditions of the system with the overall length L_{tot} are:

- The system is adiabatic at the evaporator boundary ($\frac{\mathrm{d}T_{\mathrm{S}}}{\mathrm{d}z}\left(z=L_{\mathrm{tot}}\right)=0$) and a boundary wall temperature is prescribed at $z=L_{\mathrm{tot}}$.
- The velocities in axial direction in the liquid and vapor phase are equal to zero at the evaporator boundary of the system ($\overline{w}_{\mathrm{L}}\left(z=L_{\mathrm{tot}}\right)=0$ and $\overline{w}_{\mathrm{V}}\left(z=L_{\mathrm{tot}}\right)=0$).
- The interface curvature at the evaporator boundary of the system is fixed at $C\left(z=L_{\mathrm{tot}}\right)=850\,\mathrm{m}^{-1}$. This interface curvature is of the same order of magnitude as the curvatures observed in the experiments.
- The values of the mean concentrations in the liquid and in the vapor phase are set to fixed values at the position $z=L_{\mathrm{tot}}$, which are dependent on the evaluated overall average fluid composition.

The system is solved in discrete steps from the evaporator boundary $z=L_{\mathrm{tot}}$ to the condenser boundary $z=0$ for a given pressure, heat flux, and inclination. The boundary conditions for the wall temperature and the component concentrations are varied until a solution is obtained which guarantees an adiabatic system boundary at the condenser boundary and the targeted overall average fluid composition. The mesh independence of the dimensionless parameters Po, φ, ψ_{L}, and ψ_{V} is shown in Appendix B.3.

Chapter 7

Model Results

In this chapter, the results of the simulations based on the theoretical model are presented. The model is applied to a re-entrant channel made of copper. Due to its channel shape, this capillary structure has a higher thermal resistance between the bottom wall and the liquid-vapor interface than the triangular groove structure, which is the focus of the experiments. This leads to lower evaporation rates for the re-entrant channel compared to the triangular groove. For this reason, the re-entrant channel fulfills the model assumption that diffusion is the only mass transfer process perpendicular to the main flow direction better than the triangular groove structure. The length of the system between condenser and evaporator boundary is $L_{\mathrm{tot}} = 150\,\mathrm{mm}$. The length of the condenser L_{co} and the evaporator L_{ev} are set to 50 mm. In Figure 7.1 the geometrical dimensions in one cross section of the evaluated system are depicted.

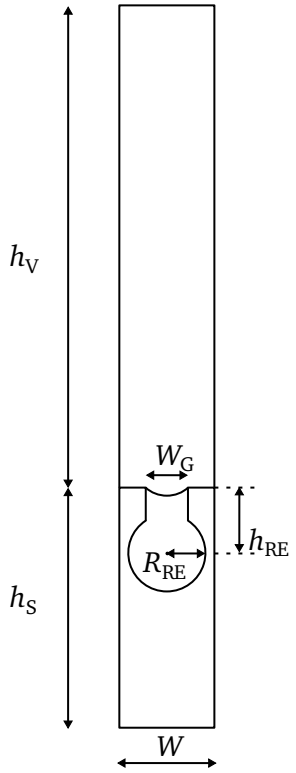

Figure 7.1: Geometrical dimensions in one cross section of the evaluated system

The height of the vapor phase is $h_V = 10\,\text{mm}$ and the height of the solid metal plate is $h_S = 5\,\text{mm}$. The opening width of the re-entrant channel is $W_G = 0.9\,\text{mm}$ and the width of the system is $W = 2\,\text{mm}$. The height of the re-entrant channel from the center of the circular channel to the top is $h_{RE} = 1.4\,\text{mm}$.

The radius of the re-entrant channel R_{RE} is varied within the simulations. The simulation parameters are given in Table 7.1. The pressure is always chosen at $p = 300\,\text{mbar}$. The process is simulated at one averaged fluid composition with three different radii of the circular part of the channel, three different heat fluxes, and three inclination angles of the system. Instead of water-ethanol as in the experiment, ethanol-methanol is chosen as the fluid system in order to avoid the influence of Marangoni flows, which are not accounted for in the model. The simulation with a radius of the re-entrant channel of $R_{RE} = 800\,\mu\text{m}$, a heat flux of $\dot{q} = 3750\,\text{W}\,\text{m}^{-2}$, and an inclination angle of $\beta = 0°$ is referred to as the reference simulation in the following sections.

Table 7.1: Parameters of simulations

Capillary structure	Overall average mole fraction of ethanol $\widetilde{x}_{E,OA}$	Radius of re-entrant channel R_{RE} in µm	Heat flux $\dot{q}$ in $\text{W}\,\text{m}^{-2}$	Inclination angle β in °
re-entrant channel	0.21	650, 800, 950	3500, 3750, 4000	−0.4, 0, 0.4

Firstly, the results for the varied heat flux are shown; afterwards the results for the varied inclination angle and the varied channel radius are presented. The results are always presented with the axial position on the abscissa. The condenser is always at the left end of the diagrams, whereas the evaporator is always at the right end of the diagrams.

7.1 Influence of the Heat Flux

In Figure 7.2, the temperature distributions in the walls and at the interface are shown for the simulations with varied heat fluxes of $3500\,\text{W}\,\text{m}^{-2}$, $3750\,\text{W}\,\text{m}^{-2}$, and $4000\,\text{W}\,\text{m}^{-2}$. For all the heat fluxes, the temperatures in the wall increase from the condenser end to the evaporator end. No clear flattening of the wall temperature can be observed in the adiabatic zone. Counter intuitively, the temperature difference in the wall between the evaporator end and the condenser end of the system decreases with increasing the heat flux. The reason for this is the decreasing molar flow rate for a decreasing heat flux (compare Figure 7.5), which leads to an increasing axially conducted heat flow with decreasing the heat flux. The temperatures at the liquid-vapor interface follow the trend of the wall temperatures. With increasing the heat flux, the absolute value of the maximum temperature difference between wall and interface increases at the evaporator.

In the left part of Figure 7.3, the curvature radius at the liquid-vapor interface is shown over the length of the system. The curvature radius is fixed at the evaporator end of the system due to the same boundary condition for all simulations. The difference between the maximum curvature radius at the condenser boundary and the minimum curvature radius at the evaporator boundary is the highest for the lowest heat flux and decreases with increasing the heat flux. Whereas the curvature radius changes strongly in all simulations from the condenser towards the evaporator, the curvature change strongly decreases in the evaporator. The reason for this can be seen in the right diagram of Figure 7.3. Here, the influence

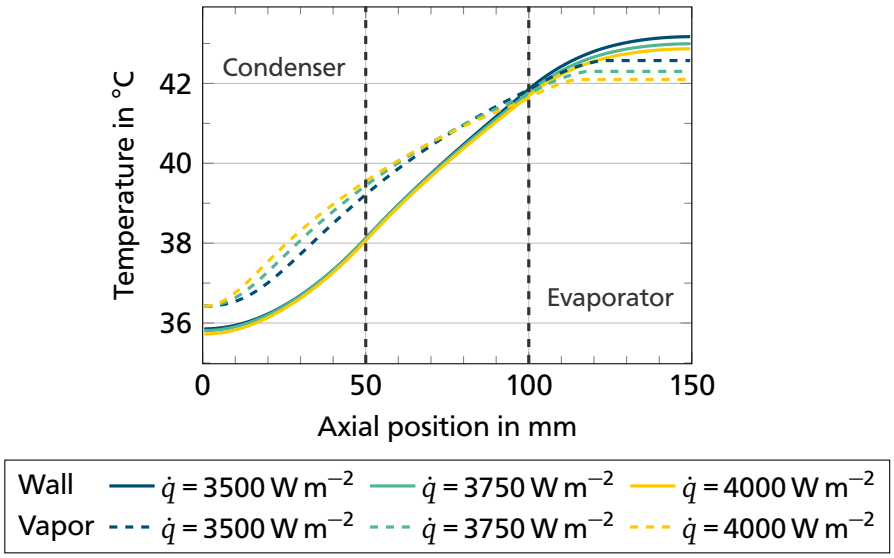

Figure 7.2: Temperature distributions in the wall and at the liquid-vapor interface over the length of the re-entrant channel for an overall average ethanol mole fraction of $\widetilde{x}_{\mathrm{E,OA}} = 0.21$ and an inclination angle of $\beta = 0°$ at a pressure of $p = 300$ mbar for three different heat fluxes ($\dot{q} = 3500\,\mathrm{W\,m^{-2}}$, $\dot{q} = 3750\,\mathrm{W\,m^{-2}}$, and $\dot{q} = 4000\,\mathrm{W\,m^{-2}}$)

of the different terms in the differential equation for the curvature (Equation 6.14) is distinguished in the curvature change due to gravity, due to friction, and due to composition. Despite the similar surface tensions of ethanol and methanol, the surface tension changes along the system due to a change in the interface temperature induced by a change in composition. Because of the horizontal position of the system, the curvature change due to gravitational influences is equal to zero over the entire length of the system. Due to the high curvature set as initial condition, the term dependent on the change in surface tension dominates the curvature radii distribution in the system. Compared to this, the curvature radius change due to friction is low for all simulations.

In the left diagram of Figure 7.4, the mean ethanol mole fraction in the liquid phase is shown over the axial position of the system. Due to the negligence of axial diffusion, the mean ethanol mole fraction in the vapor phase is at the same values (see Appendix B.1). The mean mole fraction of the less volatile component ethanol increases towards the evaporator for every simulation. This increase is strongest for the lowest heat flux. With increasing the heat flux, the increase in mean ethanol mole fraction is lower and thus the separation gets worse. To the right of Figure 7.4 the ethanol mole fractions at the interface are presented. The liquid ethanol mole fraction at the interface is always slightly higher than the mean ethanol mole fraction, except at the condenser end, where the fluid only consists of pure methanol. The vapor interface ethanol fraction is lower than the mean liquid ethanol fraction, except in the evaporator. Because of the overall average composition of the fluid, the fluid cannot get separated any further in this region and reaches a limit. This is why the vapor interface composition is equal to the mean liquid composition in this part of the system, which can be observed by comparing the left and the right diagram of Figure 7.4.

In Figure 7.5, the axial molar flow rate is presented for the different simulations. The axial flow rate is the same for the liquid and the vapor phase (see Section 6.2). In the left graph, the overall flow rate is shown. For every simulation, the flow rate increases towards the evaporator until it reaches a maximum

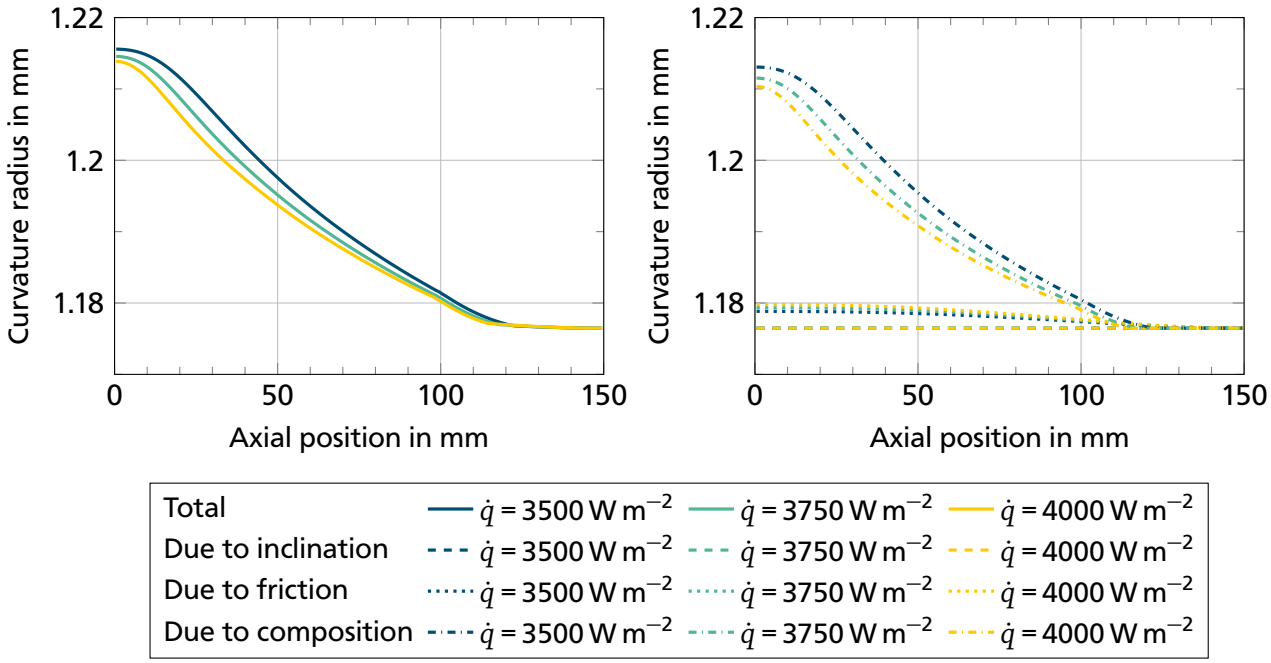

Figure 7.3: Curvature radii over the length of the re-entrant channel for an overall average ethanol mole fraction of $\widetilde{x}_{\mathrm{E,OA}} = 0.21$ and an inclination angle of $\beta = 0°$ at a pressure of $p = 300$ mbar for three different heat fluxes ($\dot{q} = 3500\,\mathrm{W\,m^{-2}}$, $\dot{q} = 3750\,\mathrm{W\,m^{-2}}$, and $\dot{q} = 4000\,\mathrm{W\,m^{-2}}$)

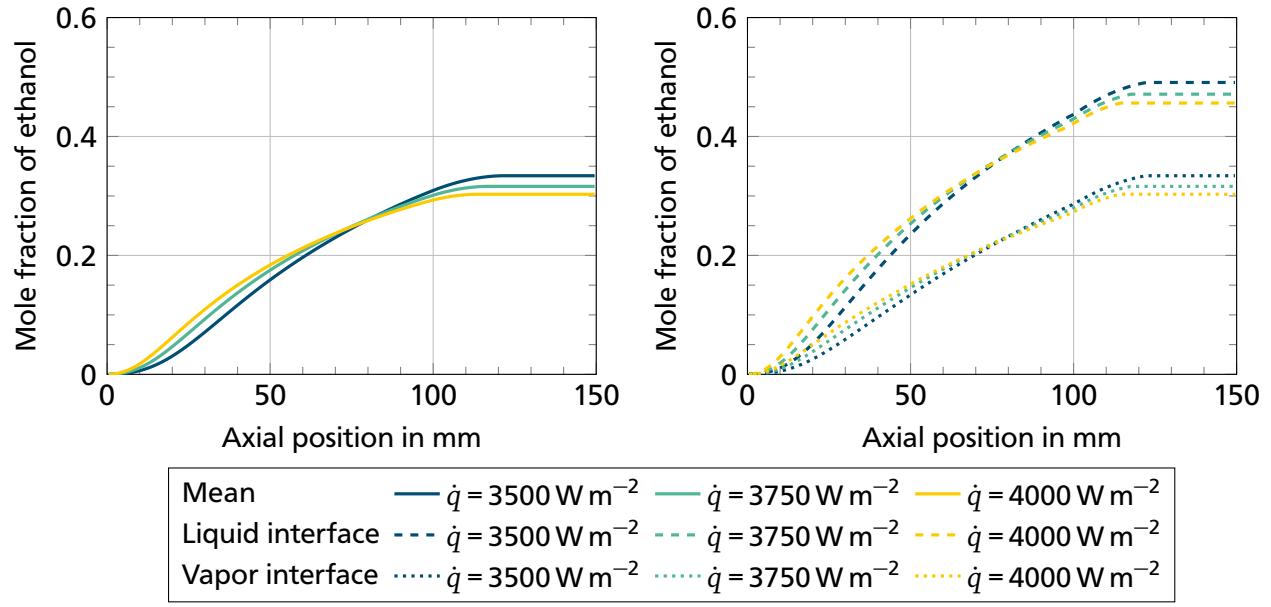

Figure 7.4: Mean ethanol mole fraction (left) and interface ethanol mole fractions (right) over the length of the re-entrant channel for an overall average ethanol mole fraction of $\widetilde{x}_{\mathrm{E,OA}} = 0.21$ and an inclination angle of $\beta = 0°$ at a pressure of $p = 300$ mbar for three different heat fluxes ($\dot{q} = 3500\,\mathrm{W\,m^{-2}}$, $\dot{q} = 3750\,\mathrm{W\,m^{-2}}$, and $\dot{q} = 4000\,\mathrm{W\,m^{-2}}$)

from which it decreases. At the boundaries of the system, the axial flow rate is equal to zero. For the lowest heat flux, the axial flow rate is the lowest at every position in the system. To the right of this figure, the molar flow rates of the different fractions of the system are shown. The ethanol flow rate is close to zero in the beginning of the condenser, while the methanol flow rate increases more rapidly. The

maximum of the methanol flow rate is always reached closer to the condenser than the maximum of the ethanol flow rate. In the region between these two maxima, methanol evaporates from the liquid phase while ethanol condenses into the liquid phase.

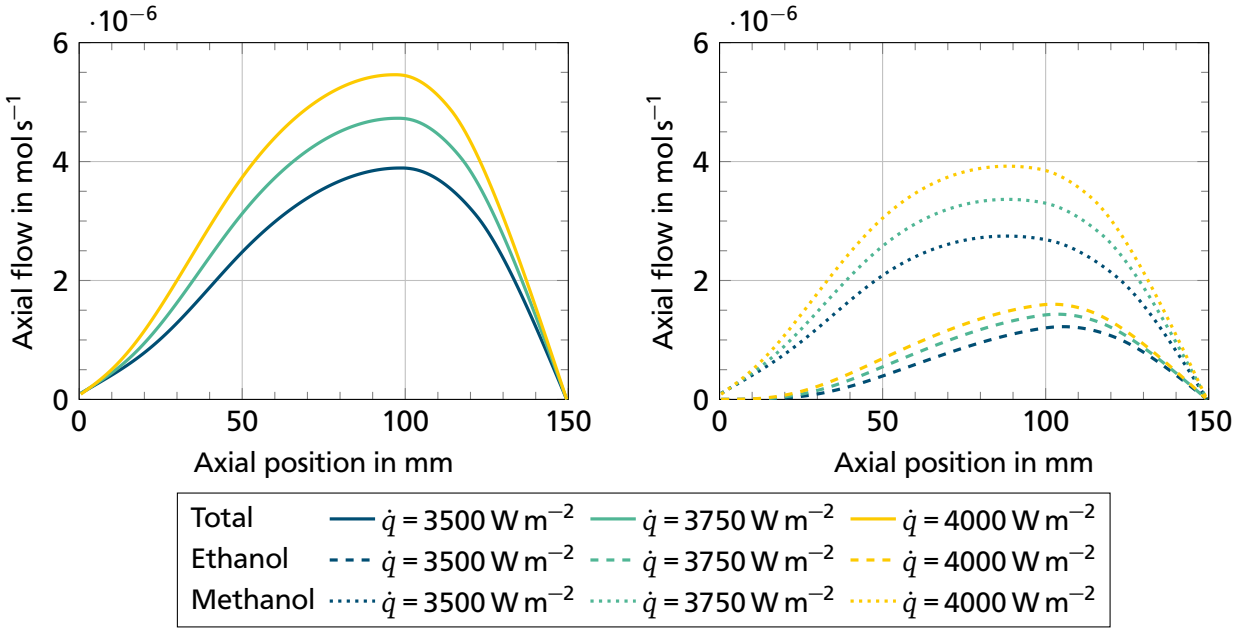

Figure 7.5: Axial flow rate over the length of the re-entrant channel for an overall average ethanol mole fraction of $\widetilde{x}_{\mathrm{E,OA}} = 0.21$ and an inclination angle of $\beta = 0°$ at a pressure of $p = 300$ mbar for three different heat fluxes ($\dot{q} = 3500\,\mathrm{W\,m^{-2}}$, $\dot{q} = 3750\,\mathrm{W\,m^{-2}}$, and $\dot{q} = 4000\,\mathrm{W\,m^{-2}}$)

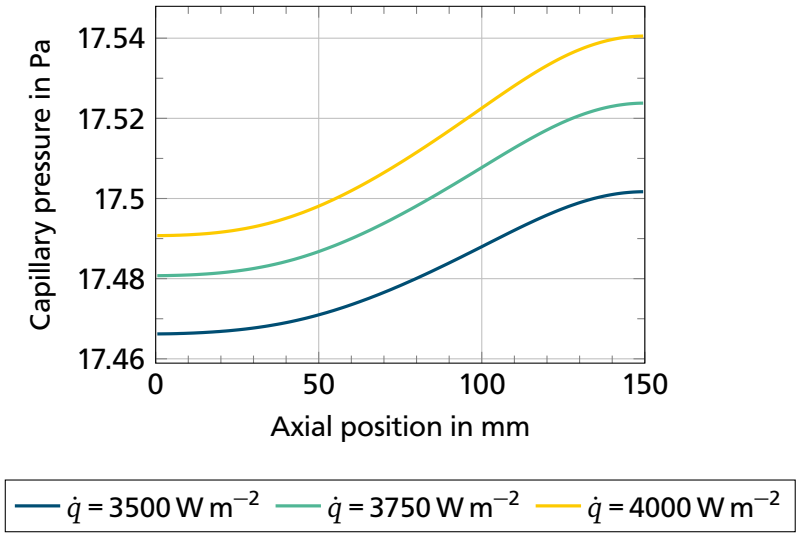

Figure 7.6: Capillary pressure over the length of the re-entrant channel for an overall average ethanol mole fraction of $\widetilde{x}_{\mathrm{E,OA}} = 0.21$ and an inclination angle of $\beta = 0°$ at a pressure of $p = 300$ mbar for three different heat fluxes ($\dot{q} = 3500\,\mathrm{W\,m^{-2}}$, $\dot{q} = 3750\,\mathrm{W\,m^{-2}}$, and $\dot{q} = 4000\,\mathrm{W\,m^{-2}}$)

In Figure 7.6, the distribution of the capillary pressure over the axial position in the system is shown. For all simulations, the capillary pressure increases towards the evaporator. At the boundaries of the system, the slope of the capillary pressure is equal to zero. The gradient of the capillary pressure is the highest close to the middle of the system where the flow rates are highest. With increasing the heat

flux, the capillary pressure increases at every axial position. For all simulations, the change in capillary pressure between the condenser end and the evaporator end is lower than 0.1 Pa. The relative change in capillary pressure is below 1 % for all simulations.

In Figure 7.7, the values of the conductive transport coefficient φ (Equation 6.22), the Poiseuille number Po (Equation 6.12), and the diffusive transport coefficient (Equation 6.34) of the liquid phase ψ_L and of the vapor phase ψ_V over the length of the system are shown. Due to the change in curvature along the main flow axis, these values change along the main flow axis and thereby influence the transport processes. The conductive transport coefficient φ and the diffusive transport coefficient of the liquid phase ψ_L increase towards the evaporator for all simulations. The Poiseuille number Po and the diffusive transport coefficient of the vapor phase ψ_V decrease towards the evaporator. For the small changes in curvature shown in Figure 7.3 the relative changes in the dimensionless parameters are small. The changes in the conductive transport coefficient are the highest but are still below 1 % in any of these simulated cases.

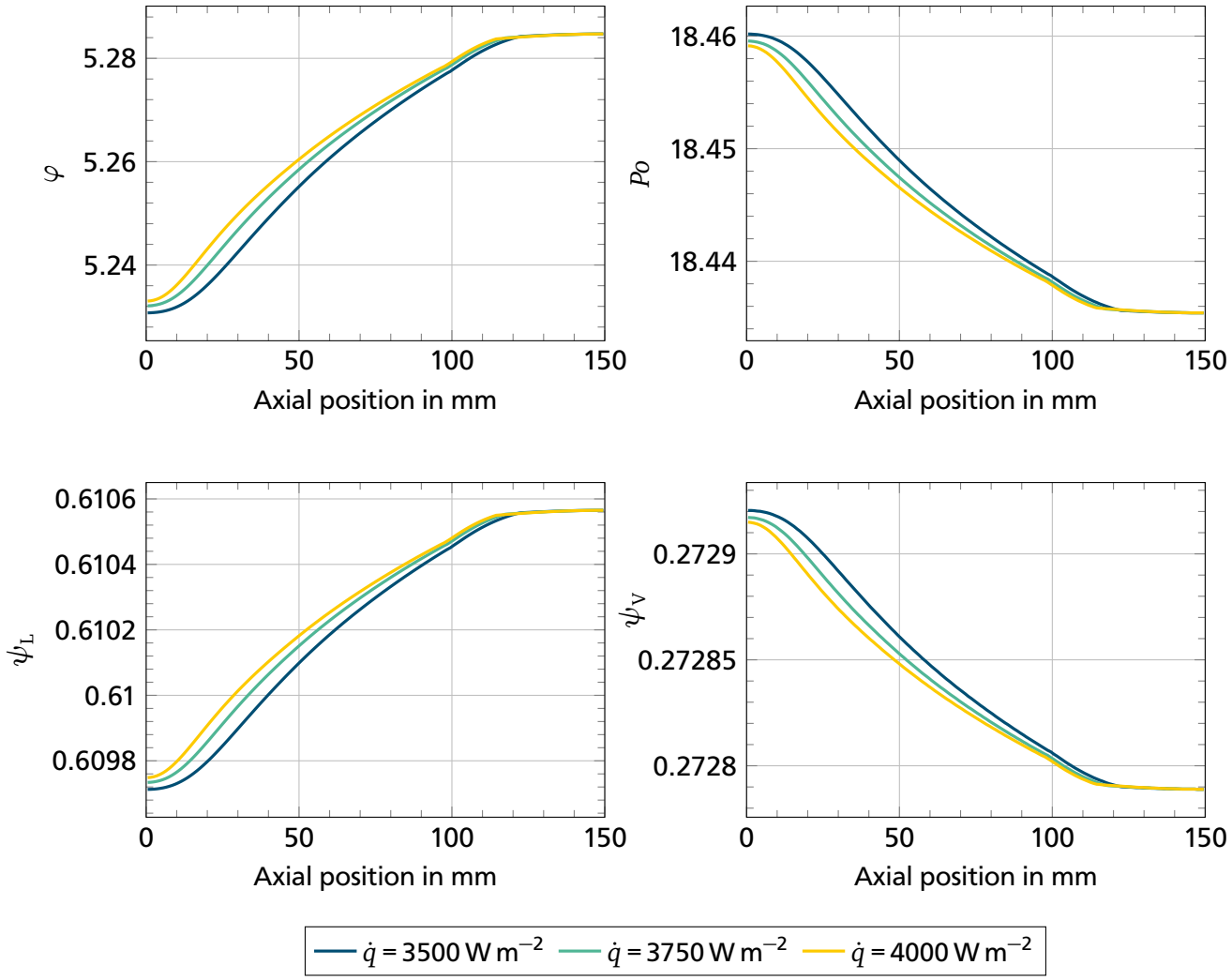

Figure 7.7: Dimensionless parameters φ, Po, ψ_L, and ψ_V over the length of the re-entrant channel for an overall average ethanol mole fraction of $\widetilde{x}_{\mathrm{E,OA}} = 0.21$ and an inclination angle of $\beta = 0°$ at a pressure of $p = 300$ mbar for three different heat fluxes ($\dot{q} = 3500\,\mathrm{W\,m^{-2}}$, $\dot{q} = 3750\,\mathrm{W\,m^{-2}}$, and $\dot{q} = 4000\,\mathrm{W\,m^{-2}}$)

With the mean ethanol mole fractions at the condenser and the evaporator boundaries, the height equivalent to a theoretical plate *HETP* can be calculated for the simulated cases. In Table 7.2 the values for the height equivalent to a theoretical plate are listed for the three simulations. For all simulations, the *HETP* values are at 30 mm. The differences in the distributions of the component fractions are too small to result in different values of the *HETP*. This is equivalent to a separation of five theoretical plates in the system.

Table 7.2: Heights equivalent to a theoretical plate for the simulations with varied heat flux

	$\dot{q} = 3500\,\mathrm{W\,m^{-2}}$	$\dot{q} = 3750\,\mathrm{W\,m^{-2}}$	$\dot{q} = 4000\,\mathrm{W\,m^{-2}}$
HETP in mm	30	30	30

7.2 Influence of the Inclination

In this section, the influence of the inclination on the process is investigated. In Figure 7.8, the temperature distributions for the inclination angles $\beta = -0.4°$, $\beta = 0°$, and $\beta = 0.4°$ are shown. A positive value of β indicates that the evaporator lies above the condenser. The temperatures in the walls and at the interface are very similar for the varied inclination angles. The reason for this is described in the following paragraphs based on the distribution of the other evaluated variables. As in the reference simulation, the temperatures in the wall and at the interface increase from the condenser to the evaporator. The temperature distributions are horizontal at the boundaries of the system reflecting the adiabatic boundary conditions.

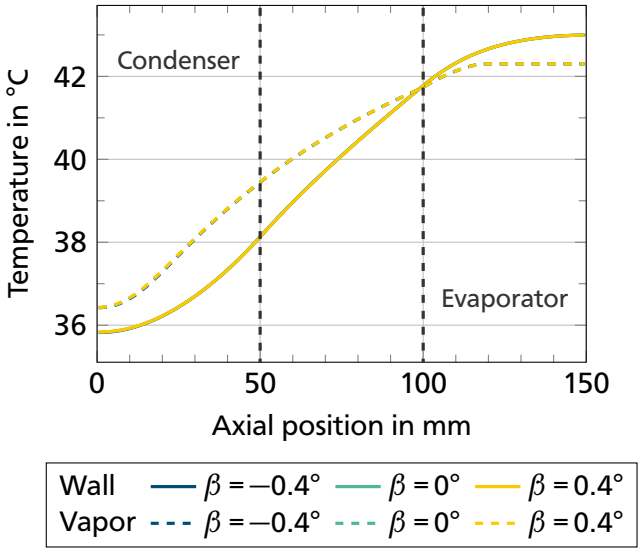

Figure 7.8: Temperature distributions over the length of the re-entrant channel for an overall average ethanol mole fraction of $\widetilde{x}_{\mathrm{E,OA}} = 0.21$ and a heat flux of $\dot{q} = 3750\,\mathrm{W\,m^{-2}}$ at a pressure of $p = 300$ mbar for three different inclination angles ($\beta = -0.4°$, $\beta = 0°$, and $\beta = 0.4°$)

In Figure 7.9, the curvature radii are presented over the length of the system. The difference between the curvature radius at the condenser boundary and at the evaporator boundary is highest for the positive inclination angle. In a horizontal system, the curvature radius also declines towards the evaporator but

this decline is weaker. For the negative inclination angle, the curvature radius increases towards the evaporator boundary. This simulation shows changes in the sign of the slope of the curvature radius. The reasons for this can be seen in the right diagram of this figure. For the negative inclination angle, the curvature radius change by gravity is positive towards the evaporator. The influences of gravity and of the composition change on the curvature radius work in different directions and are of similar magnitude in this case. In the horizontal case, the change in curvature radius by gravity is equal to zero. For the positive inclination angle, the decrease in curvature radius by gravity is stronger than the decrease by a change in composition along the main flow axis. The flow must work against gravity in this case. The change in curvature radius by gravity and by composition work in the same direction and thus add up. The influence of friction on the curvature radii is negligible in all cases.

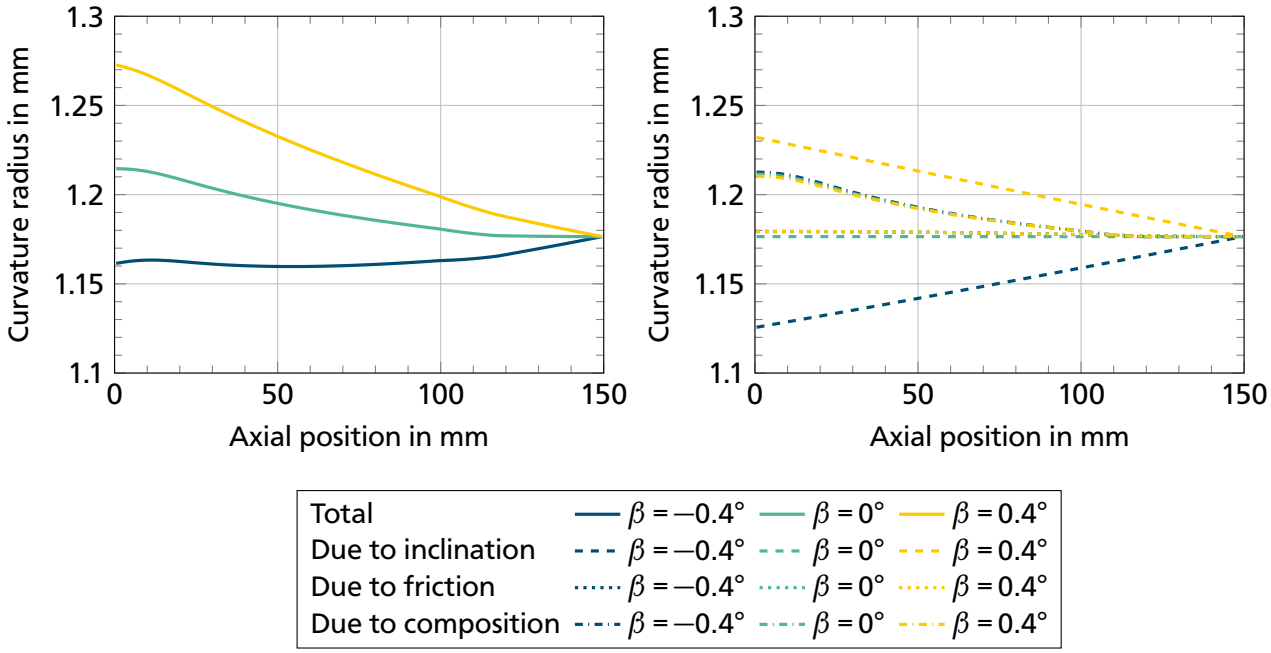

Figure 7.9: Curvature radii over the length of the re-entrant channel for an overall average ethanol mole fraction of $\widetilde{x}_{\mathrm{E,OA}} = 0.21$ and a heat flux of $\dot{q} = 3750\,\mathrm{W\,m^{-2}}$ at a pressure of $p = 300\,\mathrm{mbar}$ for three different inclination angles ($\beta = -0.4°$, $\beta = 0°$, and $\beta = 0.4°$)

In Figure 7.10, the mean ethanol fraction and the interface ethanol mole fractions are shown. In accordance with the temperature distributions, no influence of the plate inclination angle can be observed and the observations made for the reference simulation for the varied heat flux hold true again. The same can be said for the overall axial flow rate and the component axial flow rates, which are shown in Figure 7.11.

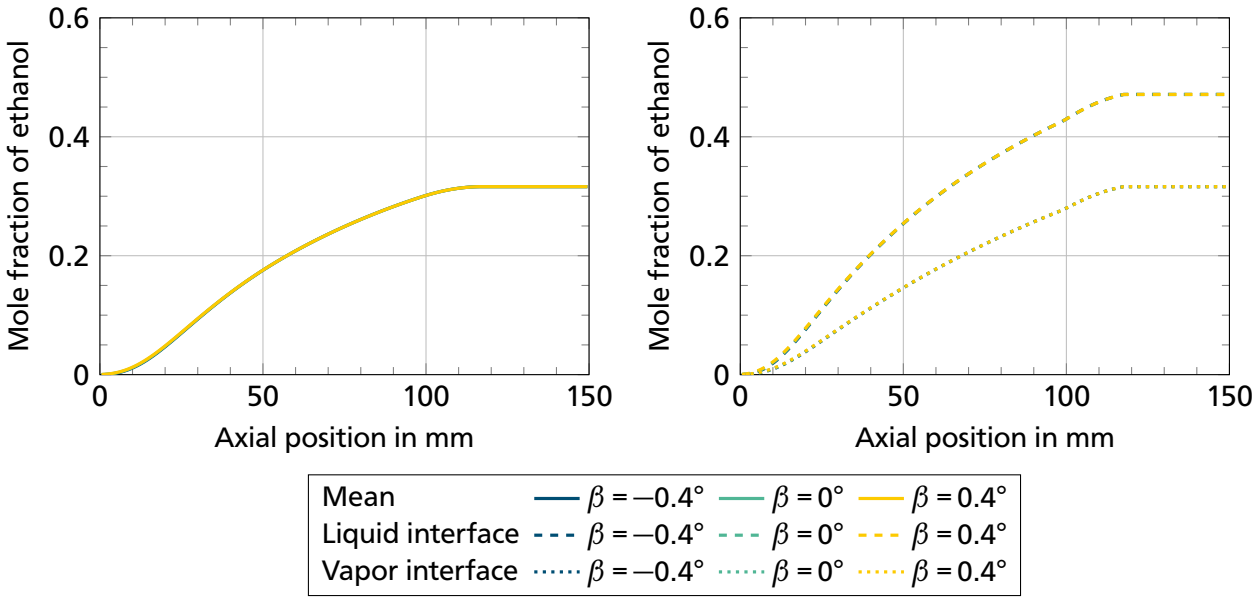

Figure 7.10: Mean ethanol mole fraction (left) and interface ethanol mole fractions (right) over the length of the re-entrant channel for an overall average ethanol mole fraction of $\widetilde{x}_{\mathrm{E,OA}} = 0.21$ and a heat flux of $\dot{q} = 3750\,\mathrm{W\,m^{-2}}$ at a pressure of $p = 300$ mbar for three different inclination angles ($\beta = -0.4°$, $\beta = 0°$, and $\beta = 0.4°$)

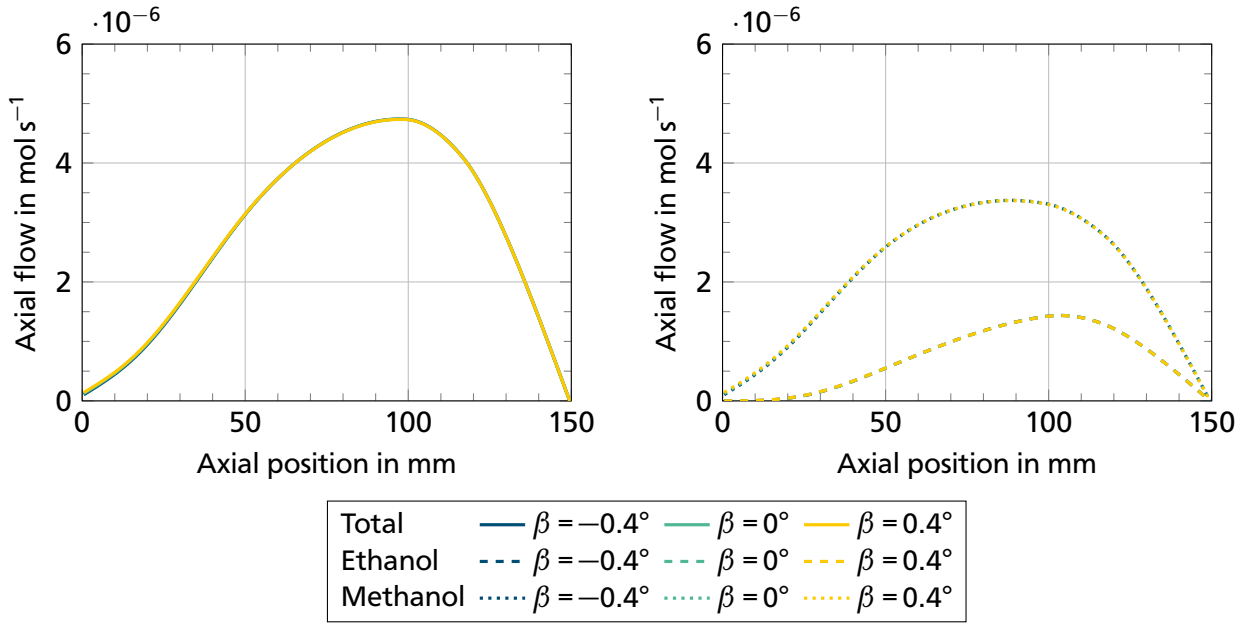

Figure 7.11: Axial flow rate over the length of the re-entrant channel for an overall average ethanol mole fraction of $\widetilde{x}_{\mathrm{E,OA}} = 0.21$ and a heat flux of $\dot{q} = 3750\,\mathrm{W\,m^{-2}}$ at a pressure of $p = 300$ mbar for three different inclination angles ($\beta = -0.4°$, $\beta = 0°$, and $\beta = 0.4°$)

In Figure 7.12, the distribution of the capillary pressure is shown over the axial position in the system. Whereas the capillary pressure increases towards the evaporator for $\beta = 0°$ and $\beta = 0.4°$, it decreases for $\beta = -0.4°$. The increase in capillary pressure for the horizontal system is small compared to the increase in capillary pressure for the system at a positive inclination angle. For the low axial flow rates, the influence of friction on the change in capillary pressure is negligible compared to the change induced by gravity. The change in capillary pressure is below 1 Pa for all systems.

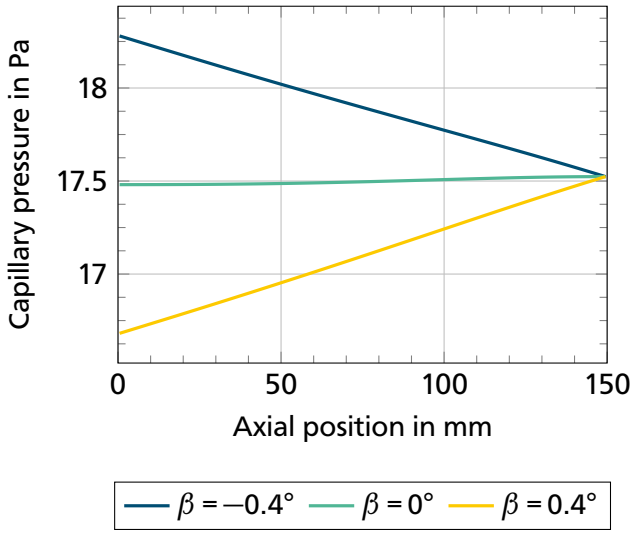

Figure 7.12: Capillary pressure over the length of the re-entrant channel for an overall average ethanol mole fraction of $\widetilde{x}_{\mathrm{E,OA}} = 0.21$ and a heat flux of $\dot{q} = 3750\,\mathrm{W\,m^{-2}}$ at a pressure of $p = 300$ mbar for three different inclination angles ($\beta = -0.4°$, $\beta = 0°$, and $\beta = 0.4°$)

In Figure 7.13, the development of the dimensionless parameters over the axial length is shown. As for the simulations with varied heat flux, the dimensionless groups barely change along the main flow axis even though the variation of the curvature is stronger for the varied inclinations. For the positive inclination angle towards the horizontal, the change in the conductive transport coefficient along the main flow axis is around 3 %. This change is too small to significantly influence the heat transfer and as a consequence the mass transfer processes.

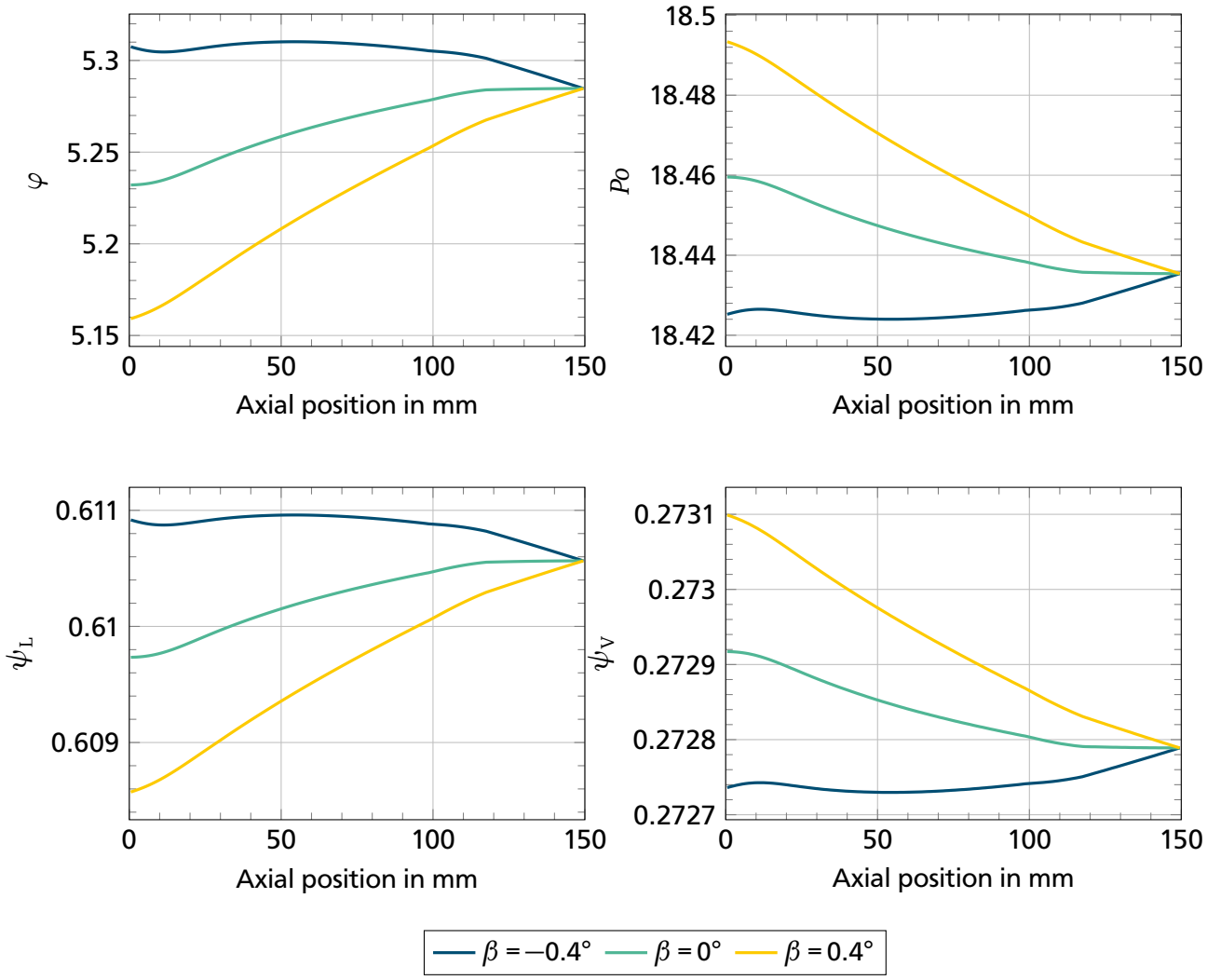

Figure 7.13: Dimensionless parameters φ, Po, ψ_{L}, and ψ_{V} over the length of the re-entrant channel for an overall average ethanol mole fraction of $\widetilde{x}_{\mathrm{E,OA}} = 0.21$ and a heat flux of $\dot{q} = 3750\,\mathrm{W\,m^{-2}}$ at a pressure of $p = 300$ mbar for three different inclination angles ($\beta = -0.4°$, $\beta = 0°$, and $\beta = 0.4°$)

In Table 7.3, the values of the height equivalent to a theoretical plate calculated are given for the three simulations with varied inclination angles. As for the varied heat flux, the calculated values are at 30 mm for every simulation.

Table 7.3: Heights equivalent to a theoretical plate for the simulations with varied inclination

	$\beta = -0.4°$	$\beta = 0°$	$\beta = 0.4°$
HETP in mm	30	30	30

7.3 Influence of the Capillary Structure

In this section, the influence of the capillary structure is evaluated. For the re-entrant channel, the radius of the circular part of the channel cross section is varied ($R_{RE} = 650\,\mu m$, $R_{RE} = 800\,\mu m$, and $R_{RE} = 950\,\mu m$). In Figure 7.14, the temperature distributions in the system are shown for the three simulations. For the capillary structure with the smallest radius, the temperature difference between the evaporator boundary and the condenser boundary in the wall and at the interface is the highest. With increasing radius of the re-entrant channel, the temperature difference between the evaporator boundary and the condenser boundary decreases. The reason for this are the higher axial flow rates for higher channel radii (compare Figure 7.17), which lead to lower axial heat conduction.

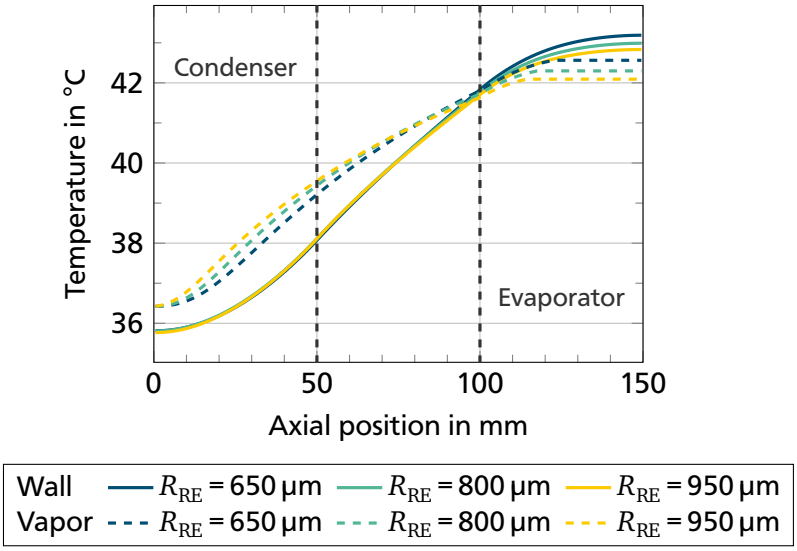

Figure 7.14: Temperature distributions over the length of the re-entrant channel for an overall average ethanol mole fraction of $\tilde{x}_{E,OA} = 0.21$, a heat flux of $\dot{q} = 3750\,W\,m^{-2}$, and an inclination angle of $\beta = 0°$ at a pressure of $p = 300\,mbar$ for three different radii of the re-entrant channel ($R_{RE} = 650\,\mu m$, $R_{RE} = 800\,\mu m$, and $R_{RE} = 950\,\mu m$)

In Figure 7.15 the distribution of the curvature radii in the system is shown. For the smallest radius of the re-entrant channel, the difference between the curvature radius between the condenser boundary and the evaporator boundary is the highest. With increasing the channel radius, the change in curvature radius over the length of the system gets smaller. In the right part of Figure 7.15, it can be observed that the change in curvature radius by composition increases with decreasing the channel radius. The same

holds true for the change in curvature radius by friction. The change in curvature radius due to gravity is equal to zero in all cases.

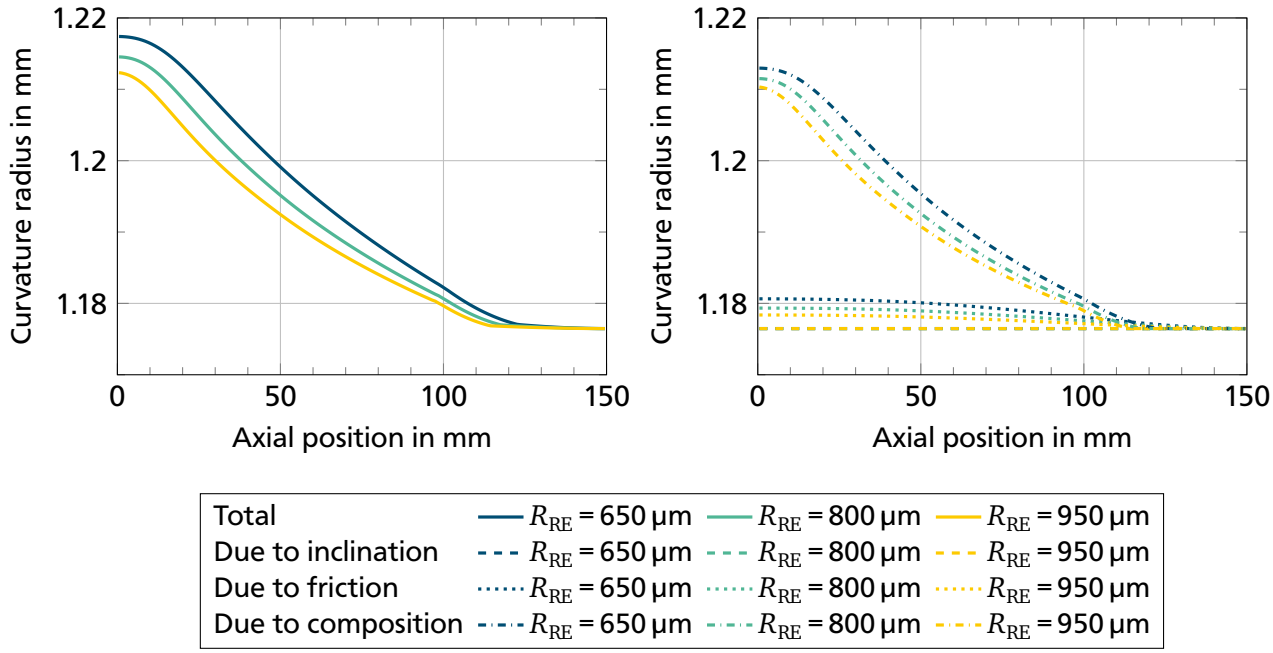

Figure 7.15: Curvature radii over the length of the re-entrant channel for an overall average ethanol mole fraction of $\widetilde{x}_{E,OA} = 0.21$, a heat flux of $\dot{q} = 3750\,W\,m^{-2}$, and an inclination angle of $\beta = 0°$ at a pressure of $p = 300$ mbar for three different radii of the re-entrant channel ($R_{RE} = 650$ µm, $R_{RE} = 800$ µm, and $R_{RE} = 950$ µm)

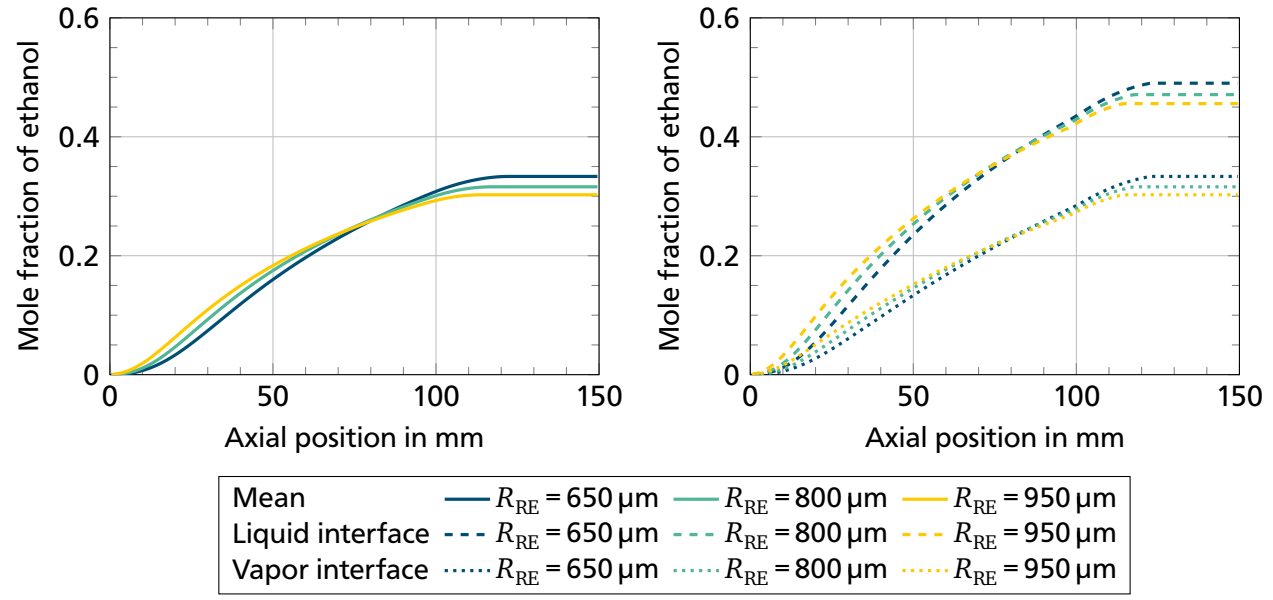

Figure 7.16: Mean ethanol mole fraction (left) and interface ethanol mole fractions (right) over the length of the re-entrant channel for an overall average ethanol mole fraction of $\widetilde{x}_{E,OA} = 0.21$, a heat flux of $\dot{q} = 3750\,W\,m^{-2}$, and an inclination angle of $\beta = 0°$ at a pressure of $p = 300$ mbar for three different radii of the re-entrant channel ($R_{RE} = 650$ µm, $R_{RE} = 800$ µm, and $R_{RE} = 950$ µm)

In Figure 7.16, the mean ethanol mole fraction and the interface ethanol mole fractions are shown over the length of the system. With decreasing the radius of the re-entrant channel, the increase in the mean ethanol mole fraction towards the evaporator gets stronger. Thus, a smaller channel radius leads to a better separation. As for the mean ethanol mole fraction, the increase in the interface ethanol mole fractions is also stronger for lower channel radii.

In Figure 7.17, the molar flow rates of the simulations with varied capillary structures are presented. For the lowest channel radius, the maximum axial flow rate is also the lowest. The maximum axial flow rate increases with increasing the radius. With increasing the radius, the maximum overall molar flow rate is reached slightly closer to the condenser. The same holds true for the ethanol flow rate, which can be observed in the right part of Figure 7.17. The axial position of the maximum of the methanol flow rate is relatively constant for all three simulations.

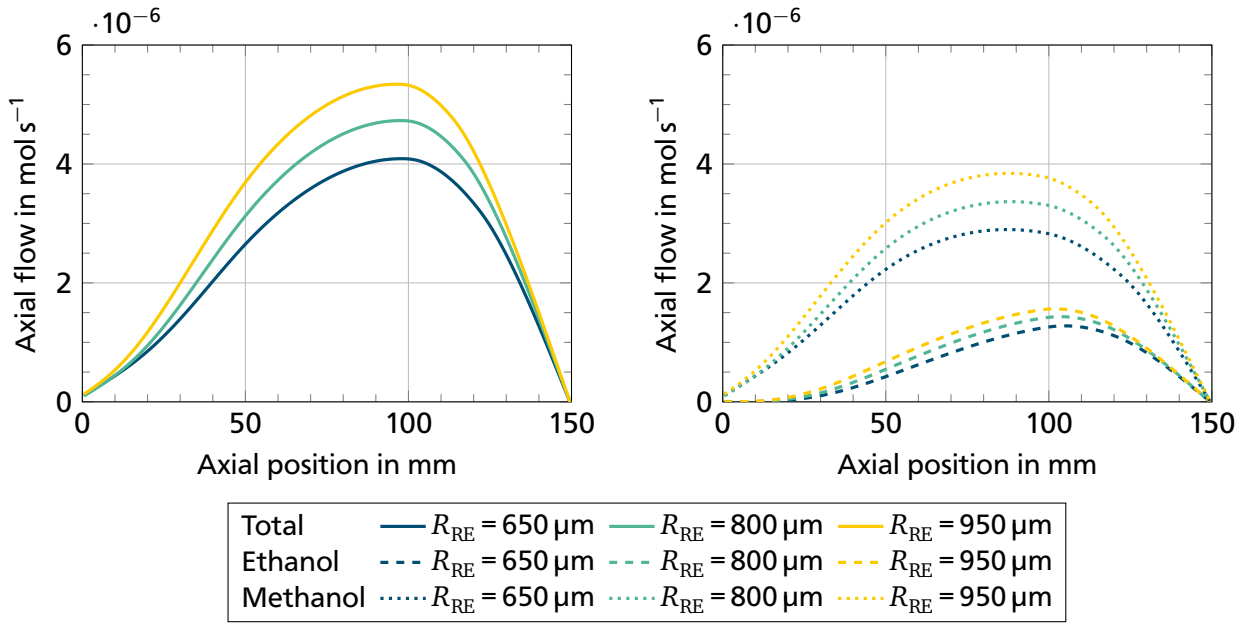

Figure 7.17: Axial flow rate over the length of the re-entrant channel for an overall average ethanol mole fraction of $\widetilde{x}_{\mathrm{E,OA}} = 0.21$, a heat flux of $\dot{q} = 3750\,\mathrm{W\,m^{-2}}$, and an inclination angle of $\beta = 0°$ at a pressure of $p = 300$ mbar for three different radii of the re-entrant channel ($R_{\mathrm{RE}} = 650\,\mu\mathrm{m}$, $R_{\mathrm{RE}} = 800\,\mu\mathrm{m}$, and $R_{\mathrm{RE}} = 950\,\mu\mathrm{m}$)

In Figure 7.18, the distribution of the capillary pressure is shown over the length of the system. The capillary pressure increases from the condenser boundary towards the evaporator. With increasing the channel radius, the values of the capillary pressure increase at every axial position. The capillary pressure difference between the evaporator boundary and the condenser boundary is lowest for the highest channel radius and increases with decreasing the radius. Due to the horizontal system all axial pressure losses are due to friction. Thus, the axial pressure losses due to friction are highest for the capillary structure with the lowest radius of the re-entrant channel, although the molar flow rate is the smallest for this capillary structure. For all simulations, the capillary pressure difference is lower than 0.1 Pa.

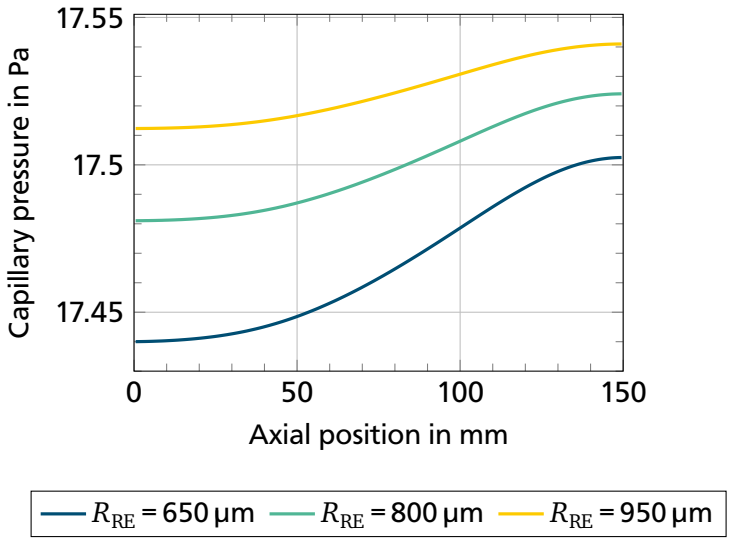

Figure 7.18: Capillary pressure over the length of the re-entrant channel for an overall average ethanol mole fraction of $\widetilde{x}_{E,OA} = 0.21$, a heat flux of $\dot{q} = 3750\,W\,m^{-2}$, and an inclination angle of $\beta = 0°$ at a pressure of $p = 300$ mbar for three different radii of the re-entrant channel ($R_{RE} = 650$ µm, $R_{RE} = 800$ µm, and $R_{RE} = 950$ µm)

In Figure 7.19 the dimensionless parameters over the axial length are depicted for the varied radii of the re-entrant structure. The macroscopic conductive transport coefficients barely differ from each other for the different channel radii. The vapor phase has the same dimensions for the three structures since the channel width does not change. The only effect leading to differences in the diffusive transport coefficient of the vapor phase are the different changes in curvature radii along the main flow axis for the different simulations. Strong differences (compared to the differences of φ) between the capillary structures in the dimensionless parameters can be observed for the Poiseuille number and for the diffusive transport coefficient of the liquid phase. The reason for this, is the different structure of the Poisson equations solved for the determination of ψ_L and *Po* compared to the Laplace equation solved for the determination of φ. The values of the Poiseuille number decrease with increasing the channel radius. Thus, the axial flow resistance decreases with increasing the channel radius. This explains the stronger increase in the capillary pressure for the channel with the smallest radius despite the lowest flow rate. For the lowest radius, the values of the diffusive transport coefficient of the liquid phase are almost 10 % higher than for the highest channel radius. The change in curvature radius along the main flow axis has a negligible influence on the transport properties in this system. Additionally, the wall area in every cross section increases with decreasing the channel radius since the outer dimensions of the metal plate remain constant. Thus, it can be concluded, that the higher values of ψ_L or the increased area for axial heat conduction lead to the observable increase in separation with decreasing the channel radius.

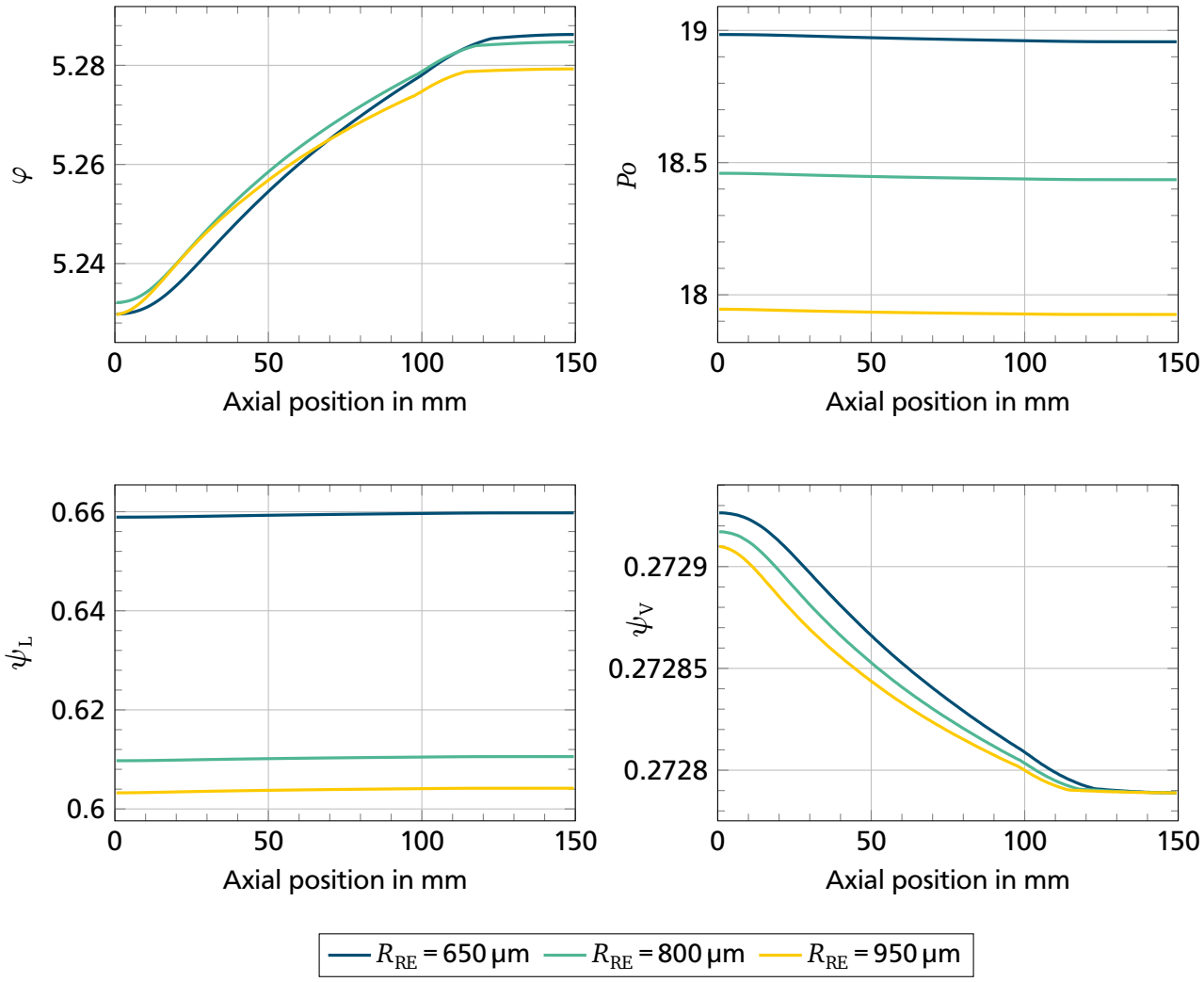

Figure 7.19: Dimensionless parameters φ, Po, ψ_{L}, and ψ_{V} over the length of the re-entrant channel for an overall average ethanol mole fraction of $\widetilde{x}_{\mathrm{E,OA}} = 0.21$, a heat flux of $\dot{q} = 3750\,\mathrm{W\,m^{-2}}$, and an inclination angle of $\beta = 0°$ at a pressure of $p = 300$ mbar for three different radii of the re-entrant channel ($R_{\mathrm{RE}} = 650\,\mu\mathrm{m}$, $R_{\mathrm{RE}} = 800\,\mu\mathrm{m}$, and $R_{\mathrm{RE}} = 950\,\mu\mathrm{m}$)

In Table 7.4, the calculated values for the heights equivalent to a theoretical plate are stated for the three simulations. For all varied channel radii the height equivalent to a theoretical plate is equal to 30 mm.

Table 7.4: Heights equivalent to a theoretical plate for the simulations with varied capillary structure

	$R_{\mathrm{RE}} = 650\,\mu\mathrm{m}$	$R_{\mathrm{RE}} = 800\,\mu\mathrm{m}$	$R_{\mathrm{RE}} = 950\,\mu\mathrm{m}$
HETP in mm	30	30	30

7.4 Conclusions

For the investigated system, the heat flux and the dimensions of the capillary structures show an observable influence on the separation of the investigated mixture. The influence of the inclination on the separation is negligible. The hydrodynamics does not strongly influence the liquid area of flow for the investigated

capillary structure. This leads to small changes of the transport coefficients along the main flow axis. In the case of stronger curvature changes, the impact of the hydrodynamics on the transport processes in the system could increase. One reason for stronger curvature changes could be mixtures with considerably different surface tensions or differently shaped capillary structures.

A variation of the heat flux can influence the separation. For the investigated capillary structure, the separation increases with decreasing heat flux. Additionally, the axial flow rate decreases with decreasing heat flux. With the comparison of the capillary structures, it is shown that the design of the capillary structure has a considerable impact on the separation. The increased separation efficiency for the decreased channel diameter can either be attributed to the increased values of the diffusive transport coefficient in the liquid ψ_{L} or to the increased axial conductive area. The change in Poiseuille number is not relevant due to the negligible influence of the hydrodynamics on the system. The heights equivalent to a theoretical plate are at 30 mm for all the simulations. The values are therefore of the same order of magnitude as the *HETP* obtained by Sundberg *et al.* [74] in their experimental setup and obtained by Rieks *et al.* [57] in their simulations for metallic foams. Compared to conventional macro-scale rectification columns, the values of the height equivalent to a theoretical plate are approximately one order of magnitude smaller (compare [33]).

For the investigated system, the hydrodynamics do not have a significant influence on the separation and the capillary pressure differences are small. In this case, the model could be simplified through neglecting the hydrodynamics. The focus of the capillary structure design could be rather on heat and mass transfer than on hydrodynamics. Therefore, higher channel opening widths than for the re-entrant channel would be possible. With the simulations presented in this work, a conclusion on whether optimizing heat or mass transfer is more beneficial for an enhanced separation is not possible. To do so, the transport coefficients φ and ψ_{L} and the axial conductive area would need to be varied independently from each other.

Compared to the experimental results, the increase in the heat flux shows the same qualitative influence on the separation efficiency. The influence of the hydrodynamics is higher in the experiment for the same inclination angles. This is possibly due to the higher change of the transport capabilities in the triangular groove compared to the re-entrant channel. In the experiments, the contact line does not pin at the upper end of the channel. Additionally, the capillary pressure differences observable in the experiment are considerably higher than in the simulation. This is even the case for experiments with strong axial heat conduction. In the experiments, different mass transfer processes are observed for different parameters based on the interface composition profiles. Due to the lower pressures and the greater height of the vapor phase, axial diffusion could be a more relevant transport process. Additionally, for experiments with comparatively high evaporative heat flows, convection perpendicular to the main flow direction is most likely relevant.

Chapter 8

Summary and Outlook

In this thesis, the coupled transport processes in zero-gravity distillation columns were analyzed. An experimental setup was developed and built, which allows the investigation of zero-gravity distillation at infinite reflux. The system can be observed with a high spatial resolution. The capillary structures in the experimental setup can be exchanged. To resolve the interaction of hydrodynamics, heat, and mass transfer, different variables were measured. These are: the liquid-vapor interface shape, the temperatures in the walls of the capillary structure and in the vapor phase, and the liquid composition at the condenser.

As a second step, a theoretical model was developed, which describes the transport processes in zero-gravity distillation columns with channel-shaped capillary structures. In this model, hydrodynamics, heat transfer, and mass transfer are coupled. Compared to existing models, this model is the first to describe zero-gravity distillation in channel-shaped capillary structures. Additionally, no models described the axial heat conduction in the walls and took micro region evaporation into account thus far. The hydrodynamics are resolved in a more detailed manner and, thus, the influence of the changing interface curvature on the process can be evaluated.

In the **experiment**, the influence of the fluid composition, the heat flux, the inclination of the copper plate, and the geometry of the capillary structure was evaluated. For different **fluid compositions** the distributions of the temperatures, curvature radii, and the resulting separation varied. The temperature differences in the system decreased and, thus, the axially conducted heat flow did, as well. The absolute capillary pressure in most of the experiments decreased with increasing the ethanol fraction. The separation efficiency in terms of the difference between the ethanol mole fraction of the distilled sample at the condenser and the overall average ethanol mole fraction decreased with increasing the ethanol fraction. Due to the lower absolute values of the slope of the saturation lines for high ethanol fractions, the mixture behavior is closer to pure fluids for higher ethanol fractions. Additionally, the results suggest that the flow rates decrease with decreasing the ethanol fraction, which can promote separation.

For a varied **heat flux** at the evaporator, differences could be observed in all measured variables. With increasing the heat flux, the axially conducted heat flow increased. The curvature radii got smaller with increasing the heat flux and the liquid got pulled back further into the capillary structure towards the evaporator. The calculated capillary pressure difference between the evaporator and the condenser

increased with increasing the heat flux. With increasing the heat flux, the separation efficiency decreased. A likely reason for this is the increased mass flow rate with increasing the heat flux.

Varying the **inclination** of the system had a major impact on the hydrodynamics. The curvature distributions in the system varied strongly. When the evaporator lay higher than the condenser (positive inclination angle), the liquid got pulled back into the groove towards the evaporator and the curvature radii in the different grooves deviated considerably in the evaporator section. When the evaporator lay lower than the condenser (negative inclination angle), gravity supported the liquid flow and the groove filling was higher at the evaporator than at the condenser. In this case, the temperature distributions varied considerably from the ones measured in horizontal position and with a positive inclination angle. Additionally, the separation efficiency for the negative inclination was considerably higher than for the horizontal system and the positively inclined system. With increasing the inclination angle, the capillary pressure difference between evaporator and condenser increased.

For different **capillary structures**, differences in the measured variables could be observed. Nevertheless, no clear trend on the influence of the capillary structure could be formulated since the observations varied for different fluid compositions.

For the different experiments, the distribution of the interface ethanol mole fraction compared to the overall average ethanol mole fraction changed considerably. These differences suggest that the mass transfer processes vary significantly depending on the set of parameters.

The theoretical **model** was applied to a re-entrant groove structure with different heat fluxes, inclination angles, and radii of the circular part of the channel cross section. With varied **heat flux** at the condenser and the evaporator, the temperature distributions in the system changed. Counter intuitively, the temperature difference between the evaporator and the condenser in the wall increased with decreasing heat flux. The reason for this is the lower axial flow rate for lower heat fluxes. The absolute conducted heat flow decreased with increasing the heat flow. A decreasing heat flux led to a better separation. The main reason for this is the lower axial molar flow rate. A considerable change in the transport properties of the capillary structure due to a change in curvature could not be observed.

With varied **inclination**, the capillary pressure differences between the condenser and the evaporator strongly differed. For the investigated inclination angles of $\beta = -0.4°$ and $\beta = 0.4°$ the capillary pressure difference induced by gravity was much higher than the pressure difference due to friction. This led to different distributions of the curvature radius. Although the changes in the curvature radius were stronger than for the varied heat flux, the transport properties of the investigated structure barely changed along the main flow axis. Thus, no changes in the temperature distributions, flow rates, and in the separation were observed for different inclinations.

To evaluate the influence of the **capillary structures**, the radius of the circular cross section of the re-entrant channel was varied. Differences between the simulations could be seen in all evaluated parameters. For the lowest radius of the circular cross section part, the temperature difference between the evaporator and the condenser was the highest. With increasing the radius, this temperature difference decreased. This is in accordance with the lower flow rate for the smaller channel radius. Despite the lower flow rate, the capillary pressure difference increased with decreasing channel radius. The reason for this is the higher flow resistance for smaller channel radii. The separation of the mixture increased with decreasing channel radius.

The qualitative influence of the heat flux was the same in the experiment and simulation. The influence of the inclination on the experiment was stronger. The reason for this might be the stronger changes in the transport properties of the capillary structure with the varied contact line position. This effect is not taken into account in the theoretical model. The capillary pressure differences in the experiments were considerably higher than in the simulation. Depending on the process parameters, a higher share of the supplied heat flow can be consumed by evaporation in the experiment than in the simulations. This leads to the conclusion that convective mass transfer perpendicular to the main flow direction must play a role in the experiment. The larger values of the calculated pressure differences in the experiment suggest that the pressure difference in the vapor phase is possibly not negligible.

To describe the transport processes in the system for various capillary structures and heat fluxes, the model should be further developed to account for the influence of convective mass transfer perpendicular to the main flow direction and of axial diffusion, especially in the vapor phase. In order to describe systems in which the components exhibit higher differences in surface tension, the influence of Marangoni flows should be implemented in the model. This is the case for many mixtures of water and alcohols. In the current state of development, the model assumes a constant wall temperature in every cross section. For micro region evaporation, the influence of the temperature gradient in one wall cross section can influence the evaporative heat flows. In the future, this effect should be accounted for.

In the past, porous structures led to promising results in zero-gravity distillation columns. These should be experimentally investigated in the developed setup in order to directly compare the results to channel-shaped capillary structures.

With different pressures in the experiments, the diffusion coefficient of the vapor phase changes. This influences the importance of axial diffusion compared to convection in the vapor phase. In the future, experiments in which the pressure is varied on purpose can lead to insights regarding the influence of convective and diffusive transport processes on the separation efficiency.

The results obtained at infinite reflux should be compared to results with varied reflux ratios in a different setup. With this further step, the quantity of the product streams can be related to their purity. This is a necessary step to enable the industrial application of zero-gravity distillation.

Bibliography

[1] Y. Abe, "Self-rewetting fluids: Beneficial aqueous solutions", *Annals of the New York Academy of Sciences*, vol. 1077, no. 1, pp. 650–667, 2006.

[2] Y. Abe, "Terrestrial and microgravity applications of self-rewetting fluids", *Microgravity Science and Technology*, vol. 19, no. 3-4, pp. 11–12, 2007.

[3] Y. Abe, A. Iwasaki, and K. Tanaka, "Microgravity experiments on phase change of self-rewetting fluids", *Annals of the New York Academy of Sciences*, vol. 1027, no. 1, pp. 269–285, 2004.

[4] Y. Abe, A. Iwaski, and K. Tanaka, "Thermal management with self-rewetting fluids", *Microgravity-Science and Technology*, vol. 16, no. 1-4, pp. 148–152, 2005.

[5] Y. Abe, K. Tanaka, M. Nakagawa, N. di Francescantonio, R. Savino, and A. Iwasaki, "Flexible wickless heat pipes radiator with self-rewetting fluids", in *9th AIAA/ASME Joint Thermophysics and Heat Transfer Conference*, 2006, pp. 1–10.

[6] C. Adiche and K. Sundmacher, "Experimental investigation on a membrane distillation based micro-separator", *Chemical Engineering and Processing: Process Intensification*, vol. 49, no. 4, pp. 425–434, 2010.

[7] S. Batzdorf, "Heat transfer and evaporation during single drop impingement onto a superheated wall", PhD thesis, Technische Universität Darmstadt, 2015.

[8] D. A. Boyd, J. R. Adleman, D. G. Goodwin, and D. Psaltis, "Chemical separations by bubble-assisted interphase mass-transfer", *Analytical Chemistry*, vol. 80, no. 7, pp. 2452–2456, 2008.

[9] C. Brandt, *Wärme- und Flüssigkeitstransport in Verdampfern von Wärmerohren mit Hochleistungskapillarstrukturen*. VDI-Verlag, 2003.

[10] C. Brandt, P. Stephan, M. Dubois, and B. Mullender, "Theoretical investigation of advanced capillary structures in grooved heat pipe evaporators for space applications", SAE Technical Paper, Tech. Rep., 2000.

[11] S. Buchholz, "Future manufacturing approaches in the chemical and pharmaceutical industry", *Chemical Engineering and Processing: Process Intensification*, vol. 49, no. 10, pp. 993–995, 2010.

[12] J. Carey and W. Lewis, "Studies in distillation", *Industrial & Engineering Chemistry*, vol. 24, no. 8, pp. 882–883, 1932.

[13] A. Cecere, D. De Cristofaro, R. Savino, V. Ayel, T. Sole-Agostinelli, M. Marengo, C. Romestant, and Y. Bertin, "Experimental analysis of a flat plate pulsating heat pipe with self-rewetting fluids during a parabolic flight campaign", *Acta Astronautica*, vol. 147, pp. 454–461, 2018.

[14] F. Größmann, "Untersuchung der Verdampfung aus strukturierten Oberflächen in Reinstoffatmosphäre", PhD thesis, Technische Universität Darmstadt, 2016.

[15] N. Damean and P. Regtien, "Poiseuille number for the fully developed laminar flow through hexagonal ducts etched in <1 0 0> silicon", *Sensors and Actuators A: Physical*, vol. 90, no. 1-2, pp. 96–101, 2001.

[16] R. Di Paola, R. Savino, D. M. Gattia, R. Marazzi, and M. V. Antisari, "Self-rewetting carbon nanofluid as working fluid for space and terrestrial heat pipes", *Journal of Nanoparticle Research*, vol. 13, no. 11, pp. 6207–6216, 2011.

[17] M. Dubois, B. Mullender, S. Van Oost, and W. Supper, "High capacity grooved heat pipes", SAE Technical Paper, Tech. Rep., 1993.

[18] EA Elektro-Automatik GmbH & Co. KG, `https://elektroautomatik.com/media/pdf/e8/06/d0/datasheet_ps8000-2u.pdf`, [Online; accessed on 13 September 2019].

[19] M. Foerster, K. Lam, E. Sorensen, and A. Gavriilidis, "In situ monitoring of microfluidic distillation", *Chemical engineering journal*, vol. 227, pp. 13–21, 2013.

[20] N. di Francescantonio, R. Savino, and Y. Abe, "New alcohol solutions for heat pipes: Marangoni effect and heat transfer enhancement", *International Journal of Heat and Mass Transfer*, vol. 51, no. 25, pp. 6199–6207, 2008.

[21] M. Furrer, L. Saraceno, A. Mariani, and G. P. Celata, "Capillary pressure influence on open channels pressure drop", *International Journal of Thermal Sciences*, vol. 70, pp. 102–113, 2013.

[22] J. Gmehling, U. Onken, and W. Arlt, *Chemistry data series, Volume I, Part 1: Aqueous-organic systems*. Dechema Frankfurt, Germany, 1977.

[23] M. Grünewald and J. Heck, "Modulare Verfahrenstechnik: Neue Anforderungen an die Apparateentwicklung", *Chemie Ingenieur Technik*, vol. 87, no. 9, pp. 1185–1193, 2015.

[24] H. Günther, *NMR spectroscopy: basic principles, concepts and applications in chemistry*. John Wiley & Sons, 2013.

[25] R. L. Hartman, H. R. Sahoo, B. C. Yen, and K. F. Jensen, "Distillation in microchemical systems using capillary forces and segmented flow", *Lab on a Chip*, vol. 9, no. 13, pp. 1843–1849, 2009.

[26] R. L. Hartman, J. R. Naber, S. L. Buchwald, and K. F. Jensen, "Multistep microchemical synthesis enabled by microfluidic distillation", *Angewandte Chemie International Edition*, vol. 49, no. 5, pp. 899–903, 2010.

[27] W. Harwell, W. Kaufmant, and L. Towert, "Re-entrant groove heat pipe", *AIAA Paper No. 77*, vol. 773, pp. 1–8, 1978.

[28] Hoffmann SE, https://www.hoffmann-group.com/pdf/DE/K49/pdf/dsh_de-de_46089.pdf, [Online; accessed on 16 September 2019].

[29] K. T. Hong, H. Imadojemu, and R. Webb, "Effects of oxidation and surface roughness on contact angle", *Experimental Thermal and Fluid Science*, vol. 8, no. 4, pp. 279–285, 1994.

[30] Y. Hu, T. Liu, X. Li, and S. Wang, "Heat transfer enhancement of micro oscillating heat pipes with self-rewetting fluid", *International Journal of Heat and Mass Transfer*, vol. 70, pp. 496–503, 2014.

[31] X. Huang, D. A. King, F. Zheng, V. S. Stenkamp, W. E. TeGrotenhuis, B. Q. Roberts, and D. L. King, "Hydrodesulfurization of jp-8 fuel and its microchannel distillate using steam reformate", *Catalysis Today*, vol. 136, no. 3-4, pp. 291–300, 2008.

[32] W.-J. Ju, L.-M. Fu, R.-J. Yang, and C.-L. Lee, "Distillation and detection of SO2 using a microfluidic chip", *Lab on a Chip*, vol. 12, no. 3, pp. 622–626, 2012.

[33] E. Y. Kenig, Y. Su, A. Lautenschleger, P. Chasanis, and M. Grünewald, "Micro-separation of fluid systems: A state-of-the-art review", *Separation and Purification Technology*, vol. 120, pp. 245–264, 2013.

[34] J. Kern and P. Stephan, "Investigation of decisive mixture effects in nucleate boiling of binary mixtures using a theoretical model", *Journal of Heat Transfer*, vol. 125, no. 6, pp. 1116–1122, 2003.

[35] J. Kern and P. Stephan, "Theoretical model for nucleate boiling heat and mass transfer of binary mixtures", *Journal of Heat Transfer*, vol. 125, no. 6, pp. 1106–1115, 2003.

[36] S. Kessler and L. Brüll, "Neue Produktionskonzepte für die Prozessindustrie erfordern modularisierte Logistiklösungen", *Chemie Ingenieur Technik*, vol. 9, no. 87, pp. 1240–1245, 2015.

[37] M. Kunkel and J. Schulze, "Noncontact measurement of central lens thickness", *Glass Science and Technology*, vol. 78, no. 5, pp. 245–247, 2005.

[38] M. Kuramae and M. Suzuki, "Two-component heat pipes utilizing the Marangoni effect", *Journal of Chemical Engineering of Japan*, vol. 26, pp. 230–231, 2 1993.

[39] K. Lam, E. Cao, E. Sorensen, and A. Gavriilidis, "Development of multistage distillation in a microfluidic chip", *Lab on a Chip*, vol. 11, no. 7, pp. 1311–1317, 2011.

[40] K. Lam, E. Sorensen, and A. Gavriilidis, "Towards an understanding of the effects of operating conditions on separation by microfluidic distillation", *Chemical Engineering Science*, vol. 66, no. 10, pp. 2098–2106, 2011.

[41] F. Lefèvre, R. Rullière, G. Pandraud, and M. Lallemand, "Prediction of the temperature field in flat plate heat pipes with micro-grooves – experimental validation", *International Journal of Heat and Mass Transfer*, vol. 51, no. 15, pp. 4083–4094, 2008.

[42] F. Lefèvre, R. Rullière, S. Lips, and J. Bonjour, "Confocal microscopy for capillary film measurements in a flat plate heat pipe", *Journal of Heat Transfer*, vol. 132, no. 3, pp. 031 502–1–031502–6, 2010.

[43] F. Lefèvre, S. Lips, and J. Bonjour, "Investigation of evaporation and condensation processes specific to grooved flat heat pipes", *Frontiers in Heat Pipes (FHP)*, vol. 1, no. 2, pp. 1–8, 2010.

[44] E. W. Lemmon, M. L. Huber, and M. O. McLinden, *NIST Standard Reference Database 23: Reference Fluid Thermodynamic and Transport Properties-REFPROP, Version 9.1, National Institute of Standards and Technology*, 2013.

[45] F. P. León, *Messtechnik*. Springer-Verlag, 2015.

[46] S. Lips, F. Lefèvre, and J. Bonjour, "Combined effects of the filling ratio and the vapour space thickness on the performance of a flat plate heat pipe", *International Journal of Heat and Mass Transfer*, vol. 53, no. 4, pp. 694–702, 2010.

[47] S. Lips, F. Lefèvre, and J. Bonjour, "Physical mechanisms involved in grooved flat heat pipes: Experimental and numerical analyses", *International Journal of Thermal Sciences*, vol. 50, no. 7, pp. 1243–1252, 2011.

[48] J. MacInnes, J. Ortiz-Osorio, P. Jordan, G. Priestman, and R. Allen, "Experimental demonstration of rotating spiral microchannel distillation", *Chemical Engineering Journal*, vol. 159, no. 1-3, pp. 159–169, 2010.

[49] F. Malz and H. Jancke, "Validation of quantitative NMR", *Journal of Pharmaceutical and Biomedical Analysis*, vol. 38, no. 5, pp. 813–823, 2005.

[50] W. L. McCabe and E. Thiele, "Graphical design of fractionating columns", *Industrial & Engineering Chemistry*, vol. 17, no. 6, pp. 605–611, 1925.

[51] A. Mersmann, M. Kind, and J. Stichlmair, *Thermische Verfahrenstechnik : Grundlagen und Methoden*. Springer-Verlag, 2005.

[52] M. Potash Jr. and P. Wayner Jr., "Evaporation from a two-dimensional extended meniscus", *International Journal of Heat and Mass Transfer*, vol. 15, no. 10, pp. 1851–1863, 1972.

[53] E. A. Ramirez-Gonzalez, C. Martinez, and J. Alvarez, "Modeling zero-gravity distillation", *Industrial & Engineering Chemistry Research*, vol. 31, no. 3, pp. 901–908, 1992.

[54] R. Revellin, R. Rullière, F. Lefèvre, and J. Bonjour, "Experimental validation of an analytical model for predicting the thermal and hydrodynamic capabilities of flat micro heat pipes", *Applied Thermal Engineering*, vol. 29, no. 5, pp. 1114–1122, 2009.

[55] R. Richter, P. Brennan, and J. Rankin, "Development of an advanced trapezoidal axially grooved (ATAG) heat pipe", in *4th Thermophysics and Heat Transfer Conference*, 1986, pp. 1–8.

[56] S. Rieks, N. Preußer, T. Gambaryan-Roisman, and E. Kenig, “Zero-gravity distillation with metal foams: A modelling approach”, *Chemical Engineering Transactions*, vol. 69, pp. 283–288, 2018.

[57] S. Rieks, M. Wende, N. Preußer, T. Gambaryan-Roisman, and E. Y. Kenig, “A hydrodynamic analogy based modelling approach for zero-gravity distillation with metal foams”, *Chemical Engineering Research and Design*, vol. 147, pp. 615–623, 2019.

[58] R. Rullière, F. Lefèvre, and M. Lallemand, “Prediction of the maximum heat transfer capability of two-phase heat spreaders – experimental validation”, *International Journal of Heat and Mass Transfer*, vol. 50, no. 7, pp. 1255–1262, 2007.

[59] R. Savino and D. Paterna, “Marangoni effect and heat pipe dry-out”, *Physics of Fluids*, vol. 18, no. 11, pp. 118 103–1–11810–4, 2006.

[60] R. Savino, D. De Cristofaro, and A. Cecere, “Flow visualization and analysis of self-rewetting fluids in a model heat pipe”, *International Journal of Heat and Mass Transfer*, vol. 115, pp. 581–591, 2017.

[61] R. Savino, N. di Francescantonio, R. Fortezza, and Y. Abe, “Heat pipes with binary mixtures and inverse marangoni effects for microgravity applications”, *Acta Astronautica*, vol. 61, no. 1, pp. 16–26, 2007.

[62] R. Savino, C. Piccolo, R. Fortezza, and Y. Abe, “Heat pipes with self-rewetting fluids under low-gravity conditions”, *Microgravity Science and Technology*, vol. 19, no. 3-4, pp. 75–77, 2007.

[63] R. Savino, A. Cecere, and R. Di Paola, “Surface tension-driven flow in wickless heat pipes with self-rewetting fluids”, *International Journal of Heat and Fluid Flow*, vol. 30, no. 2, pp. 380–388, 2009.

[64] R. Savino, R. Di Paola, A. Cecere, and R. Fortezza, “Self-rewetting heat transfer fluids and nanobrines for space heat pipes”, *Acta Astronautica*, vol. 67, no. 9-10, pp. 1030–1037, 2010.

[65] R. Schlitt, “Development of an axially grooved heat pipe with non-constant groove width”, in *3rd International Heat Pipe Conference*, 1978, pp. 1–9.

[66] R. Schlitt, “Performance characteristics of recently developed high-performance heat pipes”, *Heat Transfer Engineering*, vol. 16, no. 1, pp. 44–52, 1995.

[67] T. Schulze, C. Sodtke, P. Stephan, T. Gambaryan-Roisman, and C. Brandt, “Performance of heatpipe evaporators for space applications with combined re-entrant and micro grooves”, in *Proceedings of the 14th International Heat Pipe Conference, 2007*, 2007, pp. 127–132.

[68] D. R. Seok and S.-T. Hwang, “Zero-gravity distillation utilizing the heat pipe principle (micro-distillation)”, *AIChE Journal*, vol. 31, no. 12, pp. 2059–2065, 1985.

[69] R. K. Shah and D. P. Sekulic, *Fundamentals of heat exchanger design*. John Wiley & Sons, 2003.

[70] S. Shchukarev and T. Tolmacheva, “Solubility of oxygen in ethanol-water mixtures”, *Journal of Structural Chemistry*, vol. 9, no. 1, pp. 16–21, 1968.

[71] P. Stephan and C. Busse, “Analysis of the heat transfer coefficient of grooved heat pipe evaporator walls”, *International Journal of Heat and Mass Transfer*, vol. 35, no. 2, pp. 383–391, 1992.

[72] P. Stephan and C. Brandt, “Advanced capillary structures for high performance heat pipes”, *Heat Transfer Engineering*, vol. 25, no. 3, pp. 78–85, 2004.

[73] P. Stephan, K. Schaber, K. Stephan, and F. Mayinger, *Thermodynamik: Grundlagen und technische Anwendungen – Band 2: Mehrstoffsysteme und chemische Reaktionen*. Springer-Verlag, 2017.

[74] A. Sundberg, P. Uusi-Kyyny, and V. Alopaeus, “Novel micro-distillation column for process development”, *Chemical Engineering Research and Design*, vol. 87, no. 5, pp. 705–710, 2009.

[75] A. Sundberg, P. Uusi-Kyyny, K. Jakobsson, and V. Alopaeus, “Development and modeling of micro distillation column”, in *Distillation & Absorption, Eindhoven, The Netherlands, 12-15 September 2010*, 2010, pp. 217–222.

[76] A. T. Sundberg, P. Uusi-Kyyny, K. Jakobsson, and V. Alopaeus, “Control of reflux and reboil flow rates for milli and micro distillation”, *Chemical Engineering Research and Design*, vol. 91, no. 5, pp. 753–760, 2013.

[77] A. Sundberg, P. Uusi-Kyyny, and V. Alopaeus, “Microscale distillation”, *Russian Journal of General Chemistry*, vol. 82, no. 12, pp. 2079–2087, 2012.

[78] C. Tien and A. Rohani, “Theory of two-component heat pipes”, *Journal of Heat Transfer*, vol. 94, no. 4, pp. 479–484, 1972.

[79] J. Tokunaga, “Solubilities of oxygen, nitrogen, and carbon dioxide in aqueous alcohol solutions”, *Journal of Chemical and Engineering Data*, vol. 20, no. 1, pp. 41–46, 1975.

[80] J. Tschernjaew, E. Kenig, and A. Górak, “Mikrodestillation von Mehrkomponentensystemen”, *Chemie Ingenieur Technik*, vol. 68, no. 3, pp. 272–276, 1996.

[81] T. Vencel, J. Donovalova, A. Gaplovsky, T. Kimura, and S. Toma, “Oxygen exclusion from the organic solvents using ultrasound and comparison with other common techniques used in photochemical experiments”, *Chemical Papers-Slovak Academy of Sciences*, vol. 59, no. 4, pp. 271–274, 2005.

[82] Verein Deutscher Ingenieure, Ed., *VDI Wärmeatlas*. Springer Verlag, 2013.

[83] WIKA Alexander Wiegand SE & Co. KG, `https://en.wika.com/p_30_p_31_en_co.WIKA`, [Online; accessed on 12 September 2019].

[84] R. C. Wootton and A. J. deMello, “Continuous laminar evaporation: Micron-scale distillation”, *Chemical Communications*, no. 3, pp. 266–267, 2004.

[85] M. Wutz, H. Adam, and W. Walcher, *Handbuch Vakuumtechnik: Theorie und Praxis*. Springer-Verlag, 2013.

[86] X. Xu and V. Carey, "Film evaporation from a micro-grooved surface – an approximate heat transfer model and its comparison with experimental data", *Journal of Thermophysics and Heat Transfer*, vol. 4, no. 4, pp. 512–520, 1990.

[87] Y. Zhang, S. Kato, and T. Anazawa, "Vacuum membrane distillation on a microfluidic chip", *Chemical Communications*, no. 19, pp. 2750–2752, 2009.

[88] Y. Zhang, S. Kato, and T. Anazawa, "Vacuum membrane distillation by microchip with temperature gradient", *Lab on a Chip*, vol. 10, no. 7, pp. 899–908, 2010.

[89] F. Zheng, V. S. Stenkamp, W. E. TeGrotenhuis, X. Huang, and D. L. King, "Microchannel distillation of jp-8 jet fuel for sulfur content reduction", in *2006 AIChE annual meeting, San Francisco*, 2006.

[90] A. Ziogas, V. Cominos, G. Kolb, H.-J. Kost, B. Werner, and V. Hessel, "Development of a microrectification apparatus for analytical and preparative applications", *Chemical Engineering & Technology*, vol. 35, no. 1, pp. 58–71, 2012.

List of Figures

List of Tables

Appendix A

Experimental Equipment

Table A.1: Pressure and temperature measurement systems

Device	Description	Manufacturer
thermocouples	type K	Temperatur Messelemente Hettstedt
Platinum resistance thermometers	Pt100/A	Temperatur Messelemente Hettstedt
pressure sensor	p-30	WIKA Alexander Wiegand
measurement controller	cRIO 9022 with NI 9201 and NI 9213 modules	National Instruments

Table A.2: Optical measurement system

Device	Description	Manufacturer
chromatic confocal measurement system	CHRocodile E with 3 mm optical probe	Precitec
electrical positioning unit	X-LSM 100 A	Zaber Technologies

Table A.3: Heating and cooling systems

Device	Description	Manufacturer
power supply unit	EA-PS 8160-60	EA Elektro-Automatik
heating foils	BK-3521-5.4-L12-03	Birk Manufacturing
bath thermostats	Ministat 125 cc3	Peter Huber Kältemaschinenbau

Appendix B

Theoretical Model

B.1 Equality of Mean Liquid and Vapor Mole Fractions

As stated in Section 6.2, the axial mass flows in the liquid and vapor phase are the same. Since no reactions occur in the system, the same holds true for the total axial molar flows, which are the sum of the component flows

$$\dot{N}_{z,\mathrm{A,L}} + \dot{N}_{z,\mathrm{B,L}} = \dot{N}_{z,\mathrm{A,V}} + \dot{N}_{z,\mathrm{B,V}}. \tag{B.1}$$

For the same reason, the axial molar flows of both components in the liquid and vapor phase are equal according to

$$\dot{N}_{z,\mathrm{A,L}} = \dot{N}_{z,\mathrm{A,V}} \tag{B.2}$$

and

$$\dot{N}_{z,\mathrm{B,L}} = \dot{N}_{z,\mathrm{B,V}}. \tag{B.3}$$

Due to the negligence of axial diffusion the component flows are described through Equation 6.26. Plugging Equation 6.26 in Equation B.1 and Equation B.2 leads to

$$\overline{w}_{\mathrm{L}}\,\overline{c}_{\mathrm{A,L}} A_{\mathrm{L}} + \overline{w}_{\mathrm{L}}\,\overline{c}_{\mathrm{B,L}} A_{\mathrm{L}} = \overline{w}_{\mathrm{V}}\,\overline{c}_{\mathrm{A,V}} A_{\mathrm{V}} + \overline{w}_{\mathrm{V}}\,\overline{c}_{\mathrm{B,V}} A_{\mathrm{V}} \tag{B.4}$$

and

$$\overline{w}_{\mathrm{L}}\,\overline{c}_{\mathrm{A,L}} A_{\mathrm{L}} = \overline{w}_{\mathrm{V}}\,\overline{c}_{\mathrm{A,V}} A_{\mathrm{V}}. \tag{B.5}$$

Dividing Equation B.5 by Equation B.4 leads to

$$\frac{\overline{c}_{\mathrm{A,L}}}{\overline{c}_{\mathrm{A,L}} + \overline{c}_{\mathrm{B,L}}} = \frac{\overline{c}_{\mathrm{A,V}}}{\overline{c}_{\mathrm{A,V}} + \overline{c}_{\mathrm{B,V}}}, \tag{B.6}$$

which shows the equality of $\overline{\widetilde{x}}_A$ and $\overline{\widetilde{y}}_A$ and thereby the equality of $\overline{\widetilde{x}}_B$ and $\overline{\widetilde{y}}_B$.

B.2 Description of Overall Concentration

The mean concentration is calculated with the density and the molar mass of the mixture according to

$$\overline{c} = \frac{\rho}{\widetilde{M}}. \tag{B.7}$$

The molar mass of the mixture is the sum of the mole fractions multiplied with the molar masses of the components. Thus, considering Equation 6.47 $\overline{c}$ is

$$\overline{c} = \frac{1}{\frac{\overline{c}_A}{\overline{c}}\widetilde{M}_A + \frac{\overline{c}-\overline{c}_A}{\overline{c}}\widetilde{M}_B} \frac{1}{\frac{\overline{c}_A}{\overline{c}}\frac{1}{\rho_A} + \frac{\overline{c}-\overline{c}_A}{\overline{c}}\frac{1}{\rho_B}}. \tag{B.8}$$

This equation can be rearranged for $\overline{c}$. Thus, $\overline{c}$ is only dependent on $\overline{c}_A$ and fluid properties. With Equation 6.37 $\overline{c}_B$ can be calculated from $\overline{c}$ and $\overline{c}_A$.

B.3 Mesh Independence of Dimensionless Parameters

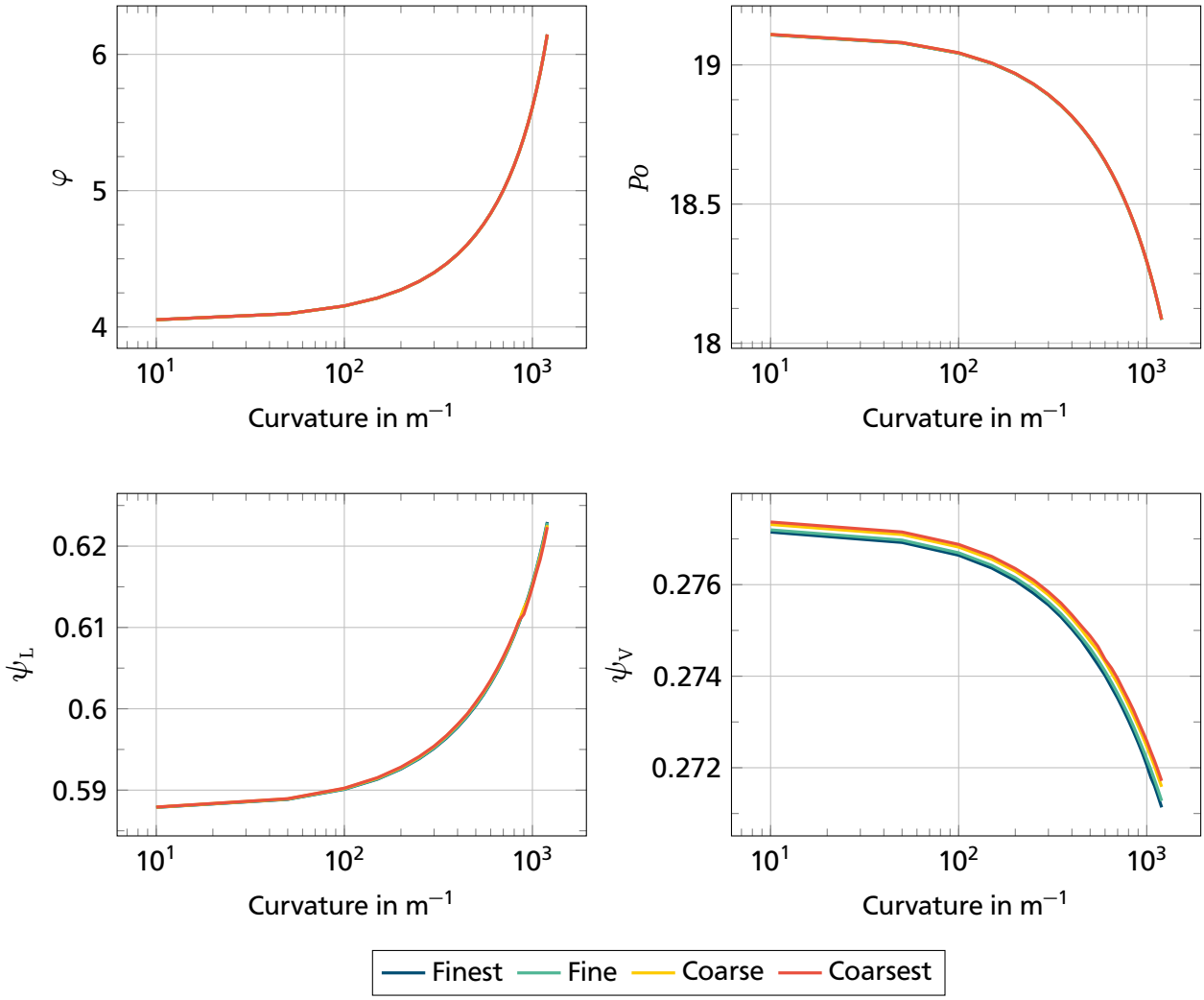

Figure B.1: Dimensionless parameters over curvature of the liquid-vapor interface for a half re-entrant channel (h_{RE} = 1.4 mm, R_{RE} = 800 µm, W_G = 0.9 mm) and the corresponding vapor phase (h_V = 10 mm, W = 2 mm) for triangular meshes with different refinements. The highest deviations between the different meshes can be observed for the diffusive transport coefficient of the vapor phase ψ_V. These are below 1 % between the coarsest and the finest mesh. The finest mesh was chosen for all the simulations.

Table B.1: Parameters of investigated meshes

Discretization	Maximum element size in m	Minimum element size in m	Maximum element growth rate	Curvature factor
finest	$6.7 \cdot 10^{-6}$	$2.0 \cdot 10^{-8}$	1.05	0.2
fine	$1.3 \cdot 10^{-5}$	$1.5 \cdot 10^{-7}$	1.08	0.25
coarse	$2.8 \cdot 10^{-5}$	$4.0 \cdot 10^{-7}$	1.1	0.25
coarsest	$3.5 \cdot 10^{-5}$	$1.0 \cdot 10^{-6}$	1.13	0.3